Excitation and relaxation of the electronic subsystem in solids after high energy deposition

Dissertation

Nikita A. Medvedev

Abstract

The present dissertation contains the theoretical studies performed on the topic of a high energy deposition in matter. The work focuses on electronic excitation and relaxation processes on ultrafast timescales. Energy deposition by means of intense ultrashort (femtosecond) laser pulses or by means of swift heavy ions irradiation have a certain similarities: the final observable material modifications result from a number of processes on different timescales. First, the electronic excitation by photoabsorption or by ion impact takes place on subfemtosecond timescales. Then these excited electrons propagate and redistribute their energy interacting among themselves and exciting secondary generations of electrons. This typically takes place on femtosecond timescales. On the order of tens to hundreds femtoseconds the excited electrons are usually thermalized. The energy exchange with the lattice atoms lasts up to tens of picoseconds. The lattice temperature can reach melting point; then the material cools down and recrystalizes, forming the final modified nanostructures, which are observed experimentally. The processes on each previous step form the initial conditions for the following step. Thus, to describe the final phase transition and formation of nanostructures, one has to start from the very beginning and follow through all the steps.

The present work focuses on the early stages of the energy dissipation after its deposition, taking place in the electronic subsystems of excited materials. Different models applicable for different excitation mechanisms will be presented: in the thesis I will start from the description of high energy excitation (electron energies of $\sim$ keV), then I shall focus on excitations to intermediate energies of electrons (~ 100 eV), and finally coming down to a few eV electron excitations (visible light). The results will be compared with experimental observations.

For the high energy material excitation assumed to be caused by irradiation with swift heavy ions, the classical Asymptotical Trajectory Monte-Carlo (ATMC) is applied to describe the excitation of electrons by the impact of the projectile, the initial kinetics of electrons, secondary electron creation and Auger-redistribution of holes. I first simulate the early stage (first tens of fs) of kinetics of the electronic subsystem (in silica target, SiO_2) in tracks of ions decelerated in the electronic stopping regime. It will be shown that the well pronounced front of excitation in the electronic and ionic subsystems is formed due to the propagation of electrons, which cannot be described by models based

on diffusion mechanisms (e.g. parabolic equations of heat diffusion). On later timescales, the thermalization time of electrons can be estimated as a time when the particle- and the energy propagation turns from the ballistic to the diffusive one. As soon as the electrons are thermalized, one can apply the Two Temperature Model. It will be demonstrated how to combine the MC output with the two temperature model. The results of this combination demonstrate that secondary ionizations play a very important role for the track formation process, leading to energy stored in the hole subsystem. This energy storage causes a significant delay of heating and prolongs the timescales of lattice modifications up to tens of picoseconds.

For intermediate energies of excitation (XUV-VUV laser pulse excitation of materials) I applied the Monte-Carlo simulation, modified where necessary and extended in order to take into account the electronic band structure and Pauli's principle for electrons within the conduction band. I apply the new method for semiconductors and for metals on examples of solid silicon and aluminum, respectively.

It will be demonstrated that for the case of semiconductors the final kinetic energy of free electrons is much less than the total energy provided by the laser pulse, due to the energy spent to overcome ionization potentials. It was found that the final total number of electrons excited by a single photon is significantly less than $\hbar\omega/E_{gap}$. The concept of an 'effective energy gap' is introduced for collective electronic excitation, which can be applied to estimate the free electron density after high-intensity VUV laser pulse irradiation.

For metals, experimentally observed spectra of emitted photons from irradiated aluminum can be explained well with our results. At the characteristic time of a photon emission due to radiative decay of $L-$shell hole ($t < 60$ fs), the distribution function of the electrons is not yet fully thermalized. This distribution consists of two main branches: low energy distribution as a distorted Fermi-distribution, and a long high energy tail. Therefore, the experimentally observed spectra demonstrate two different branches of results: the one observed with $L-$shell radiation emission reflects the low energy distribution, the Bremsstrahlung spectra reflects high energy (nonthermalized) tail. The comparison with experiments demonstrated a good agreement of the calculated spectra with the experimentally observed ones.

For the irradiation of semiconductor with low energy photons (visible light), a statistical model named the "extended multiple rate equation" is proposed. Based on the earlier developed multiple rate equation, the model additionally includes the interaction of electrons with the phononic subsystem of the lattice and allows for the direct determination of the conditions for crystal damage. Our model effectively describes the dynamics of the electronic subsystem, dynamical changes in the optical properties, and lattice heating, and the results are in very good agreement with experimental measurements on the transient reflectivity and the fluence damage threshold of silicon irradiated with a femtosecond laser pulse.

Zusammenfassung

Diese Dissertation beschreubt theoretische Untersuchungen zur Hochenergiedeposition in Materie. Die Schwerpunkte liegen auf den elektronischen Anregungen sowie den Relaxationsprozessen auf ultrakurzen Zeitskalen. Energiedeposition durch ultrakurze (Femtosekunden) Laserpulse hoher Intensität oder durch schnelle schwere Ionen haben einige Gemeinsamkeiten: Die beobachtbaren Materialveranderungen sind das Resultat diverser Prozesse auf verschiedenen Zeitskalen.

Zuerst regen Photoabsorption bzw. Ioneneinschlag, auf einer subfemtosekunden Zeitskala das elektronische System an. Diese angeregten Elektronen propagieren, verteilen ihre Energie untereinander, und erzeugen Sekundärelektronen; dies geschieht typischerweise innerhalb von Femtosekunden. Innerhalb von zehn bis hundert Femtosekunden sind die angeregten Elektronen in der Regel thermalisiert. Der Energieaustausch mit den Gitteratomen dauert bis zu zehn Pikosekunden. Die Gittertemperatur kann den Schmelzpunkt erreichen, danach kühlt sich das Material ab und rekristallisiert, wobei es experimentell beobachtbare Nanostrukturen formen kann.

Die Ergebnisse eines jeden Schrittes stellen die Startbedingungen für den folgendem Schritt dar. Will man den finalen Phasenubergang und die Bildung von Nanostrukturen beschreiben, muss man daher alle Schritte von Beginn an durchlaufen.

Diese Arbeit konzentriert sich auf die frühen Stadien der Energiedissipation nach der Deposition in den elektronischen Subsystemen des angeregten Materials. Verschiedene Modelle, anwendbar für unterschiedliche Anregungen, werden vorgestellt: Ich beginne mit hochenergetischer Anregung (Elektronen mit mehrer keV Energie), beschäftige mich mit dem mittleren Energiebereich (100 eV) und letztendlich der Elektronenanregung mit wenigen eV (sichtbares Licht). Die Ergebnisse werden mit experimentellen Beobachtungen verglichen.

Für die hochenergetische Materialanregung durch Bestrahlung mit schnellen schweren Ionen wird die klassische "Asymptotical Trajectory Monte-Carlo (ATMC) Methode" verwendet. Mit ihr wird die Anregung von Elektronen durch den Einschlag von Projektilen, die anfängliche Dynamik der Elektronen, die Erzeugung von Sekundärelektronen und die Auger Redistribution der Löcher beschrieben.

Es wird gezeigt, dass sich durch die Elektronenpropagation eine deutlich hervortretende Anregungsfront im elektronischen und ionischen Subsystem bildet. Dabei kann die Elektronenpropagation nicht mit Modellen beschrieben werden, die auf Diffusionsmechanismen basieren (z.B. Parabolische Wärmediffusionsgleichung).

Für größere Zeitskalen berechne ich die Thermalisierungszeit der Elektronen. Diese gelten als thermalisiert, wenn die Elektronen- und Energiepropagation von ballistisch zu diffus überwechselt. Nachdem die Elektronen thermalisiert sind, kann man das Zwei Temperatur Modell verwenden. Die Weiterverarbeitung der MC Ergebnisse im Zwei Temperatur Modell wird dargestellt und erläutert. Die Ergebnisse dieser Kombination zeigen, dass die Ionisierung von Sekundärelektronen eine sehr wichtige Rolle für den Spurbildungsprozess spielt. Sie führen zu einem zusatzlichen Term in der Wärmediffusionsgleichung, der sich auf die im Subsystem der Löcher gespeicherte Energie bezieht. Die Ernegiespeicherung verursacht eine signifikante Verzögerung der Aufheizung und verlängert die Zeitskalen um mehrere Dutzend Pikosekunden.

Für die mittleren Anregungsenergien (XUV-VUV Laserpulsanregung von Materialien) verwende ich Monte-Carlo Simulationen, die an notwendigen Stellen modifiziert und erweitert wurden, um die elektronische Bandstruktur sowie das Pauli Prinzip für die Elektronen im Leitungsband einzubeziehen.

Ich verwende diese neue Methode für Halbleiter und Metalle am Beispiel von Quarz, bzw. Aluminium. Es wird wird gezeigt, dass für Halbleiter die endgültige kinetische Energie der freien Elektronen weit unter der vom Laser bereitgestellten Energie liegt. Dies liegt daran, dass Energie aufgewendet werden muss, um das Ionisierungspotenzial zu überwinden.

Es stellte sich heraus, dass die endgültige Elektronenzahl, die durch durch ein einzelnes Photon angeregt wird deutlich unter $\hbar\omega/E_{gap}$ liegt. Das Konzept der Ďeffektiven BandlückeŞ wird fur kollektive elektronische Anregungen eingeführt. Es kann verwendet werden um die Dichte freier Elektronen nach der Bestrahlung mit hochintensiven VUV Laserpulsen abzuschätzen.

Experimentell beobachtete Photoemissionsspektren von bestrahltem Aluminium können durch unsere Ergebnisse gut erklärt werden. Zur charakteristischen Zeit der Photoemission durch strahlenden Zerfall eines L-Schalen Lochs (t < 60 fs), ist die Verteilungsfunktion der Elektronen noch nicht vollständig thermalisiert. Die Verteilungsfunktion besteht aus zwei Hauptbereichen: Eine Verteilung niedriger Energie in Form einer deformierten Fermiverteilung und einem langen Hochenergieausläufer. Darum zeigen die beobachteten Spektren zwei Bereiche: der eine, beobachtet mit L-Schalen Emission, spiegelt die Verteilung niedriger Energie wider, das Bremsstrahlungsspektrum reflektiert den (nicht thermalisierten) Hochenergieauslaufer. Der Vergleich zeigt eine gute Übereinstimmung zwischen den berechneten und den experimentell beobachteten Spektren.

Zur Modellierung der Bestrahlung von Halbleitern mit Photonen niedriger Energie (sichtbares Licht), wird ein statistisches Modell vorgeschlagen, die Erweiterte Multiple Ratengleichung. Basierend auf der früher entwickelten Multiplen Ratengleichung, beinhaltet dieses Modell zusätzlich die Wechselwirkung von Elektronen mit dem phononischen Subsystem des Gitters. Es erlaubt, die Bedingungen für eine Schädigung des Kristalls direkt zu bestimmen. Unser Modell beschreibt effektiv die Dynamik des elektronischen Subsystems und der Kristallerwärmung. Die Resultate sind in sehr guter Übereinstimmung mit experimentellen Messungen der zeitabhängigen Reflektivität und dem Schadensschwellenwert der Fluenz von mit Femtosekunden Laserpulsen bestrahltem Silizium.

Contents

Chapter 1

Introduction

High energy deposition into materials by means of laser or swift heavy ion beams is a subject of significant interest from both, experimental and theoretical points of view. Recent development of experimental techniques has led to an essential progress in understanding of fundamental processes, which occurs in irradiated solids (dielectrics, semiconductors and metals), in plasma, and in warm dense matter - a transient state between solid and plasma states of matter.

Experiments with lasers in the visible range have shown that the ultrashort laser irradiation produces observable modifications of the material surface, such as the formation of nanobumps and the creation of molten regions [1–4]. With the invention of femtosecond lasers, which have a pulse duration comparable to characteristic times for processes in the electronic subsystem of the material, nanometric spatial and femtosecond temporal scales have created new possibilities for nanotechnologies, micromachining and medical surgery. A high potential for applications of intense femtosecond laser pulses (FLP) in applications have stimulated fundamental theoretical and experimental investigations of strongly non-equilibrium states of matter [5–15]. The first experiments with the free-electron laser in Hamburg (FLASH), a laser that provides pulses of femtosecond duration in the vacuum ultraviolet (VUV) to extreme ultraviolet (XUV) energy regime, opened a pathway to promising new areas of fundamental research and technical applications [16–20].

In this new range of photon energies that was not previously accessible by experiments, there remains a lack of data about the primary response of the material to irradiation. Therefore, theoretical investigations are necessary to predict and interpret experimental observations. Such theoretical investigations must consider the range from the very first energy absorption event to the final phase transitions and structural modifications of the target.

Ultrashort laser pulses allow access to fundamental electronic processes in the solid because the pulse duration is comparable to the characteristic femtosecond timescale for collisional processes such as electron-electron interactions and electron-lattice collisions. The kinetics of the excitation and

relaxation of the target can be divided into a set of processes separated temporally. Due to the mass difference between electrons and ions, excitation of the electronic subsystem by a laser pulse and the subsequent creation of second-generation free electrons occurs much faster (some femtoseconds, $\sim 10^{-15}$ s, or the duration of a pulse) [14, 21] than other processes such as energy exchange with the lattice and the cooling of excited electrons, which both take up to $\sim 10^{-11}$ s [22–27]. The processes in the electronic subsystem play a fundamental role because they provide the initial conditions for subsequent energy dissipation. Thus, these processes are of essential interest for all material behaviour - from the initial light absorption to further energy dissipation and the eventual phase transitions of the target in the form of melting or a transformation to warm dense matter [5, 10, 14, 23, 24].

For the case of swift heavy ions (SHI), these peculiarities of ultrashort temporal and nanosize spacial scales are even more pronounced and more important. SHI with energies higher than ~ 1 MeV/amu and masses higher than ~ 20 proton masses stimulate structural and phase transformations in vicinities of a few nanometers of their trajectories when penetrating various solids. These effects occur in the electronic stopping regime, when the electronic energy loss of a projectile overcomes a threshold ($\sim 2 - 5$ keV/nm in dielectrics). The radiation damage produced by elastic recoils is orders of magnitude too low to provide the observed structural modifications in tracks [28–35].

Spatial anisotropy, nanometric spatial and subpicosecond temporal scales, as well as extremely high excitation of materials in SHI tracks supply with new tools for nanotechnologies [31, 36] and give new abilities for investigations of strongly non-equilibrium states of matter [37–47]. Strong deviations from the equilibrium in excited SHI tracks can result in pathways of the relaxation kinetics which may be hardly described by ordinary macroscopic models based on local equilibrium conceptions [38, 45, 46]. Furthermore, analytical descriptions of the track kinetics usually neglect effects of holes created in different atomic shells during ionization of a media by a projectile. In addition to a high energy accumulated in these holes, their decay leads to creation of secondary generations of electrons and holes that affects considerably the kinetics of the electronic subsystem in the track.

In both cases, FLP and SHI irradiation of matter, the material transformations can be characterized by the fact, that initially the electronic subsystem is excited to high energies, and only then the lattice is heated by the electrons. One can expect certain similarities in both cases: the excited electronic subsystem should behave similarly on ultrashort timescales. This electronic behaviour and energy exchange with a lattice define the following material transformations.

The dissertation is arranged in three main parts, preceded by the general description of the statistical methods used. These three parts are ordered according to the level of excitation of a solid after the energy deposition: high energy ($\sim$ keV) electron excitation regime, intermediate electron excitations

($\sim$ 100 eV), and low energy electron dynamics (a few eV energies). Each of these energy regimes has its own peculiarities that have to be included in an adequate model.

The first part (chapters 3 and 4) is focused on the SHI irradiation of insulators. There we are interested in the high energies of electronic excitations (up to several tens of keV). At so high energies, the semiclassical descriptions are working well, therefore, we will give an overall description of the methods used in there and following chapters (chapters 3 to 6). We will present a Monte-Carlo (MC) approach for SHI irradiation, and compare the results with experiments. All cross-sections applied in the work are described in these chapters and discussed in more detail in the Appendix. This part is accomplished by presenting the combination of the MC approach with the two temperature model (TTM) and discussion of the advantages of this combined MC-TTM approach.

In the second part (chapters 5 and 6) we focus on the description of an excitation of the electronic subsystem of materials in ultrashort timescales by intermediate energies (in the order of $\sim$ 100 eV). We consider the excitation with FLP in VUV-XUV photon energy range, as they are produced in the new experimental facility FLASH - free electron laser in Hamburg, Germany. For this purpose, we have developed an advanced MC code, which describes the excitation and relaxation processes in terms of single particles. Here we give a brief description of a standard MC modeling and extend the MC approach to account for density of states (DOS) of a particular material and for such quantum effects as Pauli blocking. We describe important peculiarities of the description of the electronic subsystem in the energy range of tens of electronvolts. In the analysis of the results for semiconductors, we introduce a concept of an effective energy gap (EEG), which allows for simple estimation of the number of excited electrons per absorbed photon. Later we give a description of metals, where we show its difference as compared to the case of semiconductors. For both kinds of materials, we analyze an influence of the material and the laser pulse properties on the resulting electron behavior. Also, comparisons with experimental results are presented there.

The third and last part (chapter 7) is maintaining an extended multiple rate equation (EMRE), a model proposed to describe irradiation of semiconductors or dielectrics with visible light, which means that electrons are excited to energies of a few eV only. The EMRE, being a numerical realization of the kinetic equation, combines the simplicity of rate equation systems with a tracing of the nonequilibrium electronic distribution. The difference from the usual thermodynamical models (as Two Temperature Model) are discussed, and the comparison with experiments is presented.

The partial summaries and conclusions are given within the chapters, and the general overview of the thesis is presented in chapter 8. Finally, the Appendix discusses cross-sections chosen for the MC modeling, presents some alternatives for the cross-sections and important features of the algorithms.

Chapter 2

General aspects of statistical methods

Statistical methods of calculations are one of the most important methods used to describe the many-body systems when some element of randomness is present – if a behavior of the system cannot be predetermined (due to a complexity of a system under investigation). From this point of view, we can divide all events into two general classes: events with a stable result, and events with a random result [48].

The first one, the stable results, means that the results will be definitely reproduced if the experiment/observation is repeated under the same conditions. For example, water is always boiling at 100° C temperature, if the atmospheric pressure is 760 mmHg.

In contrast, an element of randomness creates an unpredictability of any particular experiment; experiments repeated under the same condition can give different results. This, for instance, is realized in throwing a dice, or in a lottery. This element of randomness significantly changes the scientific interest in such processes: one cannot determine the result of any particular throw of a dice, but can find the full set of possible results and the frequency of repetition of any result in a row of experiments, thus, the *probability* of the result.

The element of randomness is present in problems of a particle transport through a matter: a free path of a particle between sequential collisions, a transferred energy in the collisions, a number of particles reflected or emitted at the surface, they are not predefined. Thus, experimentally, the number of emitted particles detected during the measurement is varying from one experiment to another. However, the *distribution* of particles is experimentally reproducible. The distribution describes a probability to find a particle of a certain kind (i.e. a particle with an energy within a given interval, a claster of particles of a given size etc.). Theoretical consideration of such processes also focuses on the probabilities, or distributions, of the results.

In this chapter we will discuss the methods that will be used further on in this work. At first, we will show the hierarchy of the statistical methods by means of how detailed information about the system can be extracted using the particular method. We will pay a special attention to the Monte-Carlo method,

which will be used in following chapters 3-6. The method used in chapter 7 is a numerical realization of a simplified kinetic equation. At the end of the present chapter, we will give a few general definitions of distributions frequently used in this work, namely, a) the Poisson distribution used to describe scattering of particles on randomly placed scattering centers; b) the Gaussian distribution, which is used to reproduce the laser pulse intensity as a set of photons. We will discuss the connections of this distributions to random numbers, which will be used in the Monte-Carlo method of simulation of particle transport.

2.1 Hierarchy of statistical methods

The commonly used methods can be classified as follows:

1. The method of individual collisions. This method uses detailed descriptions of every single event occurring with every single particle in the system. Realization of an event depends on processes involved; at each particular simulation it is defined by the generated random numbers. As a result of such simulations, one obtains the full information about every particle involved. Then, repeating the simulation to get statistically trustful results, one can extract the final distributions of the particles in space of coordinates-momenta-time. The methods are known as the Monte-Carlo (MC) methods [49].

2. The method of condensed (or extended) collisions. This method traces every single particle individually, but now the trajectory of the particle is constructed as a polygonal path, at each part of it between sequential kinks a number of collisions take a place. This is possible, taking into account that most of the scattering events for charged particles occur at large impact parameters and, thus, do not change significantly the trajectory and the energy of the particle. This method is less precise than the previous one, however, it can significantly save the computational power. At the end, again, the statistically averaged distributions can be obtained. This class of methods are also considered as the Monte-Carlo methods [49].

3. The kinetic equations. This class of methods is based on the Liouville equation. The particles are already distributed in space and momenta, and individual particles do not enter the calculations. Instead, the methods operate with the distribution functions, tracing a change of distributions in every space point. Different simplifications of the Liouville equation lead to the Bogoliubov-Born-Green-Kirkwood-Yvon (BBGKY) hierarchy [50], Boltzmann kinetic equation [51], Fokker-Planck equation [52].

4. The thermodynamic equations. This class of the equation is dealing with physical values already averaged with the distribution functions. Nor

particles, neither their distributions enter the equations. These methods
allow to trace changes in the experimentally observable values (temper-
ature, pressure, volume) without looking at the detailed description of
processes occurring with individual particles [53]. Here comes the con-
nection between actual statistical methods and the methods with stable
results.

Of course, the precision of the results obtained with each different method
and its limits of validity depend on the particular realized model.

In the present work, chapters 3-6 use the Monte-Carlo method according
to the method of individual collisions. Chapter 7 proposes a numerical model,
which relies on the Boltzmann equation, and, thus, can be classified as belong-
ing to the kinetic methods.

2.2   On the Monte-Carlo methods

The name "Monte-Carlo" was proposed by N. Metropolis and S.M. Ulam [54].
Since 40th of XX century, the method found a great amount of applications
in different fields of physics, astronomy, numerical mathematics, economics,
biology, social science, business.

It should be noted, that there is no single Monte Carlo method. Instead, the
term describes a large and widely-used class of approaches, which use random
inputs during the simulations. The most general idea of the algorithm can be
formulated as follows:

1. Define a domain of all possible inputs.

2. Choose inputs randomly from this domain, using a certain specified prob-
   ability distribution.

3. Perform a deterministic computation using this selected inputs.

4. Average the results of the individual computations to obtain the final
   result.

The Monte-Carlo methods are so widely and interdisciplinary used because
of their advantages, namely, a) the simplicity from the mathematical point of
view: the method doesn't require writing of complicated equations, instead it
requires only knowing the elementary processes going on in the system [55]; b)
the computational stability: since the method consists only of a huge amount
of repetition of similar iterations and averaging the obtained results, there is
no problem of stability, which is typical for the solution of differential equa-
tions; c) an easy applicability to different initial and boundary conditions [49].
Algorithms in the framework of the Monte-Carlo methods are usually quite
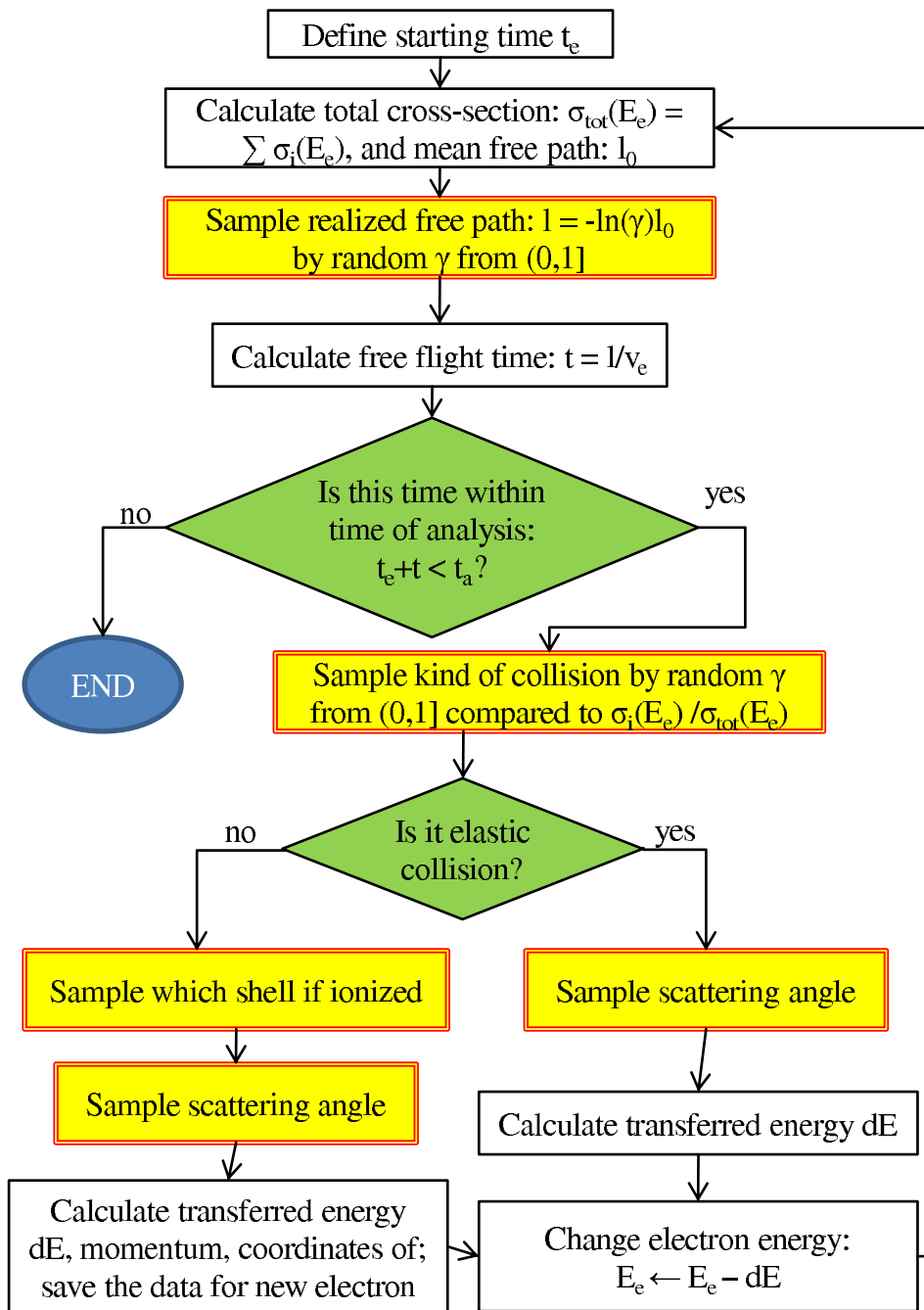transparent.

Figure 2.1: Schematic picture of a typical MC algorithm modeling electron transport. Solid white boxes denote calculations to be performed; double-lined yellow boxes show a stochastic sampling of a random parameter; choice to be made is in the diamond-shaped green box with two possible choices shown in arrows "yes" and "no" in the algorithm tree. The calculations stop when the choice reaches the END-box.

Fig.2.1 shows an example of the algorithm modeling electron transport trough a solid. It starts from initial conditions (defining the starting time of the electron being traced, its energy E_e, momentum and coordinates). Then, one has to calculate the total cross-section of scattering of this electron $\sigma_{tot}(E_e) = \sum \sigma_i(E_e)$. Note, that this box of the scheme itself may contain a number of internal blocks: one has to define all the possible processes and the corresponding cross-sections σ_i (comparing the electron energy to all ionization potential of the target atoms, and choosing only possible processes). After that, one meets the first stochastic choice to be made, after one has defined the realized free flight distance $l = -\ln(\gamma)l_0$ based on the calculated mean free path l_0. The details about the procedure are given in the next section and in the following chapters for each particular realization of the algorithm; here I give only a schematic picture.

Defining then the free flight time $t = l/v_e$ (where v_e is the electron velocity), one has to find whether this time is still within our time of analysis t_a, or the next collision occurs too late and, thus, must not be included in the modeling. In case if the time is within the time of interest, we shall follow the electron further. At the next step, the kind of the process should be defined: elastic scattering on atom (in which the total kinetic energy of the colliding partners is conserved), or inelastic ionization process (which spends a part of the kinetic energy to overcome the ionization potential of an atomic electron to be ionized). Here we meet another choice, and further shall follow one of the branches of the algorithm: either modeling elastic or inelastic path.

In case of an elastic collision, one has to calculated the transferred energy dE via scattering angle (or vice versa), and change the parameters of the electron: its kinetic energy, coordinates, momentum, and go back to the starting point to repeat the whole algorithm with these new initial conditions. If the collision is inelastic, then there is one more intermediate step among those for the elastic case: one has to model how this process occurs. For this, we must sample which shell of an atom is ionized, and calculate the transferred energy to the electron, accounting for the ionization potential. Further, one should follow the same path as for the elastic case. Also, in a good algorithm, the second ionized electron must be included into the array of primary electrons, and to be followed in all its kinetics in the same manner, applying the same algorithm with its own initial conditions.

I would like to emphasis once again, that this is only one of many possible ways to construct a MC algorithm. Depending on a precision required in the model, the number of stochastic choices (random values involved[1]) can differ, the pathways may be diversified, or other processes can be included. The more connections between different values are included, the less random numbers are needed in the algorithm. For example, the scattering angle and

---

[1]Note, that here and further in the Dissertation, the random numbers are assumed to be uniformly distributed in the interval [0,1), unless indicated different limits or difference distribution law

the transferred energies can be given as independent random values [48]; on the other hand, one can account for the fact that they are interconnected, and calculating only one of them is enough to define the other one. Accounting for all possible connections would, in principle, lead to an absence of random numbers involved, which turns the Monte-Carlo scheme into an exact solution of the equations of motion (like Molecular Dynamic simulations).

2.3 Poisson distribution, particle scattering on random centers

Let us consider a bunch of particles with a flux Φ penetrating through a matter, consisting of randomly placed atoms. Now, let atoms be rigid balls with a cross-section σ, and the density of atoms is n_0. If the particle collides with an atom, the particle disappears from the bunch. Thus, the flux will be a random function of the depth $\Phi(x)$: after each collision the number of particle in the flux is decreasing by one $\Phi(x + \Delta x) = \Phi(x) - Q(\Delta x)$, where $Q(\Delta x)$ is the number of scattered particles per unit time per depth Δx. The particles are scattering the more often, the more particles are in the bunch, the bigger the atoms are, and the more of these atoms are in the matter, thus, $Q(\Delta x) = \Phi(x)\sigma n_0 \Delta x$.

The ratio of the number of collision to the number of incoming particles is thus

$$\frac{Q(\Delta x)}{\Phi(x)} = \sigma n_0 \Delta x = \frac{\Delta x}{l_0} \ , \tag{2.1}$$

where $l_0 = 1/(\sigma n_0)$ is called a mean free path of the particle.

Taking the limit of $\Delta x \to 0$, we obtain the differential equation for the flux:

$$\frac{\Phi(x + \Delta x) - \Phi(x)}{\Delta x} \to \frac{d\Phi(x)}{dx} = -\frac{\Phi(x)}{l_0} \ , \tag{2.2}$$

The solution of this equation is

$$\Phi(x) = \Phi_0 \exp(-x/l_0) \ , \tag{2.3}$$

where $\Phi_0 = \Phi(0)$. Therefore, the probability to travel the distance x without a scattering for a particle is written as follows:

$$P(x) = \frac{\Phi(x)}{\Phi_0} = \exp(-x/l_0) \ . \tag{2.4}$$

In the framework of the MC method, any probability is replaced by the random number, different for every event. Thus, replacing the probability $P(x)$ by a random number γ from $(0, 1]$, we obtain the following free path traveled until collision:

$$x = -l_0 \ln(\gamma) \ . \tag{2.5}$$

This Eq.(2.5) will be often used in the following chapters.

Calculating now the mean free path of a particle by the definition

$$< l >= \int_0^\infty x \frac{dP(x)}{dx} dx = l_0 \ . \tag{2.6}$$

we prove that the value $l_0 = 1/(\sigma n_0)$ introduced above indeed has a meaning of the mean traveled distance of a particle between collisions [48].

2.4   Gaussian distribution

Here we will not devise the gaussian distribution and the central limit theorem, which can be found in any textbook of probability theory (see i.e. [56]). We will start from the known gaussian distribution, and show the connection to the random numbers, which is used later in MC simulations.

Let's write the two gaussian distributions:

$$w_x(x) = \frac{1}{\sigma\sqrt{2\pi}} \exp\left(-\frac{x^2}{2\sigma^2}\right) \ , \ w_y(y) = \frac{1}{\sigma\sqrt{2\pi}} \exp\left(-\frac{y^2}{2\sigma^2}\right) \ , \tag{2.7}$$

where σ^2 is a dispersion of the gaussian.

The probability that a point $\vec{r}$ is in the area $da = dxdy$ is then

$$P(\vec{r} \in ds) = \frac{1}{2\pi\sigma^2} \exp\left(-\frac{x^2+y^2}{2\sigma^2}\right) dxdy \ . \tag{2.8}$$

Transferring it to the polar coordinates, we have

$$P(\vec{r} \in ds) = \frac{1}{2\pi\sigma^2} \exp\left(-\frac{\rho^2}{2\sigma^2}\right) \rho d\rho d\phi \ , \tag{2.9}$$

since $\rho d\rho d\phi = da = dxdy$. Thus, the probabilities for ρ and ϕ can be written separately as follows:

$$P_\rho(\rho) = \frac{1}{\sigma^2} \exp\left(-\frac{\rho^2}{2\sigma^2}\right) \rho d\rho \ , 0 < \rho < \infty$$

$$P_\phi(\phi) = \frac{1}{2\pi} d\phi \ , 0 < \phi < 2\pi \ . \tag{2.10}$$

Replacing the probabilities with the random numbers γ (index 1 and 2 note that the numbers are different), we have

$$\rho = \sigma\sqrt{-2\log\gamma_1} \ ,$$

$$\phi = 2\pi\gamma_2 \ . \tag{2.11}$$

Transferring equations 2.11 back to the Cartesian system, we obtain two independent equations, each of which gives the connection between the two random numbers $\gamma_{1,2} \in (0,1]$ to a point on the gaussian distribution:

$$x = x_0 + \rho\cos\phi = x_0 + \sigma\sqrt{-2\log\gamma_1}\cos\left(2\pi\gamma_2\right) \ ,$$

$$y = y_0 + \rho\sin\phi = y_0 + \sigma\sqrt{-2\log\gamma_1}\sin\left(2\pi\gamma_2\right) \ . \tag{2.12}$$

where now the central point (x_0 and y_0) of a gaussian is introduced [48].

These Eqs. 2.12 will be used in chapters 5 and 6 for modeling the laser intensity profile (determine the temporal profile of the density of photons).

Chapter 3

Electron kinetics in SHI tracks in dielectrics

As it was mentioned in the introduction, the Monte-Carlo methods are best applicable for absolutely uncorrelated systems of particles. This assumes a weak interaction between particles in the system under consideration and a negligibly small influence of quantum effects. These conditions are perfectly fulfilled for the case of highly excited electrons in a dielectric, when the absence of free-electrons provides the absence of correlated interactions between excited particles, while high energies allow to neglect quantum effects, like Pauli's exclusion principle and other correlation effects.

Thus, we will start from constructing a Monte-Carlo method for the case of high energy electrons in dielectrics. Within this chapter we will show how the Monte-Carlo algorithms can be constructed for the description of particle transport in solids, which processes must be considered, how they can be treated within the Monte-Carlo concept, and what are the limits of validity of such approximations. Finally, we will come to the application of the method to a real system and compare the results to experimental data. This chapter reproduces the Ref. [57].

3.1   Introduction to a Swift Heavy Ion beams physics

«Swift heavy ions (SHI) with energies higher than ~ 1 MeV/amu and masses higher than ~ 20 proton masses stimulate structural and phase transformations in nanometric vicinities of their trajectories when penetrating various solids. These effects occur in the electronic stopping regime, when the electronic energy loss of a projectile overcomes a certain threshold (~ 2 - 5 keV/nm in dielectrics), while the radiation damage produced by elastic recoils (nuclear stopping) is orders of magnitude too low to provide the observed structural modifications in tracks [28–35].

Spatial anisotropy, nanometric spatial and subpicosecond temporal scales,

as well as extremely high excitation of materials in SHI tracks supply with new tools for nanotechnologies [31, 36] and give new abilities for investigations of strongly non-equilibrium states of matter [37–41, 43–47]. Strong deviations from the equilibrium in excited SHI tracks can result in pathways of the relaxation kinetics which may be hardly described by ordinary macroscopic models based on local equilibrium conceptions [38, 45, 46]. Furthermore, analytical descriptions of the track kinetics usually neglect effects of holes created in different atomic shells during ionization of a media by a projectile. In addition to a high energy accumulated in these holes, their decay leads to creation of secondary generations of electrons and holes that affects considerably the kinetics of the electronic subsystem in a track.

Numerical simulations can provide detailed information [15, 49, 55, 58–66] necessary for adequate description of the kinetics of the electronic subsystem of a solid in the nanometric vicinity of the SHI trajectory. In the present work we apply Monte-Carlo simulations focused on the description of the early stage of the electronic kinetics in wide band gap dielectrics irradiated with swift heavy ions decelerated in the electronic stopping regime. These simulations cover the time interval from the moment of ion impact up to the typical timescales of radiative decays of holes in $K-$shells of target atoms (~ 30 fs). In addition to the initial spatial distribution of the energy deposited by the projectile, the investigations concentrate also on descriptions of the kinetics of spatial and temporal distributions of (a) excited free electrons having different momenta and energies as well as holes in different atomic shells, and (b) energy transferred into the lattice on these timescales.

We identify the processes governing the relaxation kinetics of the electronic subsystem in SHI tracks by a comparison of numerical results with those obtained in the spectroscopy experiments determining intensities of $K_\alpha L^n$ radiative transitions in irradiated silica [40, 41]. The importance of the interatomic Auger (Knotek-Feibelman) processes [67–69] for this relaxation is an unexpected result of the comparison.

We demonstrate furthermore a spatial propagation of the excitation front in the electronic and ionic subsystems from the projectile trajectory. We find high concentrations of holes in different atomic shells and high energy accumulated in these holes at times up to 10 fs. This indicates that models based on assumptions of the local equilibrium can be hardly applied to the femtosecond temporal scales of relaxation of the electronic subsystem in nanometric SHI tracks in dielectrics. »

3.2   Monte-Carlo method

«We use the Asymptotical Trajectory Monte-Carlo (ATMC) method [49, 55, 59] with the Binary Collision Approximation (BCA) for description of both elastic and inelastic scattering of a swift heavy projectile as well as for the description

of free electrons generated due to ionizations of the target atoms. In the framework of this method SHI and free electrons were treated as point-like particles having well-defined trajectories. For SHIs with energies $E_{ion} > 1$ MeV/amu this approximation is always valid. For electrons the approximation requires energies higher than $Ee \geq 100$ eV [49, 58–60, 65], however, the method is also used for lower energies of electrons [15, 49, 58–61, 65, 66]. As it will be demonstrated below, the classical treatment of electrons cannot affect considerably the energy relaxation in a track on femtosecond timescales, because on these timescales low energy electrons accumulate only a negligible part of the excess energy of the electronic subsystem transferred from the projectile.

In the algorithm applied here [15, 58], the velocities of primary free electrons generated due to ionizations produced by a projectile are determined at the first step of the simulation. Then, spatial spreading of these electrons and their elastic and inelastic scattering on atoms resulting in appearance of new free electrons are calculated event by event. At the same time we simulate Auger decays, which lead to redistribution of holes and creation of new secondary electrons. Modeling of elastic scattering of free electrons with atoms yields the energy transferred to the target lattice. Finally, averaging over the obtained ensembles gives the spatial distribution of electrons, holes, and their energies. The program runs many times to gain statistically trustful results.

3.2.1 Target and projectile

A solid dielectric target is assumed here as a uniform and randomly arranged distribution of atoms [15, 49, 55, 58–66]. The investigated times (≤ 10 fs) are too short for appearance of collective lattice oscillations and lattice atoms are presented in the model as dynamically independent during their collisions with a SHI and electrons [38, 70]. We assume also that the target lattice initially does not contain any defects, which cross-sections of interactions with free electrons or a SHI differ from those of lattice atoms. Creation of new stable lattice defects resulting from relaxation of electronic excitations is not considered in this research because it needs much longer times than the timescales investigated here (> 100 fs).

Because of high energies transferred to electrons from the projectile, we do not take into account the difference between excitations of target electrons to the continuum or to the conduction band. The electronic band structure of the target is not taken into account and at the beginning the target electrons are considered as occupying atomic levels characterized by their ionization potentials taken from [71].

We assume that only ionization of electrons from the atomic shells provides the projectile energy losses in a dielectric target. This assumption is based on (a) a lack of free electrons in the conduction band of dielectrics resulting in negligible dynamical friction of SHI due to interaction with free electrons as well as due to a plasmon creation in the conduction band [58, 60], (b)

negligible stopping of a swift heavy ion due to elastic collisions with target atoms, (c) absence of Cherenkov irradiation, (d) negligible Bremsstrahlung irradiation from SHI as well as from excited electrons due to probabilities orders of magnitude smaller than the probabilities of impact ionizations for typical ion energies considered here [28].

Because of the heavy mass of a projectile ($M_{ion} >> m_e$) and the perpendicular incidence, its trajectory is assumed to be a straight line and cylindrical geometry is applicable. For the calculations, the target is assumed to be a layer with a thickness of 10 nm with periodical boundary conditions.

The probability of ionization of the projectile electrons having orbital velocities higher than the SHI velocity is low due to adiabatic collisions of such electrons with lattice atoms. Therefore, after a number of collisions, a penetrating SHI reaches the equilibrium charge state keeping only fast electrons. The penetration depth when the projectile reaches the equilibrium charge state is called an equilibration depth. The equilibrium charge can be described by the Barkas formula [28, 59, 60, 72]:

$$Z = Z_{ion} \left[1 - \exp\left(-\frac{V_{ion}}{V_0} Z_{ion}^{-2/3} \right) \right] \ , \qquad (3.1)$$

Here, Z_{ion} is the atomic number of the projectile; V_{ion} is its velocity; $V_0 = \alpha c$ is the Bohr velocity; $\alpha = 1/137$ is the fine structure constant; and c is the speed of light. The formula (3.1) is valid for homogeneous targets [72]. The equilibration depth depends on the initial charge and velocity of the ion [73] and typically does not exceed ~ 100 nm [74–76], which is much shorter than the total penetration depth of SHIs in solids ($\sim 100\mu$m). We did not analyze effects of this thin surface layer and assumed that along the trajectory the projectile keeps the equilibrium charge depending on its velocity.

Silica (SiO_2) is chosen for simulations as the target. It has the density $\rho = 2.32$ g/cm^3 corresponding to the atomic density $n_t = 6.9 \times 10^{22}$ 1/cm^3. Calcium (Ca, $M_{ion} = 40 m_p$, $Z_{ion} = 20$) with the initial energies $E_{ion} = 5$ MeV/amu, 8 MeV/amu and 11.4 MeV/amu is chosen as the projectile. Such energy corresponds to the parameters of UNILAC accelerator (GSI, Darmstadt) [40, 41]. The velocity of this ion ($V_{ion} = 4.7 \times 10^7$ m/s for $E_{ion} = 11.4$ MeV/amu) is less than the speed of light in silica ($V_c^{SiO_2} = 1.94 \times 10^8$ m/s) resulting in absence of Cherenkov emission, as it was assumed above. According to Eq.(3.1), such Ca ions have the equilibrium positive charge $Z = 18.74$ resulting in energy losses of $S_e = 2.66$ keV/nm. A Ca ion with an energy of 455.6 MeV (11.4 MeV/amu) can transfer an energy up to $E_{max} = 24.8$ keV to an electron. This maximum energy E_{max} corresponds to the electron velocity $V_e^{max} = 9 \times 10^7$m/s $< V_c^{SiO_2}$ which is also less that the speed of light in quartz.

3.2.2   Ionization of atoms by a projectile

The following algorithm was used to obtain the parameters of collisions of a swift heavy ion with target electrons. In our multi-component target, the particular atom, with which the SHI is colliding, is chosen according to the shortest prospective free path among those calculated for all atomic species. Therefore, first, the path lengths between sequential collisions of the projectile and atoms of different species are calculated for the prospective collision. Second, the kind of a target atom is selected, and the impact parameter for the SHI collision with this atom is calculated. Finally, the quantum number and coordinates are generated for all electrons of this atom. As a result, the impact parameters for each electron of the atom and transferred energy to the atomic electrons interacting with the projectile during this collision are determined. The atom is considered to be ionized (and an electron to be free), when the calculated transferred energy exceeds the ionization potential for the analyzed electron. Otherwise, we conclude that no ionization occurs and no energy is transferred to this electron from the projectile.

In a homogenous target the distribution of the free path lengths l_{ion}^{α} between collisions of SHI with the α-th kind of atom (Si or O for our case) is described by the Poisson law giving the following dependence of the prospective free paths l_{ion}^{α} on random values γ_{α} [49, 55, 59] uniformly distributed in the interval (0,1]:

$$l_{ion}^{\alpha} = -\ln(\gamma_{\alpha}) l_0^{\alpha} \ , \tag{3.2}$$

The mean free path can be written as $l_0^{\alpha} = c_0 (n_{\alpha}\sigma_{\alpha})^{-1}$, where σ_{α} is the total cross section of scattering of a SHI on an $\alpha-$th atom; n_{α} is the volume density of such atoms; and c_0 is the fitting parameter taking into account the experimental scattering data for the used target [59, 60]. It should be noted that the mean free path should not differ significantly from the mean interatomic distance of the material.

Other methods of fitting of l_{ion}^{α} based on different variations of the collision cross-sections can also be applied. For example, it is possible to fit the impact parameter or its different combinations with the mean free path. We have analyzed such different methods. They gave the same results for the ion energy losses. Only small differences in the initial distributions of low energy electrons from the first generation of the free electrons were found. However, any differences vanish during relaxation already on subfemtosecond timescales. It was assumed that because of the short time (< 0.01 fs) of SHI interaction with a lattice atom, binary collisions of the ion with atomic electrons occur momentary when the distance between the projectile and the atomic nucleus is minimal (the Asymptotical Trajectory method [49, 55, 59]). The coordinates of atomic electron depend on the principle quantum number of the shell this electron belongs to. Due to the degeneracy of the atomic level, a number of electrons occupy the selected shell.

To describe the interaction between the projectile and an electron, we use a simplified semi-classical description. The underlying assumptions restrict the velocity of a projectile $V_{ion} >> Z_a^{2/3} V_0$ [28, 30, 33] and agree with the requirements of ATMC. The a-posteriori analysis of the obtained results confirms that the application of our comparably simple but computationally advantageous model is reasonable because small differences in the initial ionizations eliminated by relaxation processes in the exited electronic subsystem already on femtosecond scales (see the Results section).
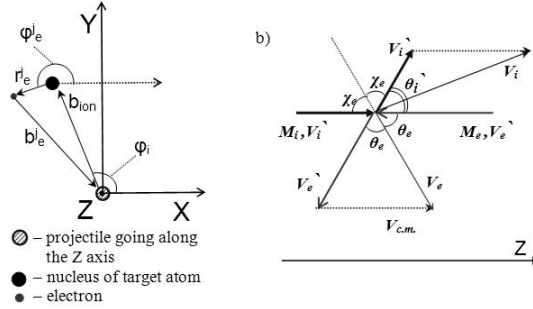
Figure 3.1: a) Scheme of the interaction of SHI with a target atom. The ion velocity vector V_{ion} belongs to the Z axis perpendicular to the figure plane. b) The kinematic scheme of the collision. Primed values correspond to the center-of-mass system. Nonprimed values correspond to the laboratory system.

According to this model the impact parameter b_e^j between the projectile and $j-$th electron of the selected atom ($j = 1, ..., Z_\alpha$, where Z_α is the atomic number of the $\alpha-$th kind of atom) is fixed by the distance b_{ion} between the projectile and the nucleus of the selected atom and the planar coordinates x_e^j, y_e^j of this electron [59] (see Fig. 1a):

$$b_e^j = \sqrt{(x_e^j)^2 + (y_e^j)^2}$$
$$x_e^j = b_{ion} \cos \phi_i + r_e^j \cos \phi_e^j \qquad (3.3)$$
$$y_e^j = b_{ion} \sin \phi_i + r_e^j \sin \phi_e^j,$$

where $r_e^j = a_0(n_\alpha^j)^2 / Z_\alpha$ is the Bohr radius of $j-$th electron; and n_α^j is its principal quantum number. The angle ϕ_i, fixing the position of the $\alpha-$th atom with respect to $x-$axis (Fig. 1a), is chosen as a random value ranging in the interval $(0, 2\pi]$. The angle ϕ_e^j lying in the (X,Y)-plane determines the position of $j-$th electron on its orbit at the moment of collision. This angle is fixed by the random value within $(0, 2\pi]$. All electrons of the atom are

analyzed, i.e. the index j changes from 1 to Z_α. In Eq. (3.3) and below in this section the index α is omitted because of similarity of the formulae for all kinds of atoms.

For the assumed homogeneous distribution of target atoms, the impact parameter b_{ion} realized in the traced collision of the ion with the selected atom was defined by the randomly generated value γ_i [59] as follows

$$\gamma_i = P(b_{ion}) = \int_0^{b_{ion}} 2\pi b \, db/(\pi b_{max}^2) = b_{ion}^2/b_{max}^2 \ , \tag{3.4}$$

Here $P(b_{ion})$ is the probability of the impact parameter value to be less then b^{ion}. It is commonly assumed that in the homogeneous model, b_{max} is restricted by the interatomic distance: $\pi b_{max}^2 = n_{at}^{-2/3} = d_{at}^2$ [59], resulting in the following dependence of the impact parameter on the random value γ_i

$$b_{ion} = \sqrt{\gamma_i} d_{at}/\sqrt{\pi} \ , \tag{3.5}$$

Eqs. (3.3) and (3.5) give the final form of the impact parameter b_e^j of the traced collision between the projectile and $j-$th electron on the Bohr orbit r_e^j of the selected atom

$$b_{ion} = \sqrt{(\sqrt{\gamma_i} d_{at}/\sqrt{\pi})^2 + (r_e^j)^2 + 2(\sqrt{\gamma_i} d_{at}/\sqrt{\pi}) r_e^j \cos(\phi_i - \phi_e^j)} \ , \tag{3.6}$$

According to the Eq. (3.6), the impact parameter $b_e^j (j = 1, ..., Z_\alpha)$ of $j-$th electron is fixed by (a) the random value γ_i related to the distance b_{ion} from the SHI trajectory to the nucleus of the selected atom which this $j-$th electron belongs to, and (b) the random angle $(\phi_i - \phi_e^j)$ between the radius-vectors of the nucleus of the selected atom and $j-$th electron.

The assumption about the classical interaction between the projectile and an electron results in the fact that the impact parameter b_e^j unambiguously determines the scattering angle χ_e^j and the energy E_e^j transferred from the SHI to the $j-$th electron. The scattering angle measured in the center-of-mass system (Fig. 1b) is determined by [77]

$$\chi_e^j = b_e^j \int_{r_{min}}^\infty \frac{dr}{r^2} \left[1 - \left(\frac{b_e^j}{r} \right)^2 - \frac{U(r)}{E} \right]^{-1/2} \ , \tag{3.7}$$

Here $U(r)$ is the potential energy of interaction (e.g. Coulomb potential), r_{min} is the shortest distance between SHI and the selected electron, and $E = E_{ion} m_e/(M_{ion} + m_e)$ is the projectile energy in the center-of-mass system.

Since the projectile is fast, dynamical screening effects cannot be established during a collision ($V_{ion} > d_{at}\omega_p$, where $\omega_p = (4\pi n_v e^2/m_e)^{1/2}$ is plasma frequency of valence electrons with a density n_v in a target). The dielectric function of a media related to this collision tends to the unity ($\epsilon(\omega, k) \to 1$)

[78–80] and the interaction potential can be written in the Coulomb form $U(r) = Ze^2/r$, where is the electron charge. In this case Eq. (3.7) gives

$$\chi_e^j = \arccos \left(\frac{Ze^2/(2Eb_e^j)}{\sqrt{1 + \left(Ze^2/(2Eb_e^j)\right)^2}} \right) \ , \tag{3.8}$$

When the velocity of SHI is higher than the electron orbital velocity, the electron scattering angle in the laboratory system θ_e^j is equal to the angle χ_e^j in the center-of-mass system (Fig. 1.b). This scattering angle θ_e^j is counted from the z-axis and belongs to the plane specified by the ion velocity vector and the position of $j-$th electron:

$$\theta_e^j = \arccos \left(\frac{Ze^2}{2E_{ion}b_e^j} \frac{M_{ion}+m_e}{m_e} \left[1 + \left(\frac{Ze^2}{2E_{ion}b_e^j} \frac{M_{ion}+m_e}{m_e} \right)^2 \right]^{-1/2} \right) \ , \tag{3.9}$$

The energy transferred to the electron is determined by this scattering angle [58] as follows

$$E_e^j = E_{ion} \frac{4m_e M_{ion}}{(M_{ion}+m_e)^2} \cos^2(\theta_e^j) =$$

$$4E_{ion} \frac{M_{ion}}{m_e} \left[\left(1 + \frac{M_{ion}}{m_e} \right)^2 + \left(\frac{b_e^j}{a_0} \frac{E_{ion}}{ZRy} \right)^2 \right]^{-1} \ , \tag{3.10}$$

Here $Ry = e^2/(2a_0) = 13.6$ eV is the Rydberg constant. Note, that at small impact parameters, in accordance to the conservation law, Eq. (3.10) yields the maximum of the transferred energy.

After the collision with the projectile the atomic electron was considered as free when the transferred energy E_e^j exceeds the ionization potential of this electron. The momentum of the emitted electron is uniquely determined by the momentum conservation law taking into account the initial momentum of the projectile and of the selected electron (the later is assumed as zero).

According to the assumption of momentary collisions of SHI with atoms, spatial propagation of all emitted electrons from the selected ionized atom starts at the same moment and ionization of any electron does not shift the energy levels occupied by other electrons during the collision [81–83]. Thus, ionized electrons are treated as independent particles with independent energy levels.

Because of the assumption of the equilibrium charge state of a penetrating SHI, we do not take into account possible interactions of created free electrons with this projectile such as capture or further ionization of SHI, fluctuation of charge or secondary scattering of free electrons with the projectile. Therefore, Fermi shuttle processes or creations of convoy electrons [84,85] are not taken into account in the presented model.

3.2.3   Spatial propagation of electrons and secondary ionization

When spreading through a target, free electrons generated by the projectile create secondary ionizations resulting in appearance of new free electrons as well as localized holes in different atomic shells. The kinetics of spatial propagation of free electrons is mainly determined by elastic and inelastic interactions of electrons with target atoms, interactions between free electrons, and their attraction by the positively charged track core. Efficiencies of these processes depend on the achieved parameters characterizing the excited electronic ensemble in the vicinity of SHI trajectory and their temporal and spatial evolutions.

In the present model we neglect interactions between free electrons because (a) the volume density of free electrons at distances larger than 0.5 nm from the projectile trajectory in dielectrics becomes too low and (b) the kinetic and potential energies are comparable only for slowest electrons (~ 10 eV) located in the nearest region to the trajectory at ~ 10 fs, and accumulating only a negligible part (< 5 %) of the energy lost by the projectile [15, 58, 60–66]. Also, such slow electrons cannot produce new ionizations of atomic shells. For the same reasons we do not take into account attraction between the positively charged track core and free electrons, which could affect only slow electrons [15, 58, 60–66]. Therefore, the trajectories of free electrons between collisions with atoms and atomic electrons are considered as rectilinear. Collisions of free electrons with atoms can be separated into two statistically independent processes, which are described by independent cross sections: (a) elastic collisions, which conserve the total kinetic energy of interacting particles, and (b) inelastic collisions where this energy changes. Inelastic collisions result in ionization of target atoms.

We neglected interactions of free electrons with already ionized atoms [15, 30, 49, 55, 58–66]. Such interactions are possible only for such densities of free electrons and ionized atoms which are comparable with the solid density. As it was mentioned above such high densities are realized only in the nearest vicinity of the projectile trajectory (a few angstroms) decreasing fast with increasing distance from the projectile trajectory. Due to low volume densities of free electrons we also do not take into account screening of the interaction potential of the traced free electron with a target atom or target electron, respectively, by other free electrons.

In order to calculate the scattering parameters of the traced collision of the selected free electron we, first, determine the realized mode of this collision (kind of interacting atom, elastic vs inelastic, interacting atomic electron). For this purpose, we use the algorithm similar to that applied for scattering of the projectile i.e. we calculate stochastic free path lengths for all possible scattering channels of the traced free electron and select the realized scattering channel as that having the shortest free path in this statistical sampling.

The free paths of free electrons for ionization of $\alpha-$th atom as well as for

elastic collisions are generated by a number of random values γ_β^α uniformly distributed in (0,1]:

$$l_e^{\alpha,\beta} = -\ln(\gamma_\beta^\alpha)l_{e,0}^{\alpha,\beta} \ . \tag{3.11}$$

Here α indicates an $\alpha-$th atom, $l_{e,0}^{\alpha,\beta}$ is the path length for the collision with a particle of kind β (symbol $\beta = e-e$ means the collision with atomic electrons, and $\beta = e-a$ used for elastic collisions with atoms), $l_{e,0}^{\alpha,\beta} = (n_\beta \sigma_\beta)^{-1}$ is the mean free path for the collisions with a particle of kind β, n_β is the volume density of particles β, σ_β is the total cross-section of interaction of the electron with particle of kind β.

The total cross-section of elastic scattering of a free electron with a target atom is taken in the form proposed by Mott, see i.e. [49], as follows

$$\sigma_{e-a} = \pi a_0^2 \frac{Z_\alpha(Z_\alpha + 1)}{\eta_c(\eta_c + 1)} \frac{Ry^2}{E_e^2} \ , \tag{3.12}$$

Here, η_c is the screening parameter of the atom by its own electrons:

$$\eta_c = 1.7 \times 10^{-5} Z_\alpha^{2/3} \left(\frac{m_e c^2}{2E_e} - 1 \right) \left(1.13 + 3.76 \frac{Z_\alpha^2}{\alpha^2} \frac{m_e c^2}{2E_e} \Big/ \sqrt{1 + \frac{m_e c^2}{E_e}} \right) \ . \tag{3.13}$$

Describing inelastic collisions, as it was mentioned above, we assume that (a) only the ionization of the electrons with ionization potentials I_j^α smaller than the kinetic energy of the traced free electron is possible, (b) the ionization cross-section of a bound electron depends only on the ionization potential [15, 49, 58–66, 86], and (c), according to the classical limitations used, atomic electrons are located in fixed points of their orbits during the collision with a free electron that restricts the energy of free electrons to $E_e \gg m_e V_0^2/2$.

The cross-sections of ionization accomplished by the emission of $j-$th electron of an α atom were calculated by Gryzinsky in Refs. [86–88] as:

$$\sigma_{e-e} = 4\pi a_0^2 \left(\frac{Ry}{I_j^\alpha} \right)^2 \frac{I_j^\alpha}{E_e} \left(\frac{E_e - I_j^\alpha}{E_e + I_j^\alpha} \right)^{3/2} \times$$

$$\left[1 + \frac{2}{3} \left(1 - \frac{I_j^\alpha}{2E_e} \ln \left(2.7 + \sqrt{\frac{E_e}{I_j^\alpha} - 1} \right) \right) \right] \ . \tag{3.14}$$

If all the prospective path lengths of the traced free electron for inelastic collisions with atomic electrons are larger than those for elastic collisions with atoms $(l_e^{\alpha,e-a} < (l_e^{\alpha,e-e})_{min})$ the current collision of the traced free electron was considered as the elastic one. In this case the scattering angle θ and the scattering plane angle ϕ were specified as random values ranging in $(0, \pi]$ and $(0, 2\pi]$, respectively. The transferred energy is unambiguously determined by the angle θ. Because of the small mass ratio, the relative part of the energy

transferred from free electrons to the lattice is small. However, this elastic scattering (a) affects considerably the spatial spreading of free electrons by changing their momenta and (b) results in initial lattice excitations at times shorter than those of atomic vibrations.

In the opposite case ($l_e^{\alpha,e-a} > (l_e^{\alpha,e-e})_{min}$) the traced electron scatters on the bound electron according to the shortest free path. The impact parameter necessary for ionization of an atom by an electron is about 30 times smaller than that for ionization by the projectile. Therefore, the probability of multiple ionizations of an atom by an energetic free electron can be neglected in our approach (more precise quantum-mechanical considerations of cross-sections confirm this simple conclusion [65]).

The energy transferred to the bound electron during the atoms inelastic interaction with the traced electron ranges in the interval $[I_j, E_e]$ and is fixed by the stochastic choice of the impact parameter. The scattering angles are determined by the energy and momentum conservation laws. The scattering plane is given by a random angle ϕ in the interval $(0, 2\pi]$.

Subsequent spatial propagation of secondary free electrons and their interactions with target atoms are described in the same manner.

3.2.4   Auger processes

In addition to free electrons, ionization of target atoms results also in the creation of holes in different atomic shells. Subsequent decay of these holes may occur via radiative decay, intra-atomic Auger processes as well as inter-atomic Auger (Knotik-Feibelman) processes at solid-like density of the target [67–69]. These Auger processes change the distributions of holes in different atomic shells and also increase the volume density of free electrons. Some of these new electrons will have enough energy to further ionize atoms. New holes appearing in deep atomic levels will generate new Auger cascades and radiative decay processes.

The distribution of Auger decay times t_{au} of $\alpha-$th kind of atom is described by the Poisson law $t_{au} = -\ln{(\gamma_{au})\tau_\alpha}$. For intra-atomic Auger processes we took the characteristic times τ_α for different shells of Si and O atom from the Ref. [89]. The electrons involved into the intra-Auger process of a fixed atom are chosen randomly from electrons of the upper atomic shells. The kinetic energy of an escaping Auger-electron from the selected atomic shell is determined by the difference between the energy released due to filling of a hole in the deeper shell and the ionization potential of this electron.

Inter-atomic Auger-process (Knotek-Feibelman) [67–69] can be realized only for solid-like densities of targets. Before this process both electrons, one which fills the hole in the deeper shell and the other one being emitted, belong to the upper shell of a neighbor atom located in the close vicinity of the atom containing the hole. The interatomic Auger-processes are especially important for atoms ionized by the projectile where multiple ionization results in a lack

of electrons on the upper shells of such atoms. For our case of a SiO_2 target, the only considered process corresponds to a transition of electrons from the $L-$shell of oxygen atoms to holes in the $L-$shell of neighboring silicon atoms. To the best of our knowledge, there is no data available of the characteristic time τ_α of this inter-atomic Auger process. Thus, this time was used as the second and last fitting parameter of the model.

For radiative decays of holes a similar procedure was applied using the characteristic times from Ref. [89]. However, we should note, that the radiative decays do not play a role here, because their relative probability is $\sim 5\%$ of the probability of Auger process [89].»

3.3   Results and discussions

3.3.1   Verification of the model

«The energy losses of Ca ion (11.4 MeV/amu) in SiO_2 calculated for $c_0 = 0.3$ (see Eqs. (3.2) and (3.3)) are are in good agreement with the theoretical Bethe-Bloch high energy limit [28–32, 49, 59, 90, 91] and with the standard codes `SRIM-2008` [91] and `CasP-4` [92]. The good agreement indicates that our model describes the ion energy losses correctly, even for low ion energies where it reaches its limits of validity.

A detailed analysis of the governing mechanisms of initial relaxation of the electronic subsystem of the SiO_2 in SHI track is made by comparison of our numerical results with the experimental data presented in Refs. [40, 41]. In these spectroscopy experiments ionization of deep shells of silicon atoms was investigated by measuring intensities of radiative decays of $K-$shell holes in atoms having different numbers n of holes in $L-$shell (KL^n-configurations).

Fig.3.2 demonstrates a very good agreement between the intensities of the experimental $K_\alpha L^n$ spectral lines for three different projectile energies (5 MeV/amu, 8 MeV/amu and 11.4 MeV/amu) and those calculated in the presented model. We use only one free parameter here, providing the best fitting: the characteristic time (60 fs) of the interatomic Auger (Knotek-Feibelman) process in which a hole in the L shell of Si atom and electrons in L shell of neighbor oxygen atoms are involved, as it was mentioned above (see sec. 3.2.4). This time is close to that of radiative decay of a hole in $K-$shell of a silicon atom (30 fs). It is important to note, that it is not possible to reproduce the presented experimental results without taking into account interatomic Auger process. The systematic deviations between calculated and measured intensities at $n = 0$ is observed, because only ionizations produced by a SHI are included in Fig. 3.2. In a real system, a small fraction of $K-$shell ionizations with completely filled $L-$shell (KL_0) is produced also by fast electrons, as it was discussed in Section 3.2 and will be included in Section 3.3.2.

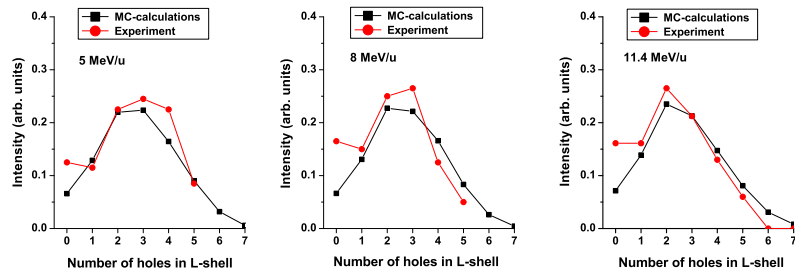To study the effects of different models of initial ionizations of a target

Figure 3.2: Calculated and experimental [40,41] spectra of radiative decays of holes in K-shell of Si atoms having also a number of holes in L-shell. The data are presented for silica irradiated with Ca ions with different energies (5 MeV/amu, 8 MeV/ amu and 11.4 MeV/ amu). The spectra are normalizaed to the total number of decays of silicon atoms.

made by SHI on the subsequent electronic kinetics, we have applied the cross-sections of multiple ionization by SHI, calculated in [93] instead of those calculated in the framework of the presented semi-classical model. Fig. 3.3 shows the comparison of the resulting intensities of $K_\alpha L^n$ spectra together with the experimental results. We see that already on the timescales of radiative decay of $K-$shell, i.e. on femtosecond timescales, differences in the initial ionizations are smoothed out to practically the same distributions of electronic configurations ($K_\alpha L^n$ spectra) which are in very good agreement with those observed in experiments. Thus, effects of small differences in the initial ionizations on the electronic kinetics completely vanish due to intensive relaxation processes at already a few femtoseconds after the projectile passage.

This good agreement between numerical and experimental results, together with the calculated energy deposited by SHI as well as negligible effect of small differences in initial ionizations, confirm that the presented approach using a semi-classical model with binary collisions provides a reasonable description of the excitation and relaxation kinetics of the electronic subsystem of dielectrics in SHI tracks.

3.3.2   The electronic kinetics

In the following we analyze in detail the electronic kinetics after impact of a Ca ion having the energy $E_{ion} = 11.4$ MeV/amu resulting in the energy losses of $S_e = 2.66$ keV/nm. Fig. 3.4 illustrates the radial dependences of the energy densities of free electrons, of the total energy of holes (in all shells of both kinds of atoms), and of the excess energy of the lattice at $t = 10$ fs after the projectile
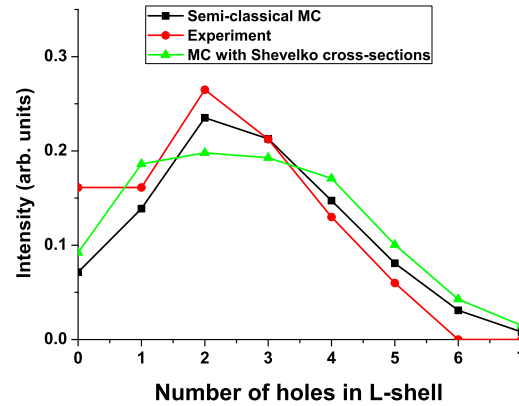
Figure 3.3: Comparison of the experimental [40, 41] $K_\alpha L^n$ spectra of silica irradiated with 11.4 MeV/amu Ca ions with those calculated in the framework of the presented semi-classical model and quantum model of multiple ionization [93].

passage. We have to note that, due to the features of the Monte-Carlo method, some statistical fluctuations can be observed at spatial scales comparable with the interatomic distance. The densities of electrons and ionized atoms in the track core inside the radius ~ 2.4 might be overestimated by up to about ten percents [58, 60] because we neglect interactions of free electrons with already ionized atoms. Fig. 3.4 demonstrates that about 0.1 % of the excess energy of free electrons is transferred to the lattice via binary collisions with atoms at a time ~ 10 fs which is much smaller than the time of atomic vibrations.

Fig. 3.5 presents the decrease of the total energy of free electrons due to conversion of a part of their energy into the energy of holes in different atomic shells. The kinetic energy of free electrons at the initial moment consists about 82 % of the energy lost by the ion, while 18 % of this energy is spent for ionization of atomic electrons. Already at $t = 1$ fs a considerable part of free electron energy has been spent to overcome the ionization potential during secondary impact ionization processes. At this time the kinetic energy of electrons is ~ 71.8 %, which means that about 28.2 % of the energy lost by the projectile is spent to overcome the ionization potential and thus considered to be contained in holes. At 10 fs after the projectile passage, potential energy of holes amounts already 63 % of the total energy deposited by the projectile. Therefore, models describing transformations of the excess electronic energy after SHI passage (e.g. [37, 45–47, 94]) should take into account redistribution of the energy accumulated in holes.

It should be noted that the total energy accumulated in holes in $K-$shells
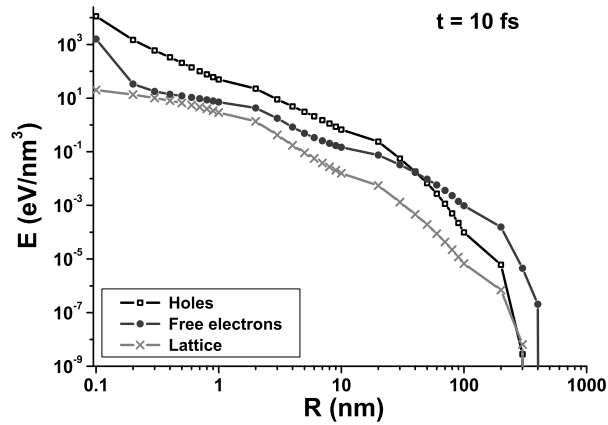
Figure 3.4: Spatial distribution of the energy densities of free electrons and all holes in different atomic shells as well as the density of the excess energy of the lattice at 10 fs after the passage of a 455.6 MeV Ca ion in SiO_2.
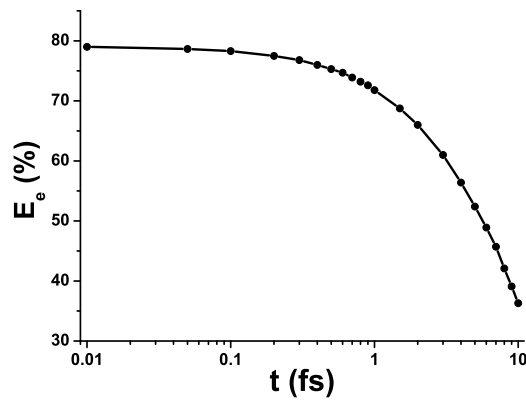
Figure 3.5: The temporal dependences of the total kinetic energy of free electrons in SiO_2 after the passage of a 455.6 MeV Ca ion.

consists only 1.7 % of the total energy of holes (or 1.16 % of the energy lost by the projectile) at $t = 1$ fs. The main part of the potential energy is accumulated in less energetic electronic vacancies. Energy release resulting from decay of these low energy holes takes place at times from tens of femtoseconds (the

shortest Auger process for $L-$shell) to hundreds femto- to picoseconds (for valence holes) after their appearance.

Figures 3.6.a and b show the transient distributions of the densities of free electrons and their excess energy, respectively. The distributions have well pronounced fronts moving out from the central region in the direction perpendicular to the ion trajectory, revealing ballistic spatial propagation of free electrons on femtosecond timescales.
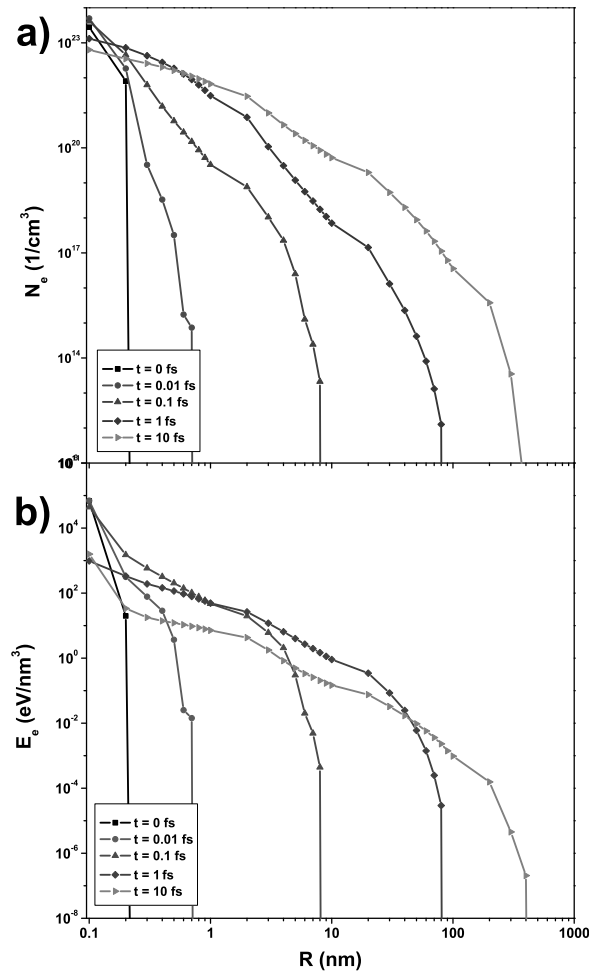
Figure 3.6: The spatial and temporal distributions of the densities of a) free electrons and b) their energy in SiO_2 after the passage of 455.6 MeV Ca ion.

The knowledge of the transient electronic density in the track enables us

to estimate the effect of interactions among free electrons on their kinetics. Indeed, the distance, at which the potential energy of interaction (Coulomb) between free electrons reaches ten percent of their kinetic energy, can be estimated as $l_{e-e} = 10e^2/E_e$ [95]. With this length we obtain a criterion to estimate a maximal electronic densities, at which the interaction among free electrons can still be neglected ($n_e^{cr} \sim l_{e-e}^{-3}$). For different characteristic electronic energies such critical densities are: $n_e^{cr} = 2.4 \times 10^{20}$ cm^{-3} for $E_e = 1$ eV; $n_e^{cr} = 2.4 \times 10^{23}$ cm^{-3} for $E_e = 10$ eV; $n_e^{cr} = 2.4 \times 10^{26}$ cm^{-3} for $E_e = 100$ eV. From Fig. 3.6.a we conclude that for electrons with energies above 100 eV the interaction among free electrons can always be neglected in description of the electronic kinetics in SHI tracks. For electrons with energies in the range of 10 eV, this is true except, perhaps, the very central region of the track core (of few angstroms) at ultrashort timescales. In contrast, for free electrons with lower energies the effect of electron-electron interaction may play a role. However, because these electrons accumulate only small part of the excess energy of the excited electronic subsystem, we neglect this effect.

The spatial distribution of the average kinetic energy of free electrons is shown in Fig. 3.7 for different instances of time after penetration of the projectile. Averaging was done for all free electrons inside a cylindrical layer between two neighboring points in the figure. The figure clearly shows that the fastest electrons tend to spatial separation from the slowest ones. Fast electrons eject from the track core already on femtosecond time-scales and bring out a part of the excess energy. A peak of the average energy distribution occur at times ~ 10 fs in the central region, where the initially highest concentration of holes has appeared (mostly created by the SHI impact, cf. Figure 3.11). This peak results from Auger decays of holes, increasing the density and mean energy of free electrons in the track core.

In order to investigate the spatial separation of electrons in more details, the ensemble of free electrons is divided into three groups with respect to their kinetic energy. Electrons with energies less than $1\%E_{max}$ formed the Group 1. Electrons with intermediate kinetics energies ranging in the interval $1\%E_{max} < E_e < 10\%E_{max}$ were attributed to the Group 2. Fast electrons with energies above $10\%E_{max}$ represent Group 3. Figs. 3.8-3.10 present the temporal and spatial variations of the number and energy densities of electrons, respectively, of all these groups up to $t = 10$ fs after the projectile passage. Fig. 8 shows the spatial distribution of these three groups of electrons after one femtosecond after the SHI impact. It clearly demonstrates the spatial separation of fast electrons on the front from the slow electrons which remain in the central vicinity of a projectile trajectory.

Fig. 3.9 demonstrates the energy density of the three electronic groups, where one can see that the considerable part of energy is brought out of the center by the fastest electrons. The propagation of these fastest free electrons (the third group $E > 0.1E_{max}$) is studied in Fig.10, showing the special electron density at different times. The figure reveals that the fastest free electrons
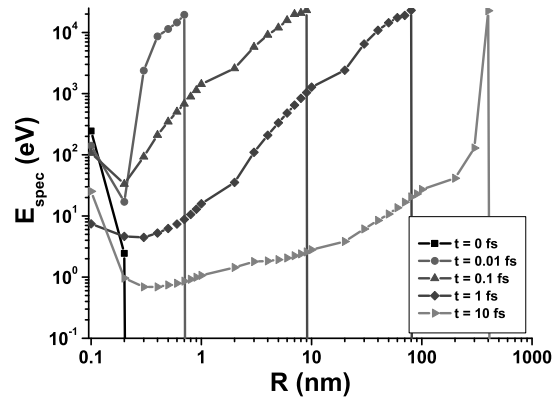
Figure 3.7: The spatial and temporal distributions of the mean energy of free electrons in SiO_2 after the passage of 455.6 MeV Ca ion.
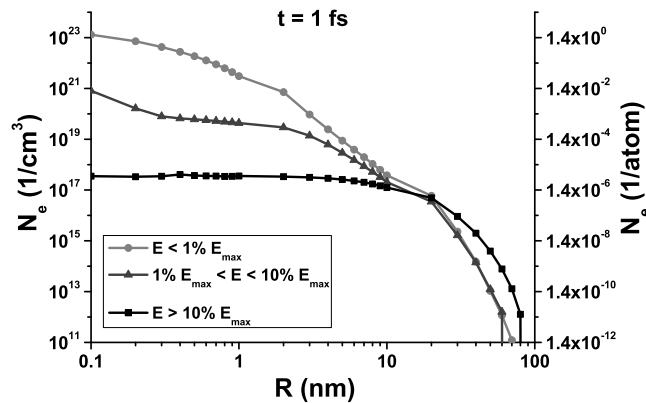
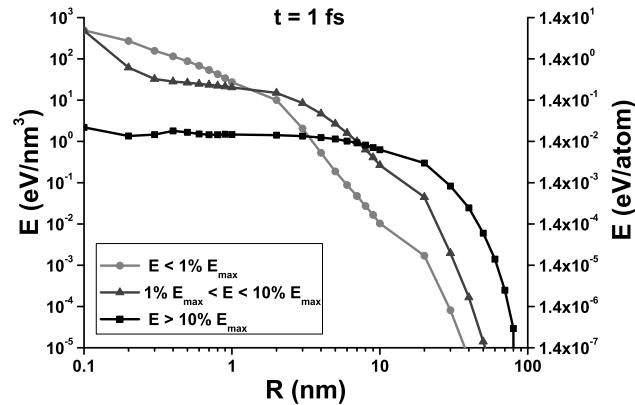

Figure 3.8: The spatial distributions of the densities of three groups of different energies of free electrons in SiO_2 after the passage of a 455.6 MeV Ca ion. See text for details.

from the third group have a pronounced ballistic propagation front, which cannot be described in terms of the diffusion model. On femtosecond timescale these fastest electrons accumulate a part of the excess energy of free electrons (Figs. 3.7, 3.9) and, therefore, spatial spreading of this energy cannot be described by heat diffusion. The possibility of the description of propagation of

such electrons in the frame of the "meso-diffusion theory" [45, 46, 96, 97], i.e. the intermediate stage between ballistic propagation and diffusion, requires additional studies which will be made in a future. Moreover, the observed differences between the kinetics of the electronic groups indicate that description of the complete ensemble of free electrons in terms of a unique temperature field is questionable at least at times up to 10 fs after the projectile passage.

Figure 3.9: The spatial distribution of the energy density of three groups of different energies of free electrons in SiO_2 after the passage of a 455.6 MeV Ca ion. See text for details.

In our model, holes are considered as localized on atomic shells and spatial propagation of the hole density occurs only due to ionizations of target atoms by spreading free electrons. Fig. 3.11 presents the spatial and temporal distributions of the density of holes in $L-$shell of silicon atoms. The ballistic front of the hole density can be observed, which follows the electron spreading. The distributions of holes in different atomic shells at $t = 10$ fs are demonstrated in Fig. 3.12. One can conclude from this figure, that the largest part of the excess energy of holes is accumulated within the valence band (represented by M-shell of silicon and $L-$shell of oxygen), as it was already noted above. The subsequent kinetics of holes occurs via interplay of two mechanisms: (a) impact ionizations by free electrons, and (b) the Auger and Knotek-Feibelman decays. The radiative decays play a minor role here, since their relative probability is $\sim 5\%$ of the probability of Auger process [89].»

3.4 Summary

«We apply a Monte-Carlo approach to describe the ultrafast electronic kinetics in swift heavy ion tracks in a dielectric (after penetration of a Ca^{+19} ion with
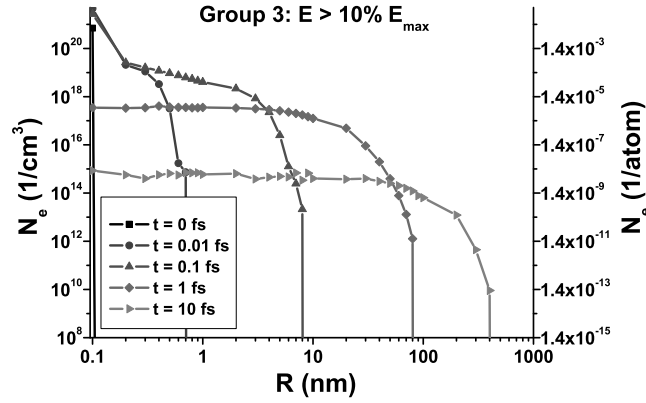
Figure 3.10: The transient spatial distributions of the number density of electrons constituting the third group (with energy of $E > 10\% E_{max}$) in SiO_2 after the passage of 455.6 MeV Ca ion.
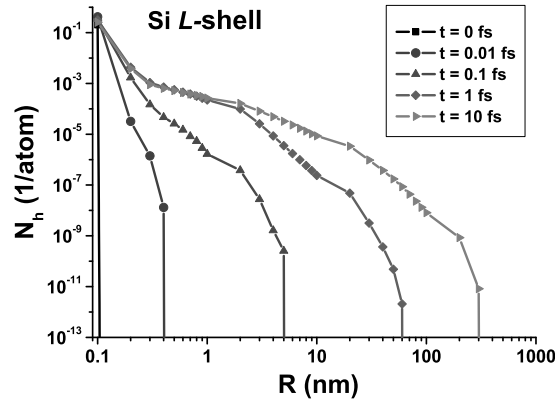

Figure 3.11: The spatial and temporal distributions of the number density of holes in L-shell of Si-subsystem in SiO_2 after the passage of a 455.6 MeV Ca ion.

the energy of 11.4 MeV/amu in SiO_2). The spatial and temporal distributions of the number and energy densities of free electrons and holes in different atomic shells, respectively, as well as the excess energy of the lattice at times up to 10 fs after the passage of the projectile are obtained.

The results have shown that the propagation of excited free electrons and
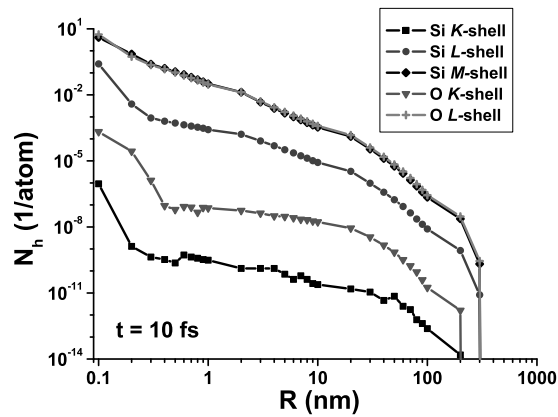
Figure 3.12: The spatial distribution of the number density of holes in different shells after 1 fs in SiO_2 after the passage of a 455.6 MeV Ca ion.

their mean energy occurs ballistically, which means that their mass and energy transport cannot be described by the classical diffusion and heat diffusion equations on femtosecond timescales. Therefore, descriptions of the initial kinetics (< 10 fs) of the electronic subsystem in SHI tracks based on the conceptions of local thermal equilibrium, particle diffusion and heat diffusion are questionable.

At 10 fs after the SHI passage, a large part of the transferred energy is accumulated as a potential energy of holes. This energy is not thermalized as well, and its redistribution has to be taken into account when describing the electronic kinetics.

By comparison with spectroscopy experiments it is demonstrated that the electronic kinetics can be described well taking into account intra- and inter-atomic (Knotek-Feibelman) Auger processes of holes relaxation. Due to this relaxation, the fine details of the initial ionization have a negligible influence on the further kinetics of the electronic subsystem. The radiative spectra calculated taking into account inter- and intra-atomic Auger processes, are in good agreement with experimentally observed ones.»

Within this chapter we demonstrated a straightforward way to develop a Monte-Carlo algorithm for the description of particle transport in solids. It is perfectly applicable for high energy electrons, but no matter how high the excitations of the electrons are at the beginning, sooner or later they end up in low energy states losing their energy into the solid. At this point one has to consider processes beyond uncorrelated methods. In the next chapter we will propose a combination of different methods applicable on different timescales: Monte-

Carlo method for short times, and the so-called Two Temperature Model for longer times, when electrons have already lost most of their energy. In the chapters 5 and 6 we will demonstrate how the Monte-Carlo method itself can be extended to account for correlation effects.

Chapter 4

Combination of Monte-Carlo approach with the Two Temperature Model

In the previous chapter we constructed the Monte-Carlo algorithm describing the excitation of the electronic subsystem of a dielectric by swift heavy ions. Comparisons with experimental results allowed us to conclude that the MC model describes well the behavior of the electronic subsystem at short timescales. However, when electrons are losing their energy to a few eV energies, the main approximations made at the beginning do not hold well anymore: the potential energy of interaction between particles becomes comparable with their kinetic energy, the quantum effects start to play a role, the collective interactions take place instead of purely binary collisions. All these effects are limiting the applicability of standard MC methods.

If we are interested in describing the full process of modification of solids under high energy deposition, we have to trace the energy transfer from initially excited electrons to the lattice and take care of the behavior of the heated lattice. The characteristic times of the lattice heating are typically some picoseconds. Thus, we have to create an adequate model applicable on such long timescales. In this chapter we propose an idea of combination of two different models, each of which takes care of its own time-domain. The considerations made in this chapter are based on the works [98,99]. All the calculations with the Two Temperature Model were performed by O. Osmani.

4.1   Introduction

As it was already briefly mentioned in the chapter 3, the « [98] phenomenon of track creation is often explained in terms of a two temperature model (TTM) commonly called the inelastic thermal spike model [37]. Within this model both, the electronic as well as the phononic system, are described via two heat diffusion equations coupled by an exchange parameter. While the primary energy loss of the ion is used as a source of energy for the electronic system,

the phononic system is heated indirectly by electron-phonon coupling. This leads to a local heating of the lattice which may result in a molten area. The thermal spike model is successfully applied for reproducing experimentally observed track radii and damage thresholds [37, 47, 100, 101].

However, in order to explain the experimentally observed effects of the SHI irradiation, the parameters used in the TTM approach, like the electronic diffusivity and the electron-phonon coupling parameter, need to be handled with care. These parameters are often not known. The difficulty is due to the variable electron density in excited dielectrics, thus these parameters depend strongly on transient excitation dynamics. A reliable theory considering complete excitation dynamics is needed to compute these quantities. Additionally, the TTM is based upon thermodynamical equations, and it is questionable wether the system is actually in equilibrium. The electron-electron collision time is in the femtosecond regime, and the TTM may be applied after about 100 fs [21] to describe the energy exchange between electrons and phonons which occurs on the timescale of a few picoseconds [14, 102]. The difference between these timescales requires special attention when choosing the appropriate theoretical model.»

« [99] In order to explain the observed effects of SHI irradiation as formation of nano-hillocks on the surface, creation of stable point-like defects (color-centers), it was found that the parameters of TTM need a special treatment, which would confine the energy inside a narrow track halo for timescales orders of magnitude longer than those given by the usual TTM [37, 45, 47, 94]. For these reasons, electronic confinement usually is introduced via a temperature-dependent electronic diffusivity [47, 94] and by fitting on electron-phonon coupling constant [94]. In other works the energy confinement in lattice was introduced by changing the shape of thermal equation from diffusive (parabolic) equation to a heat-wave (hyperbolic) equation [45]. Both ways of fitting are linked to the same problem of the timescales.»

« [98] However, the physical origin of this energy confinement has not been further studied. In order to follow the dynamics of SHI irradiated insulators we have performed classical Monte-Carlo simulations (MC) which are capable to describe the excitation and transport of the electrons even at highly non–thermal conditions. The output of these MC calculations is then used as initial conditions for a TTM run to compute the lattice heating. This model reveals the physical origin of the energy confinement in the track core as an energy storage in holes and followed by the release of the energy via Auger processes and electron-hole recombinations.»

« [99] We have performed Monte-Carlo (MC) simulations of the irradiation of a solid insulator (SiO_2) with a swift heavy ion (Ca^{+19}, $E = 11.4$ MeV/u, $dE/dx = 2.7$ keV/nm). Following combination of the Monte-Carlo method with Two Temperature Model (MC-TTM) allows to investigate these questions of electronic confinement. The results of our MC-TTM reveals a new physical view and explains the timescale problems mentioned above, by taking into

account the energy storage in holes and following release of the energy via Auger processes and electron-hole recombinations.»

4.2   Model

For the Monte-Carlo part of the modelling, we use the same method as described in Chapter 3. Let us briefly remind the basic idea of the method. After that we will come to the description of the Two Temperature Model and to the connection between these two methods.

« [98] The general idea of our developed algorithm is as follows: first, we calculate the free path length between collisions of the ion with the target atoms; then multiple ionization occurs for each collision which results in the creation of the first generation of free electrons. Second, we determine the path lengths between all possible following collisions for all free electrons with the other bound electrons in different energetic states; then the bound electron corresponding to the shortest possible path length is ionized and the transferred energy is calculated. Consequently the mean free path and time for each electron, i.e. for electrons with different energies are also obtained. Each ionization of a bound electron leads to the creation of a hole. The possibility of hole decay by Auger recombination and thus further creation of secondary electrons is also included in the MC simulation. We will see later that this process plays a crucial role for the energy confinement mentioned above. The MC algorithm is repeated many times and finally averaged over the statistics.

We assume perpendicular incidence for SHI and neglect its nuclear stopping. Therefore we use a cylindrical geometry with periodic boundary conditions. The projectile is considered as a point-like particle with an equilibrium charge state according to the Barkas formula [28, 58, 60]. SHI penetration through the homogeneous media is described with a Poisson law for a free path between series of collisions. For solids this mean free path can be chosen equal to the mean interatomic distance [49, 59, 60, 63]. During the collision of SHI with an atom, the electrons of the atom are placed randomly around the nucleus according to their energy levels. The impact parameter between the projectile and the atomic nucleus is chosen randomly within the interatomic distance [59]. According to this impact parameter, the energy transferred to every electron is calculated [58]. The ionized electrons are treated as independent particles, i.e. the energy transfer and angles of emission of electrons are uncorrelated [49, 59, 60, 63]. If this energy exceeds the ionization potential of the certain electron, this electron is ionized, otherwise, no energy transfer takes place and no free electron is created. The scattering angle is explicitly determined by the transferred energy, and the polar angle is randomly uniformly distributed within the interval $[0, 2\pi)$.

For the subsequent electronic propagation, in contrast with SHI, elastic collisions with atoms must be included. Therefore, for electrons there are two

channels of energy losses: elastic and inelastic. The free path of an electron is defined by the shortest path realized according to Poisson laws for every possible collision: elastic collisions with every kind of atoms of target, and inelastic collisions with bounded electrons on different energy levels of every kind of atoms. Mean free paths of elastic collisions are calculated with Mott's cross-section of electronic scattering [49], that depends on the energy of electron and the atomic number of colliding atom. The scattering angle is defined by this transferred energy, and the polar angle is chosen from the interval $[0, 2\pi)$. For low energy electrons there is also another possibility for energy loss related to scattering on phonons [49, 103], this energy exchange is left for the following calculation with two temperature model. Mean free path of inelastic collisions are calculated using Gryzinski's ionization cross-section [60, 86–88], which depends only on the energy of the traced electron and ionization potential of a bound electron. The secondary generated electrons can then travel and scatter in the same manner [15, 58, 104].

For Auger-recombinations of holes the Poisson law for the time of decay is applied [15], with a characteristic time different for each atomic shell of each kind of atoms [89]. After the time of the decay is calculated, the electron that is getting the excess energy is chosen. Its final energy is given by difference between the energy released by electron filling the hole in deeper shell and its own ionization potential, and corresponding momentum is chosen uniformly within the solid angle. For solid targets it is also possible to have an interatomic Auger-processes, or so called Knotek-Feibelman processes [67], when electrons filling the hole and being ionized are coming from the neighboring atom to the one which has a hole. This process is important for the holes made by SHI, since after multiple ionization of an atom there is lack of its own electrons. The characteristic times of such processes are assumed to be equal to usual Auger recombination times.»

« [99] Following every particle and then averaging over the statistics we determine spatial and temporal distributions of particles and their energies. When electrons demonstrate a diffusive behavior instead of ballistic propagation, at this moment the calculations are switched from MC to the two temperature model.

Spatial distributions of temperatures of electron and of the lattice are taken from the corresponding energy distribution obtained by MC simulation. Then the TTM equations are given in the following way:

$$\frac{\partial T_e(\vec{r}, t))}{\partial t} = \nabla(D_e(T_e)\nabla T_e(\vec{r}, t)) - g \cdot (T_e(\vec{r}, t) - T_i(\vec{r}, t)) + S(\vec{r}, t), \quad (4.1)$$

$$\frac{\partial T_i(\vec{r}, t))}{\partial t} = D_i \triangle T_i(\vec{r}, t) + g \cdot (T_e(\vec{r}, t) - T_i(\vec{r}, t)) \quad (4.2)$$

where $T_e(\vec{r}, t)$ is the temperature of electrons, $T_i(\vec{r}, t)$ is the lattice temperature, $D_e(T_e)$ is the temperature dependent electronic diffusivity [47].» The

lattice diffusivity of solid SiO_2 is cgosen to be $D_i = 0.0084$ cm^2/s [107]; the parameter g is the electron-phonon coupling constant; and $S(\vec{r}, t)$ is the source of energy to the electronic subsystem.

O. Osmani developed the following numerical realization of the TTM. « [98] For the numerical description the crystal is discretized and equations (4.1) and (4.2) are solved fully three dimensional using the finite difference method. During the simulation the system is in contact with an infinite large heat bath at room temperature (assuming the experiment is performed at room temperature) serving as boundary conditions. However electrons with higher energy than the work function of the solid can escape the surface removing energy from the system. To take that into account we apply open boundary conditions for the electronic system at the surface allowing energetic electrons to be emitted into the vacuum.

This set of heat diffusion equations is coupled via the electron-phonon coupling parameter g, which determines the amount of energy transferred from the electrons to the phonons per unit time and volume. It is evident that this parameter plays a key role, as it governs the heating of the lattice. However, this parameter is difficult to come by, as only limited experimental data is available. Also the electronic diffusivity D_e poses a problem. It determines the amount of energy that is transported away from the point of release (i.e. the position were the electron was ionized). This transport will effectively limit the amount of energy that is locally available in order to heat the lattice above the melting point. Experimental data on this property is lacking. Although one can extract this number from resistivity measurements for instance, such kind of measurements often do not reflect the transient electronic excitation during the irradiation.

The electronic system is heated at the same rate the passing ion loses its energy. This can be calculated using the SRIM code [105]. The transferred energy enters eq. (4.1) in the source term S and in the present notation is formulated in terms of a temperature increase. It is therefore it is necessary to convert the excitation energy into an electronic temperature. This can be done by assuming that the electrons behave like a diluted free electron gas and using that the internal energy of the electrons is related to the temperature by $E = \gamma T^2/2$ where γT is the specific heat capacity of the free electron gas:

$$\gamma = \frac{1}{m_e} \frac{\pi^2}{2} \frac{n_e k_B}{T_F}$$

with n_e the free electron gas density, m_e is the electron mass, k_B the Boltzmann constant and $T_F = 1.04 \times 10^5$ K the Fermi temperature.

The electronic diffusivity is a function of the temperature (see results and discussion section) which is a function of the coordinate $D_e(T_e(\vec{r}))$. Therefore the gradient of the heat flux occurs in Eq. (4.1). In contrast, the lattice diffusivity can be regarded as constant, thus the corresponding term in Eq. (4.2)

appears in a simplified form.» The electronic «parameters entering eq. (4.1) and (4.2) are obtained as an output of the MC part of the model, see below.

As mentioned above, it is important to take into account the energy redistribution related to holes [108, 109]. The holes may decay via the Auger recombination. In this process, the recombination energy is released to an electron. Thus, these recombinations act as an additional source of energy for the electronic system, which is governed by a certain characteristic recombination time. Assuming an exponential decay of the holes we can write this source term as:

$$S_h(\vec{r}, t) = E_h(\vec{r}) \cdot (1 - e^{-t/\tau}) \tag{4.3}$$

Here $E_h(\vec{r})$ denotes the initial excess energy of the hole at position $\vec{r}$ and τ is the characteristic decay time. Therefore the effective source-term in eq. (4.1) heating the electronic subsystem can be written as $S(\vec{r}, t) = S_h(\vec{r}, t) + S_{SHI}(\vec{r}, t)$ where $S_{SHI}(\vec{r}, t)$ is the energy introduced to the electronic system by the primary ion.»

4.3 Results and Discussion

« [98] As a model system we choose the irradiation of solid SiO_2 by a Ca^{19+} ion with a total energy of 11.4 MeV/u which corresponds a resent experiment [110]. By means of Monte-Carlo simulation we was found that only after a time of approximately 1 ps after the ion impact the electronic behavior can be treated as a diffusive, thus the electronic system is assumed to be thermalized. Therefore a description based upon thermal equations is only valid at later times. This thermalization time is found by studying the transport behavior and the distribution of electrons for different times and radii concentric around the ion track. Therefore this time of 1 ps is considered as the starting time of the TTM calculations, using the output of the MC simulation as initial conditions.

In our simulation we find that the total energy of holes amounts to $\approx 82\%$ of the energy transferred by the SHI. According to eq. (4.3), these holes act as an additional source of energy for the electronic system. Due to the fact that a *major* fraction of the transferred energy is released with delay the heating of the lattice is prolonged to picosecond timescales. We also observed that the radial dependence of the electronic distribution plays a key role in the description of SHI induced track creation. High energetic electrons are escaping from the central track region creating slower electrons in their wake. As a consequence the electronic temperature is spatial dependent, and the time of equilibration for electronic and lattice temperatures will differ for different radii.

The benefit of our combined approach is that parameters needed for the TTM can be calculated within the MC approach. Here we will demonstrate
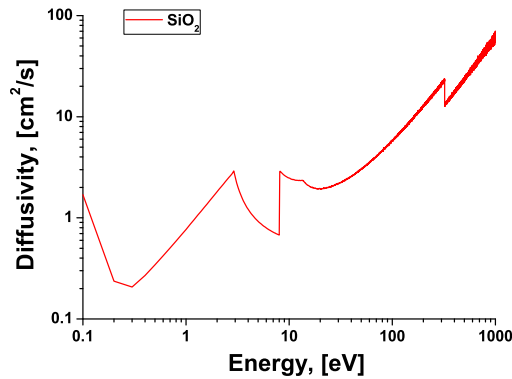
Figure 4.1: Diffusivity of electrons vs. the electronic energy calculated within binary collision approximation.

this for the electron phonon coupling parameter g and for the electronic diffusivity D_e. As was mentioned before the mean free path λ and the velocity $v(E)$ of the electrons with the energy E are prescribed in the MC part of this calculation. Using the well known expression $D = v\lambda/3$ we obtain an energy dependent electronic diffusivity $D_e(E)$ for SiO_2. This energy dependence can be transformed into a temperature dependence as was stated in the previous section.» The electronic diffusivity $D_e(E)$ shown in figure 4.1 exhibits different peaks. The low energy behavior (electrons below 10 eV) is determined by the electron-phonon scattering rates, extracted from Ref. [111]. That kinky behavior accounts for many effects [111]: it includes scattering on accustic and optical phonons, and the band structure of SiO_2. At different energies, different channels of scattering play a role: at very low energies (below ~ 1 eV), the accustic scattering is dominant; then the optical phonon takes the dominant role; and after ~ 5 eV again accustic-scattering start to dominate. So, overall it shows kinks and changes of the behavior. On the energies of 10 eV to 15 eV, the electron-phonon scattering rates are joint with the electron-atom scattering, which is described with the Mott's cross-section as was stated above (and discribed in more details in the Appendix). This gives for larger energies increase of $D_e(E)$. The sharp decrease of the diffusivity at high energies corresponds to the ionization potential of Si atoms. Thus, electrons with energies below 20 eV are localized around the track core.

Note that both quantities calculated here, D_e and g below are presented for a single particle. To apply them for a statistical ensemble, one has to average them over a Fermi distribution with given transient temperature.

« [98] We will now evaluate the electron phonon coupling parameter g. The coupling parameter describes the amount of energy transferred from the electrons to the lattice per unit time and volume. From the MC calculation we know the time between collisions between the electrons and the target atoms.
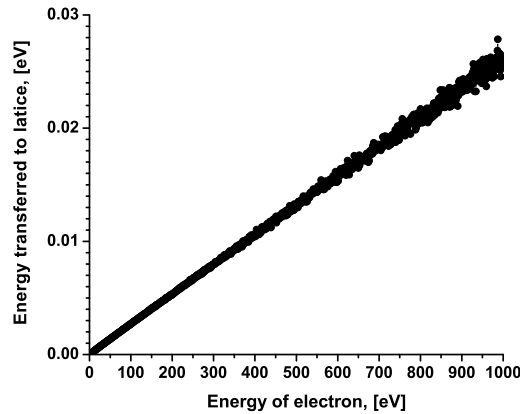
Figure 4.2: Energy exchange between electron and atom.

The transferred energy is calculated between electrons and atoms within the binary collisions approximation. As single particle trajectories are calculated, the volume in which this energy is transferred is the volume of one atom [1]. This gives us g in units of eV·(fs Å^{3}K)$^{-1}$; transferring to more common units yields a electron phonon coupling constant of $g \approx 10^{18}$ J·(s m^{3}K)$^{-1}$ for SiO$_2$, which is on the order of values for coupling parameters that were extracted for metals [94, 112, 113] and is reasonable also for laser-excited dielectrics [14].

The energy transfer from the electrons to the atoms is shown in figure 4.2. The scattering of the data at higher electronic energies is due to lack of statistics at these energies.

With the electron diffusivity $D_e(T_e)$ and the electron-phonon coupling parameter g all crucial material parameters entering the TTM are thus extracted out of the MC part.»

« [99] We stop the calculations where the electronic and lattice temperatures are equilibrated in the central region of 4 nm, which corresponds to the typical radius of a SHI track. This time is found to be $t \simeq 40$ ps, as can be seen on the Fig.4.3, where the electronic and the lattice temperatures for the central regions are presented.

The introduced source term S_h and the temperature-depended electronic diffusivity $D_e(T_e)$ confine the electronic energy for a longer period of time. In contrast with previous assumptions [47, 94], this is not a confinement in the sense of a stationary electron gas, but rather a repeated energy emission into an electronic subsystem by a hole relaxations at distinct places via Auger processes or recombinations.

The result of the calculation shows also that the melting temperature of the lattice is reached in the radius of around 4 nm from the projectile trajectory,

---

[1]Which is, however, not well defined value, ranging in between the volume defined by the Bohr atomic radius and volume of the unit cell in the solid
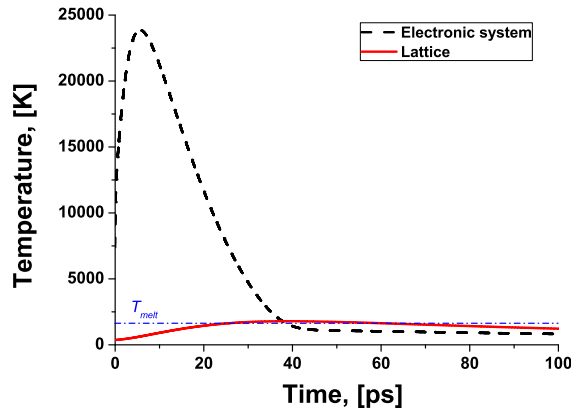
Figure 4.3: Transient electronic (dashed) and lattice (solid) temperature in the central region of the track. Melting temperature is included as a dash-dot line.

leading to an effective molten area.

This track radius is in a very good agreement with experimentally observed tracks, which proves the applicability of the created MC-TTM model for description of the swift heavy ion tracks problem.»

4.4 Summary

« [98] We developed a combination of the Monte-Carlo method with a two temperature model (MC-TTM) to describe the track creation processes in dielectric targets after swift heavy ion irradiation. Within the MC part of the calculations all necessary (and experimentally inaccessible) material parameters are computed so that no fitting is needed in the frame of the TTM. Especially the electron phonon coupling parameter is extracted which is an important material dependent parameter. The results of the combined MC-TTM model show that the energy storage in holes and secondary electron creation by the first generation of ionized electrons as well as by Auger decay of holes has to be taken into account. The Auger decay of holes plays a key role as an energy source of the electronic system, acting as a delay and thus confining the energy at the place of its initial excitation, i.e. in the vicinity of the track core. It can be accounted for by means of an additional source term in the heat diffusion equation.»

« [99] It was found that all processes in SHI tracks are significantly prolonged due to energy storage in holes via secondary electrons creation by first generations of ionized electrons. This secondary electron creation plays a very important role as a storage and later source of the energy, that can be described with an additional term in a heat diffusion equation related to holes. The delay

caused by this energy storage leads to an electron-lattice equilibration time of the order of 40 ps.»

« [98] Final structural modification of the material calculated with MC-TTM appeared to be in a radius of $\sim$ 4 nm, which is in very good agreement with experimental data. The new method presented here will prove helpful in predicting ion track properties for any other dielectric material as well.»

For the case of highly excited electrons, it was possible to combine two different models applicable on different timescales. This allowed us to describe the SHI excitation of dielectrics, and to make general conclusion on the physics of the process. However, for a case of lower excitation energies, this simple method is not working anymore – for excitations on the order of a few hundreds or a few tens of electron-Volts, the correlation effects play a role from the very beginning of the excitation process. This is an important point for materials excited with an ultrashort laser pulse in a ultraviolet to soft X-ray energy regime. How to include effects of the band structure, the Pauli's principle and some correlation effects into the Monte-Carlo model will be described in the next two chapters.

Chapter 5

Monte-Carlo simulation of VUV-XUV femtosecond laser pulse irradiation of semiconductors

In the previous chapters we have demonstrated how the Monte-Carlo algorithm can be applied for highly excited electronic systems of solids. We also have proposed a way how to deal with a systems beyond the limits of applicability of the classical MC methods – the MC model could be successfully combined with the thermodynamical approach on longer timescales. This was possible to do for highly excited electrons, with initial energies in a range up to several keV and higher.

Now we will focus on lower energies of electrons, on the order of few tens to few hundreds of eV. In this energy domain, which is typical for a new generation of femtosecond lasers, the usual Monte-Carlo concept is not so easily applicable. However, some modifications of the method allow to apply it in this case as well. In the present chapter the quoted parts are reproducing the article [114].

5.1   General aspects of laser irradiation of solids

« Experiments with lasers in the visible range have shown that the ultra-short laser irradiation of semiconductors produces observable modifications of the material's surface, such as the formation of nanobumps and the creation of molten regions [1–4]. With the invention of femtosecond lasers, which have a pulse duration comparable with characteristic times for processes in the electronic subsystem of the material, nanometric spatial and femtosecond temporal scales have created new possibilities for nanotechnologies, microma-chining and medical surgery. The many potential uses of intense femtosecond laser pulses in applications have stimulated fundamental theoretical and experimental investigations of strongly non-equilibrium states of matter [5–15]. The first experiments with the free-electron laser in Hamburg (FLASH), a

laser that provides pulses of femtosecond duration in the VUV to XUV energy regime, opened a pathway to promising new areas of fundamental research and technical applications [16–20].

In this new range of photon energies that was not previously accessible by experiments, there remains a lack of data about the primary response of the material to irradiation. Therefore, theoretical investigations are necessary to predict and interpret experimental observations. Such theoretical investigations must consider the range from the very first energy absorption event to the final phase transitions and structural modifications of the target.

Ultrashort laser pulses allow access to fundamental electronic processes in the solid because the pulse duration is comparable to the characteristic femtosecond timescale for collisional processes such as electron-electron interactions and electron-lattice collisions. The kinetics of the excitation and relaxation of the target can be divided into a set of processes separated temporally. Due to the mass difference between electrons and ions, excitation of the electronic subsystem by a laser pulse and the subsequent creation of second-generation free electrons occurs much faster (some femtoseconds, $\sim 10^{-15}$ s, or the duration of a pulse) [14, 21] than other processes such as energy exchange with the lattice and the cooling of excited electrons, which both take up to $\sim 10^{-11}$ s [22–27]. The processes in the electronic subsystem play a fundamental role because they provide the initial conditions for subsequent energy dissipation. Thus, these processes are of essential interest for all material behaviour - from the initial light absorption to further energy dissipation and the eventual phase transitions of the target in the form of melting or a transformation to warm dense matter [5, 10, 14, 23, 24].

In our studies, a Monte-Carlo method (MC) with binary collision approximation (BCA) [15, 58–60, 104, 115] is applied to describe the kinetics of electronic excitation in a semiconductor that is irradiated with a femtosecond laser pulse. The number of excited and ionised electrons, the energy of these free electrons and the energy distribution function were calculated as a function of time for a 10 fs FWHM Gaussian laser pulse in solid silicon. Laser and target parameters were chosen according to experiments performed with FLASH at DESY in Hamburg [20].

The recently introduced concept of an *effective energy gap* (EEG) [15] makes it possible to estimate the free electron density created due to high-intensity, high-energy laser pulse irradiation. In contrast to former models, which applied only to long timescale experiments [116–122], our concept focuses on the statistical behaviour of quasiparticles in ultrashort timescales.

Here, we extend and generalize the EEG-concept, analyzing influence of different processes involved for different photon energies and intensities, and give limits of the validity of the concept.»

5.2   Monte Carlo method

« In our model, we consider the following electronic processes: photoabsorption by bound electrons, impact ionisation by free electrons, and Auger-like processes within the valence band (so-called Coster-Kronig transitions or impact ionisation by holes). We neglect the radiative decay of electronic vacancies and electron-hole recombinations because they usually require longer times than those allowed by the timescales investigated here [81, 82]. Interactions among ionised electrons were also neglected because their typical density is low in comparison with the electron density in the valence band [15, 59, 60].

The basic idea of the numerical model is as follows: first, we simulate the penetration of the photons with a density corresponding to the intensity envelope of the laser pulse. For each photon, the penetration depth is calculated. If this penetration depth is within our simulation box, the photon is considered to be absorbed and to have given its energy to a randomly chosen electron. Second, this ionised electron can then perform secondary ionisations. To simulate this process, the free path is calculated according to the ionisation cross-section. At the end of this free path, the traced electron exchanges energy with a randomly chosen valence electron. This process proceeds by ionisation of the second electron, which can then also travel further and perform secondary ionisations itself as long as it has a sufficiently high energy. At the same time, the holes that remained after the ionisation can decay by Auger-like processes and also create free electrons. We simulate these three main processes by following each particle event by event during and slightly after the laser pulse. »

5.2.1   Target and photo-ionisation processes

« In the present work, the solid silicon target is considered to be a homogeneous isotropic arrangement of atoms with a density of $n_{at} = 4.5 \cdot 10^{28}$ m^{-3} and with an electronic density of states (DOS) corresponding to solid silicon [123, 124], see figure 5.1. Note in figure 5.1 that the deep atomic shells L_1, $L_{2,3}$ and K have energies of 100 eV, 148 eV and 1839 eV [71], respectively; these shells are not shown. We chose a Gaussian shape for the temporal intensity distribution of the laser pulse. Further excitation parameters of the laser pulse were chosen to mimic experimental data [20]: the energy of the photons was $\hbar\omega = 38$ eV, the intensity of the laser pulse was 2 J/cm^2 (unless otherwise indicated), and the full width at half maximum of the duration of the laser pulse was $\tau_L = 10$ fs with a total duration numerically cut off at 25 fs.

The number of absorbed photons can be calculated if the fluence and the attenuation length for a photon travelling in solid silicon (presented in figure 5.2) are known. The data were extracted from the references [28, 125].

The probability of multiphoton absorption is proportional to

$$J_l^2(e\vec{E}_L\vec{q}/(m_e\omega^2))$$

[126], where J_l are the Bessel functions of the first kind, l is the order of the function and indicates the number of absorbed photons (for positive integer l), e is the electron charge, $\vec{E_L}$ is the laser field amplitude, and $\vec{q}$ is the momentum change of the electron from the collision with a third partner during the photoabsorption process. The laser field amplitude can be estimated by the fluence [14]. For our range of fluences and the VUV-XUV photons, the probability of two-photon absorption is approximately two orders of magnitude lower than the probability of one-photon absorption. As fluence increases, the two-photon absorption probability increases and only approaches the one-photon absorption probability at a fluence of approximately 50 J/cm^2. Thus, in the present work, we consider only one-photon absorption processes.
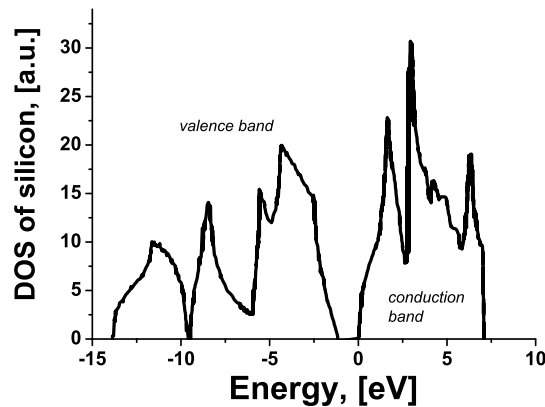
Figure 5.1: Density of states of solid silicon as given in [123, 124]. The deep atomic shells considered in this work (L_1, $L_{2,3}$ and K, with energies of 100 eV, 148 eV and 1839 eV, respectively) are not shown in this figure.

For the simulation, we chose a cube of silicon with a size of $10 \times 10 \times 10$ nm^3. The considered cube is assumed without free surfaces, thus we use periodical boundary conditions. It should be noted that electron emission from the surface might change the transient number of free electrons and their energy distribution. However, the mean free path for electrons with energies of the order of tens of eV in silicon is typically on the sub-nanometre scale [127]. Thus, our assumption of periodic boundaries for the simulation box means that we do not consider the effect of a several nanometre thick surface; we are instead interested in the general processes that occurred in the bulk.

The initial energy distribution of electrons was chosen to be represented by an empty conduction band and a completely filled valence band, which corresponds to the given density of states in figure 5.1 [123, 124]. The energy scale

for free electron kinetic energy starts at the bottom of the conduction band ($E = 0$ eV in figure 5.1). All electrons above the final 'outermost' state of the conduction band (~ 7 eV, figure 5.1) are treated as free electrons (i.e., as belonging to the continuum but still inherently in the crystal). All free electrons within the conduction band and the continuum are treated with the parabolic dispersion law with all effective masses equal to the free electron mass. Thus, we explicitly include the DOS of the material but not the detailed band diagram itself. The main influence on the results presented below comes from Pauli blocking, therefore, we account for the real density of states of silicon in detail, while the band structure is used only for the preliminary analysis (described in section 5.2.2) and does not enter the modeling. This approximation also considerably simplifies the numerics and makes the calculations significantly less time-consuming.

Interactions of every single photon with bound electrons were simulated event by event. The probability of interaction with every single electron from different energy states is determined from the relative cross-section. The details of the numerical algorithm can be found in [104]» and in chapter 3.
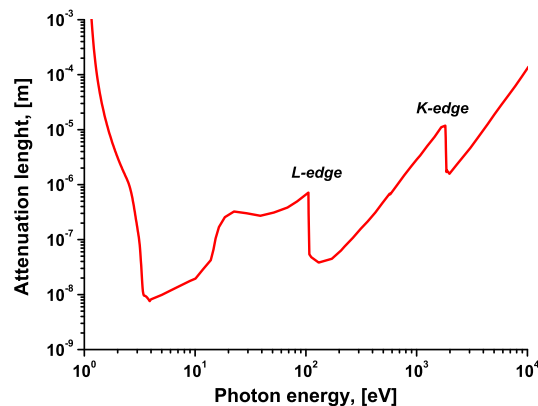
Figure 5.2: Attenuation length of the photon inside a solid silicon target. The low energy data are taken from the ref. [125], and the high energy data are extracted from [28].

« The pure cross sections for photoionisation of electrons in different energy levels within the valence band are considered to be equal, which is a fairly good approximation in this energy interval [28]. Differences were introduced only by having different densities of electrons in different levels, according to the DOS-function: the valence band was discretised and each discrete interval was normalised according to the total number of electrons, which yields the relative concentration values for electrons in different discrete energy intervals in the

valence band. The conduction band was discretised in the same manner. L and K atomic shells are represented as delta-function energy levels containing a corresponding number of electrons.»

5.2.2   Band structure analysis of secondary processes: impact ionisation and Auger decay

« Secondary electrons are ionised by impact ionisations and Auger decays to deeper shells (i.e., Coster-Kronig transitions) within the valence band. For these processes, momentum- and energy-conservation are simultaneously taken into account in accordance with the real dispersion laws of the material. Conserving these quantities leads to a strong reduction in the probability of secondary electron ionisation. Thus, to analyse the processes of secondary electron excitation, the electronic band structure of the material must be taken into account. The band diagram [124] and examples of energy- and momentum-conserving secondary processes are shown in figure 5.3. An analysis of the impact ionisation process corresponding to an initial state with one electron each in the conduction and valence bands and a final state with two electrons in the conduction band (see figure 5.3, where an electron e_1 ionises a second electron e_2, dashed arrows) shows that this process required a minimum kinetic energy for the initially free electron of $E_{\mathrm{e}}^{min} = 1.2$ eV. This energy is approximately equal to the indirect energy gap of silicon, Egap = 1.15 eV, as shown previously in [128]. Electrons with energies less than the value of E_{e}^{min} cannot initiate impact ionisation. Therefore, an electron with energy $E_e > E_{\mathrm{e}}^{min}$ can only perform secondary ionisations until its energy becomes less than the minimum energy of this process, which, in this case, is the real indirect energy gap of the material, E_{gap}.

Similarly, for an Auger-like (Coster-Kronig) secondary electron creation corresponding to an initial state with one hole and one electron in the valence band and a final state with one electron in the conduction band and a hole with higher energy in the valence band (see figure 5.3, where a hole h in the valence band ionises an electron e_A to the conduction band, solid arrows), we obtain a minimum initial energy for a hole in the valence band of $E_{\mathrm{h}}^{min} = -3$ eV, as measured from the bottom of the conduction band. Therefore, holes of higher energies than -3 eV cannot create a secondary electron and will remain stable on femtosecond timescales.

These limiting values of energies for electrons, E_{e}^{min}, and holes, E_{h}^{min}, must be taken into account in all subsequent analyses of secondary electron ionisation. Obviously, they strongly depend on the band structure of the considered material.»
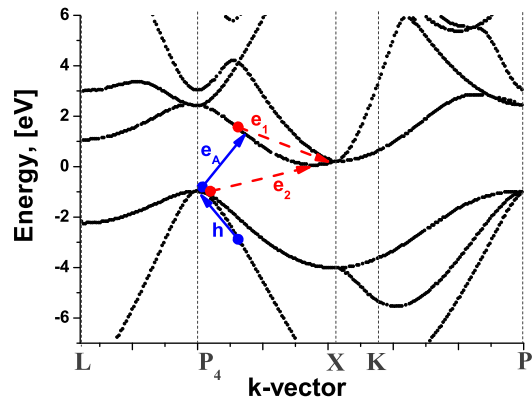
Figure 5.3: Band diagram of solid silicon taken from [124]. The schemes of impact ionisation and Auger-like processes are included, see text. We sketch these processes corresponding to the minimum energies of the ionising electron and hole, respectively.

5.2.3 Modelling of secondary processes

« The following algorithm was applied to determine the interaction parameters realised in a collision between a free electron in the conduction band and a bound electron in the valence band (impact ionisation). First, the path lengths are determined for all possible subsequent collisions of the chosen free electron with bound electrons in different energy levels of the valence band. The bound electron to be ionised is then chosen based on the shortest length. Finally, the transferred energy is calculated. As a result, the free path, the duration of the motion and the energy loss of the chosen electron are obtained. This scheme is used to describe the dynamics of all the excited electrons.

For randomly arranged atoms, the distribution of path lengths for a series of collisions with bound electrons can be written in an exponential form [59, 104]. The total cross section of impact ionisation for a particle at a discretised energy interval of the valence band can be determined by the expression obtained by M. Gryziński [86–88], which depends only on the ionisation potential of the electron. All cross sections σ of interactions are multiplied by a Pauli factor $w \sim f_v(1 - f_c)$, where f_v is the distribution function of electrons in the valence band and f_c is the distribution function of electrons in the conduction band. Both distribution functions are taken with respect to the energy levels of electrons, which participate in the traced collision. By including this factor, the expression for the mean free path automatically takes into account Pauli's principle: if there are no free states in the discretised interval, the cross-section is zero. In that situation, the mean free path tends to infin-

ity, and such a collision becomes impossible [104]. The energy transferred to a bound electron with ionisation potential I_e during an interaction with an electron of kinetic energy E_e lies within the interval $[I_e, E_e]$ and is fixed by the randomly chosen impact parameter according to the following expression: $\Delta E_e = E_e \left[1 + (b/a_0)^2 \cdot (E_e/(2Ry))^2\right]^{-1}$, where ΔE_e is the energy transferred to the bound electron, b is the randomly chosen impact parameter between a free electron and the selected bound electron, $a_0 = 0.53$ Å is the Bohr radius and $Ry = 13.6$ eV is the Rydberg constant [58].

This scheme assumes that impact ionisation and laser field interactions are independent processes. Generally, that might not be the case: the presence of a strong laser field can influence electron-electron collision processes [129, 130]. This influence is particularly important for low-frequency (i.e., visible light) very intense laser pulses where the field is so intense that it can be treated in the classical limit. However, for VUV-XUV photon energies and our analysed fluences, the laser-electron interaction is of a purely quantum nature. It is an essential point that electrons can gain energy from the laser field only in units of $\hbar\omega$. Thus, the processes of electron-electron interactions (impact ionisations) and photoabsorption can be treated as independent [14, 21, 126].

We note that as the photon energy decreases, multiphoton absorption becomes increasingly important. For photon energies of ~ 10 eV and a fluence of 2 J/cm^2, the two-photon absorption probability already equals the one-photon absorption probability. Thus, for even lower photon energies, the laser field becomes classical. However, this effect is neglected in the present work because we are focusing on the VUV-XUV range.

For Auger-like processes within the valence band (Coster-Kronig transitions), the exponential law for the decay time can be applied with characteristic times assumed to be equal to those obtained in [89]. The DOS and Pauli's principle are taken into account in the same way as for the electron impact ionisation process. The electron (hole) enabling the Auger-like transition and the electron being ionised are chosen randomly from among the electrons in the valence band.

The subsequent dynamics of the secondary electrons produced by the first generation of free electrons and holes and their interactions with the valence electrons were also taken into account in the same manner.»

5.3   Results and Discussion

5.3.1   Energy and density of excited electrons

« As a result of the numerical algorithm described above, we obtained the transient energy distribution of electrons and holes, which enabled us to study their transient dynamics. Figure 5.4 represents the energy distribution of electrons in the conduction band (positive energy) and holes in the valence band

(negative energy) in Si at different time points during the irradiation. Curves were normalised to the final number of absorbed photons.

The first curve shows a time t=0 fs, which corresponds to the absorption of the very first photon. One can see that before secondary processes start (just after absorption of the first photon), this distribution reflects the band structure of the material: electrons from the valence band are shifted to the continuum by adding the photon energy (E_{ph} = 38 eV in the presented case), while at the same times holes appear at the corresponding energy in the valence band. Then, electrons and holes start to redistribute their energy.

There are two competing mechanisms of energy redistribution: the absorption of photons during the laser pulse, which increases the total energy and the number of free electrons and holes, and secondary ionisations, which are responsible for decreasing the energy of free electrons and shifting the distribution to low energy states just as Auger processes shift the distribution of holes to lower absolute values of energy. The spikes on the curves show that the density of states influences the energy distribution at all times during irradiation.
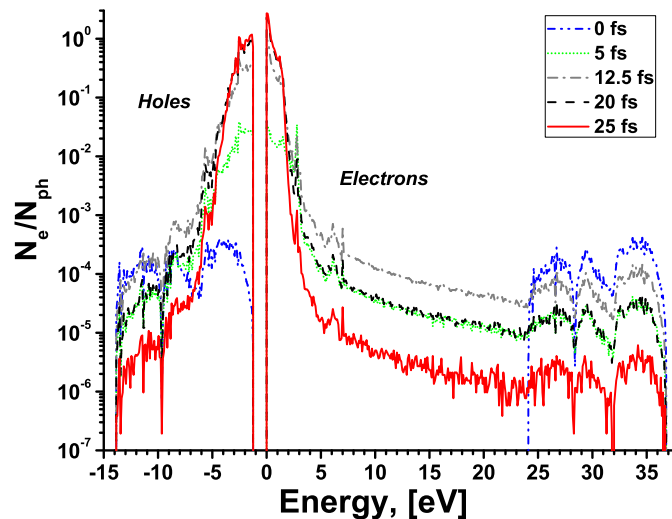
Figure 5.4: Transient energy distribution of free electrons in the conduction band and holes in the valence band. The fluence of the laser pulse is 2 J/cm^2 and the photon energy is 38 eV.

By integrating over all positive energies, we obtain the total kinetic energy of the electron gas during the laser pulse irradiation (figure 5.5). The energy shown in this figure is normalised to the total energy provided by the absorbed photons. The shape of the curve reflects the two competing mechanisms mentioned above. During the laser pulse, electron energy increases

due to photoabsorption while impact ionisations and Coster-Kronig decays decrease the energy - even for times longer than the pulse duration of 25 fs. Figure 5.5 demonstrates that the final kinetic energy of the free electrons is much less than the total energy provided by the laser pulse. An essential part of the energy ($\sim 65\%$) is spent to overcome the ionisation potential and is held as potential energy (i.e., the energy of holes).
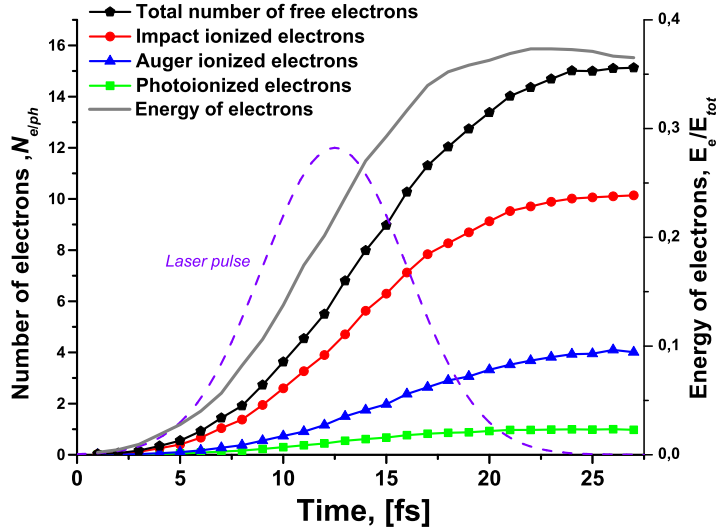
Figure 5.5: The total energy of free electrons in the conduction band normalised for the total absorbed energy (right ordinate). The number of free electrons created by different processes during the laser pulse irradiation and normalised per number of absorbed photons are also presented (left ordinate). The intensity envelope of the laser pulse is added as a dashed line in arbitrary units.

Figure 5.5 also shows the transient number of free electrons during the irradiation together with the laser pulse intensity envelope in arbitrary units. We calculated the temporal evolution of the number of free electrons ionised by direct photon absorption, electron impact and Auger-like processes, respectively. The number of electrons increased very quickly during the laser pulse because the time between two impact ionisation events is much shorter than the characteristic time of the problem. The collision time for an impact ionisation can be estimated as $t_{e-e} \sim l_e/\langle v_e \rangle \sim (n_e \sigma \langle v_e \rangle)^{-1} \sim 10^{-16}$ s, where l_e is the mean free path of excited electrons, n_e is the density of bound electrons in the valence band, σ is the cross-section of impact ionisation and $\langle v_e \rangle$ is the mean velocity of free electrons. Therefore, the maximum increase occurs exactly when the laser intensity (and thus the photoionisation probability) has

its maximum. Electron-electron impact ionisation is the dominant process for free electron generation, which differs from the irradiation of dielectrics with visible light [6,14]. Auger-like processes also play a significant role in secondary electron production, as shown in the same figure. Due to these secondary processes, each photon excites about $N_{e/ph} = 15$ electrons (cf. figure 5.5, where the primary excited electrons create around 10 secondary electrons by impact ionisation and 4 secondary electrons by Auger-like transitions).

Experimentally, the transient electronic density can be measured on a femtosecond timescale, for instance, by measuring the reflectivity with a pump-probe technique [13].»

5.3.2 Effective energy gap

«To estimate the number of ionised electrons, it is commonly assumed that each electron with or above a certain critical energy performs an impact ionisation. Using the band gap of the material considered here, this assumption leads to $N_{est} = \hbar\omega/E_{gap} = 32.6$ electrons per photon, which drastically overestimates the number of excited electrons compared to the present calculation. Such overestimation was also found experimentally decades ago [116], and several models were proposed for a better estimation of the number of free electrons (see the description of theoretical models in [119] and numerical models in [131] and the references therein). One of the most common models involves the application of the *direct* band gap of the material [117]. However, impact ionisation, as well as Auger-like processes, are restricted by energy *and* momentum conservation [14]; therefore, they generally take place as *indirect transitions*, as shown in figure 5.3. Thus, the direct band gap has no physically justified meaning for impact ionisation and appears as a fit parameter.

Our calculations reveal that the discrepancy in earlier estimations is caused by the fact that electrons are located in more than just the highest state of the valence band and are ionised into more than just the lowest state of the conduction band. To calculate the number of ionised electrons, we introduced the concept of an *effective energy gap* (EEG) [15]. For the present case of solid silicon irradiated by a laser pulse with a photon energy of 38 eV, it can be estimated as $E_{EEG} = \hbar\omega/N_{e/ph} = 2.62$ eV.

Using the above-described Monte-Carlo approach, we calculated the number of ionised electrons at different photon energies of the incident laser pulse (figure 5.6). For comparison, we also present the experimental results for similar parameters taken from [116] (red circles) and a typical numerical model [131] (green triangles). As one can see, our calculations coincide well with the experimental results, while the difference between the experimental data and other models is significant (it can be seen even more clearly in figure 5.7, which will be introduced below). This discrepancy is due to the fact that earlier theoretical works were not focused on ultrashort timescales; previous models to calculate the 'pair creation energy' (PCE) neglected the
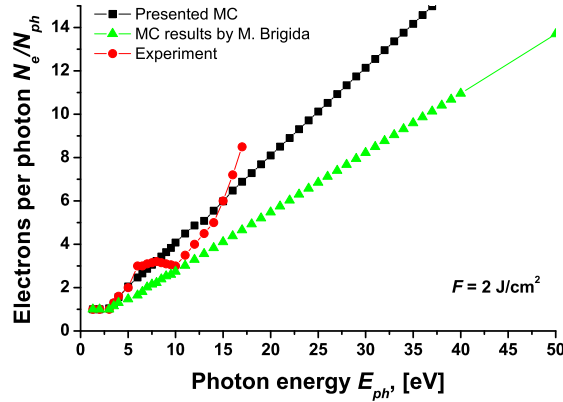
Figure 5.6: Number of ionised electrons as a function of photon energy. The black squares represent results of the Monte-Carlo simulation. The red circles are the experimental results taken from [116], and the green triangles are results of earlier calculations from [131].

temporal dependence of the free-electron density [119], which is essential in femtosecond timescales (i.e., in timescales before a detailed balance is established and while the electron density is changing significantly).

It should be noted here that, in the case of low photon energies and high intensities, the interaction with a laser field may influence the electron-electron impact ionisation process and thus change the number of free electrons. Furthermore, the intense laser pulse combined with the strong degree of ionisation may also influence the band structure and the DOS of the target, which, in turn, affects the electronic dynamics. Both mentioned effects should be treated carefully if one is interested in intense visible light irradiation; however, they may be justifiably neglected for the higher photon energies in the VUV-XUV range.

Generally, in femtosecond timescales and for VUV-XUV photon energies, the EEG can be expressed as

$$E_{\mathrm{EEG}} = \langle E_{\mathrm{e}} \rangle + E_{\mathrm{gap}} + \langle E_{\mathrm{h}} \rangle \tag{5.1}$$

where $\langle E_{\mathrm{e}} \rangle$ is the mean kinetic energy of ionized electrons and $\langle E_{\mathrm{h}} \rangle$ is the mean energy of holes.

By averaging the kinetic energy of electrons over the electronic distribution presented in figure 5.4, we found that the mean kinetic energy at the end of the laser pulse was approximately equal to half of the band gap. This result can be understood as follows: an electron with kinetic energy higher than a

certain minimum energy $E_e > E_{\mathrm{e}}^{min}$ quickly performs secondary ionisations. As was shown in the Model section, the minimum energy necessary for impact ionisation in the case of silicon is equal to the indirect energy gap $E_{\mathrm{e}}^{min} = E_{\mathrm{gap}}$. Therefore, all electrons with energy $E_e > E_{\mathrm{gap}}$ will produce secondary electrons until their energy falls below E_{gap}. In femtosecond timescales, all the electrons end up with energies between 0 and E_{gap}. Thus, the mean kinetic energy of a free electron after the laser pulse irradiation is roughly half of the band gap energy $\langle E_{\mathrm{e}} \rangle \approx 1/2\, E_{\mathrm{e}}^{min} = 1/2\, E_{\mathrm{gap}}$.

We should mention that, in cases with a high density of free electrons, the mean kinetic energy of electrons increases due to Pauli's principle. $\langle E_{\mathrm{e}} \rangle$ may then be larger than half of the minimum energy for secondary ionisations, which leads to a larger effective energy gap. Cases such as this are presented below.

One must also remember that the transient mean kinetic energy of electrons is a function of time. It changes during the laser pulse irradiation, then approaches the value of $\sim 1/2 E_{\mathrm{gap}}$ by the end of the laser pulse and stays almost constant for some time until the energy loss to the lattice via electron-phonon coupling becomes essential (typically, in timescales of 0.1 - 1 ps). Additionally, as mentioned above, further electron-hole recombination will change the number of free electrons and their mean kinetic energy in the picosecond timescale.

The same argument holds for the average energy of holes, which have their own minimum energy for secondary electron creation via an Auger-like process $|E_{\mathrm{h}}^{min}| = 3$ eV, as seen in the analysis of the static band structure discussed in the Model section. Therefore, after losing energy due to an Auger-like process, holes will end up with an energy between the minimal energy $|E_{\mathrm{h}}^{min}|$ and E_{gap}, i.e., $\langle E_{\mathrm{h}} \rangle \approx 1/2(|E_{\mathrm{h}}^{min}| - E_{\mathrm{gap}})$ at the end of the laser pulse, which again is confirmed by averaging over the distribution of holes presented in figure 5.4.

With these considerations, the effective energy gap can be estimated as follows:

$$E_{\mathrm{EEG}} = \frac{1}{2} \cdot (E_{\mathrm{gap}} + E_{\mathrm{e}}^{min} + |E_{\mathrm{h}}^{min}|) \qquad (5.2)$$

where $E_{\mathrm{gap}} = 1.12$ eV, $E_{\mathrm{e}}^{min} = E_{\mathrm{gap}}$ and $|E_{\mathrm{h}}^{min}| = 3$ eV for silicon, the mean energies of electrons and holes, respectively, after all electrons and holes have made all possible secondary ionisations.

The minimum energies E_{e}^{min} and E_{h}^{min} for (5.2) are obtained by an analysis of the static band structure, as explained in section 5.2.2. The resulting values of the EEG for different materials are shown in Table 5.1. We also show the results for the minimum energies for impact ionisation and Coster-Kronig transitions, respectively, that were obtained from the band structures taken from [123].

Experiments focusing on the pair creation energy (PCE) are usually performed in timescales where electron-hole recombination plays a crucial role (i.e., picoseconds or longer). Therefore, a direct comparison of such experiments with the pure EEG is impossible. However, due to recombination,

Table 5.1: For different materials the band gap energy E_{gap}, the minimal kinetic energy of an electron needed for impact ionisation E_{e}^{min}, the minimal energy of a hole for a Coster-Kronig transition $|E_{\text{h}}^{min}|$, and the predicted EEG calculated with (5.2) are presented in comparison with experimental values of EEG with damped electron-hole recombination [116] and the upper limit obtained in long-time measurements for the pair creation energy (PCE) [118].

	E_{gap}	E_{e}^{min}	$|E_{\text{h}}^{min}|$	EEG	Exp.	PCE
Si	1.15	1.2	3	2.62	2.6†	3.63
SiO$_2$	8.9	13.5	12.5‡	17	18§	18
C	4.65	4.8	10.25	9.85	-	13.1
Ge	0.85	1.55	1.8	2.1	-	2.96

†For a detailed comparison see figure 5.7
‡Note that, for SiO$_2$, the width of the valence band is smaller than the band gap; therefore, holes cannot make a Coster-Kronig transition, and the mean energy of holes, which is half of the valence band width, is presented here and used in (5.1)
§Assumed equal to PCE, see text

the electron density in the conduction band decreases and leads to a higher experimental value of the pair creation energy, which can be assumed to be an upper limit for the EEG. The calculated EEG can be compared with experiments that had suppressed electron-hole recombination; the results for Si can be found in [116] and are shown in figure 5.6. For SiO$_2$, electron-hole recombination is not a process of primary importance [61]; therefore, we can expect good coincidence between the experimental long-time value [118] and our calculation. For the two other materials shown in Table 5.1, we can only compare our results for the pure EEG with the upper limit of the pair creation energy for longer times (PCE) [118]. New experiments with femtosecond lasers (FLASH) are needed to confirm our predictions.»

5.3.3   Dependence of EEG on fluence

« In figure 5.7, we show a detailed comparison of the calculated effective energy gap of silicon, which depends on photon energy and fluence, with experimental values and earlier models. The figure contains the experimental data obtained by A.J. Tuzzolino in [116] (red circles), several results of different theoretical calculations taken from previous studies: by M. Brigida et al. [131] (violet diamonds), by R.C. Alig [121] (green crosses), by F. Scholze et al. [120] (blue up-looking triangles) and by G.W. Fraser et al. [122] (orange down-looking triangles). The results of the present calculations are shown with lines for different fluences. As can be clearly seen in this figure, all previous models yield values around the commonly assumed electron-hole pair creation energy in Si, 3.63 eV (i.e., the direct band gap, as discussed above), which is the result of long-timescale experiments [117–122]. These values differ from the

experiments with damped recombination [116] by a factor of two or more, while our simulation compares very well with the experimental data (figure 5.7).
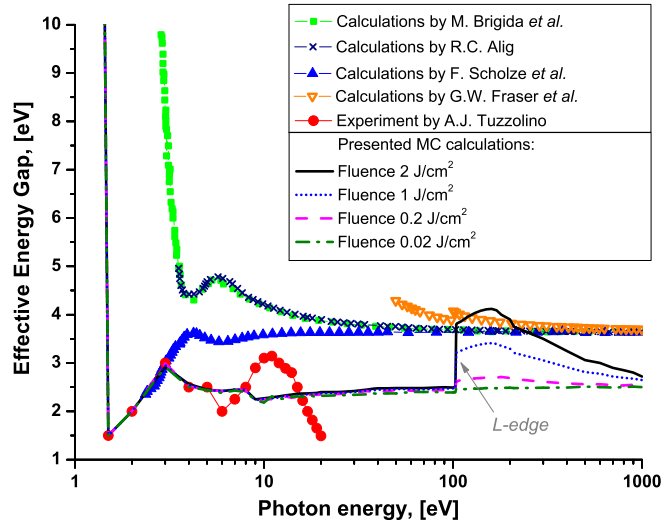
Figure 5.7: Effective energy gap vs. photon energy. Our Monte-Carlo simulation (shown as lines for different fluences) compares well with experimental results extracted from [116] (shown as circles). Other calculations (the diamonds are results of the model from [131], the crosses are the results of the calculations from [121], the up-looking triangles are the results of the simulations presented in [120], and the down-looking triangles are taken from the simulation reported in [122]) show strong deviations.

We found almost no influence of the laser intensity on the EEG in the case of photon energies of several tens of eV. The effective energy gap remains at $E_{EEG} \sim 2.6$ eV in the VUV photon energy region for fluences ranging three orders of magnitude around our chosen fluence, from 0.02 to 20 mJ/cm^2.

However, for higher energies around the $L-$shell edge of Si, the number of absorbed photons is very high in comparison to lower energies. The Auger decay of holes in the $L-$shell has characteristic times typically around 10 fs (for light elements [89]); therefore, $L-$shell photoionisation leads to only a short delay of high energy electron production, which occurs in two steps. First, the photon is absorbed by the $L-$shell, leaving a hole behind. This hole is then filled by an electron from the valence band, which excites a second electron from the valence band into the conduction band or the continuum at a high energy equal to the difference between the $L-$shell ionisation potential and the energy of the electron in the valence band. However, another effect

plays a much bigger role here. As can be seen in figure 5.2, the probability of photoabsorption by $L-$shell electrons is almost two orders of magnitude higher than the photoabsorption by valence electrons. This fact is reflected in a sudden jump in the attenuation length as soon as the photon energy reaches the L-edge. Additionally, highly energetic electrons created after $L-$shell Auger decays then produce impact ionisations of secondary electrons. Finally, the electron density becomes so high that, even for a fluence of 2 J/cm^2, Pauli's principle has to be taken into account. For high densities of excited electrons, the electron loses a large portion of its energy after a few impact ionisations and ends up in low energy states. According to Pauli's principle, electrons fill the lower states of the conduction band, and later generations of electrons cannot also be in the lowest energy states. As a result, the mean electronic energy increases and, according to (5.1), the EEG increases. Thus, for very high electron densities [1], the effective energy gap will deviate, demonstrating the limits of the validity of (5.2).»

5.4 Summary

« In conclusion, the transient dynamics of ionisation and redistribution of free electrons in semiconductors (silicon, in our case) during ultrashort VUV laser pulse irradiation were simulated with a Monte-Carlo method. The method was extended in order to take into account the band structure of the material and Pauli's principle. The number and energy distributions of free electrons as a function of time from zero to 25 femtoseconds (laser pulse duration) were obtained and analysed in detail.

It was demonstrated that the band structure significantly influences the excitation of electrons. An essential part of the total energy provided by the laser pulse was accumulated in holes ($\sim$ 65%). We demonstrated that the total number of excited electrons is determined by a statistical process that depends on the mean kinetic energies of electrons and holes, respectively. The recently introduced effective energy gap [15], a concept accounting for the statistical nature of electron ionisation, is capable of estimating the number of free electrons that are excited in irradiated semiconductors.

A simple formula to estimate this value at femtosecond timescales was proposed based on the analysis of the electronic band structure of the material. The method of such analysis was described, leading to a simple application of the proposed concept. The limits of validity of the concept are discussed while accounting for the timescales, photon energies and fluences of the laser pulse.

---

[1]We must note that, in the regime of such high-electron densities, when Pauli's principle begins to play a role, one of the assumptions of our model is no longer satisfied: the interaction among free electrons becomes non-negligible. However, for the purposes of the present work, the effect of thermalization by the redistribution of energy among free electrons is not important and will not significantly change the outcome of the calculations and the conclusions drawn.

The values of the effective energy gap obtained for different materials compare well with the available experimental data.

The effects of $L-$shell ionisation, as compared to ionisation of the valence band, were considered. It was shown that, in addition to a short delay in high-energy electron production, the $L-$shell ionisation produces another effect: the total number of absorbed photons and, in turn, the total number of excited electrons strongly increases relative to lower photon energies because the photoabsorption sharply increases when photon energy reaches the ionisation potential of the $L-$shell. Pauli's principle comes into play, especially for high fluences, restricting secondary ionisations.

We encourage the creation of experiments with FLASH in the XUV regime around $L-$shell ionisation energies to confirm our predictions and observe the effects discussed in the presented work. Experiments on different materials will also be valuable for comparison.»

This chapter demonstrated that the description of intermediate energy electrons is different from the high energy electron excitations (presented in chapters 3 and 4). The main differences in the MC method are in the inclusion of some of the quantum effects, namely, effects of a band structure of the particular material and the Pauli's exclusion principle. Such effects can not be neglected for electron energies of only a few tens of eV; the proposed extended MC methods takes them into account. Although, the method became more computationally consuming, but it significantly shifted the limit of applicability of Monte-Carlo method to lower energies.

In the next chapter we will demonstrate how further correlation effects between electrons can be accounted for the case of many-electron systems – metals.

Chapter 6

Monte-Carlo simulation of VUV-XUV femtosecond laser pulse irradiation of metals

In this chapter a Monte-Carlo method is modified to describe the kinetics of electronic excitation in a metal irradiated with a femtosecond laser pulse. As discussed in the previous chapter, the method is extended by taking into account the density of states of materials, Pauli's principle, Auger processes. Additionally, for a metal we include free-free electron interactions and correlations between them.

We will focus on calculations of the free electron distribution functions for a 10 to 40 fs Gaussian laser pulses in solid aluminum. Laser and target parameters are chosen according to experiments made with FLASH at DESY in Hamburg, which will allow us to directly compare the calculated results with experimental ones. The comparison with the results of irradiated aluminum is presented for the same parameters of irradiation as in Chapter 5. We also show the comparison of the calculated emission spectra with the experiments. This chapter is partly based on the work [132], the corresponding parts are quoted.

6.1   Monte Carlo method extended for metals

« In our model we consider the following electronic processes: photoabsorption by bound or free electrons, impact ionization by free electrons, Auger-like processes within valence band for semiconductors (so called Coster-Kronig transitions, or impact ionization by holes), and scattering between free electrons within conduction band for metals. These processes give initial conditions for further energy dissipation and an eventual atomic motion. We neglect electron-hole recombinations and radiative decays of holes because they typically need more times than the timescales we are interested in [81, 82].

For the case of metals, free-free electron scattering is considered, taking into account dynamical screening of the interaction potential. For the case of semiconductors, free-bound electron collisions (impact ionizations) are dominant and interaction among free electrons can be fairly neglected [15, 49, 58, 60].»

The temporal intensity distribution of the laser pulse equates a Gaussian shape with the FWHM duration of $\tau_L = 10$ fs and a total duration numerically cut at 25 fs. The photon energy is chosen to be from $\hbar\omega = 38$ eV to 200 eV, and the fluence ranges into interval from 0.2 till 5 J/cm^2, similar to experiments [19, 20]. «Interactions of every single photon with electrons were simulated event by event. The interaction probability with every single electron from different energy states within the valence (for semiconductor) or conduction band (for metal) is determined from the relative cross-section of interaction. The differences in the cross-sections of photo-ionization of electrons from different energy levels were introduced only by different densities of electrons in different levels, according to the DOS-function. The valence band was discretized, and each discrete interval in the valence band was normalized to the total number of electrons in a simulation cube, as described below. This yielded the relative values of the electron concentration in different energetic discretization intervals of the valence band. In the same manner we discretized the conduction band. The details of this numerical algorithm may be found in [15, 104]» and in the previous chapters.

Analogously to the case of semiconductors (Chapter 5), the metallic target is also considered as an isotropic and homogeneous atom arrangement. We chose solid aluminum with a density of $n_{at} = 5.4 \times 10^{28}$ m^{-3}.

In the following, we will analyze the parameters of the laser pulse similar to experiment in order to compare the calculated results with experimentally measured ones; also we will present the results for the same laser parameters are applied as for silicon (10 fs duration FWHM, $\hbar\omega = 38$ eV, fluence of 2 J/cm^2). «For energies of tens of electron-volts, the attenuation length of a photon in aluminum [28] is very close to the one for silicon, see Fig. 6.1. Therefore, we have approximately the same number of absorbed photons within a simulation cube of the size $10 \times 10 \times 10$ nm^3. The periodical boundary conditions for the simulation cube are used again. The initial energy distribution of electrons was chosen to be as follows: the conduction band is filled up to a Fermi-energy of aluminum $E_f = 11.2$ eV (initial temperature equals zero), corresponding to the real density of states of aluminum, presented in Fig. 6.2 [123, 133]. The energy scale for the kinetic energy of free electrons starts at the bottom of the conduction band ($E = 0$ eV in Fig. 6.2). All effective masses of the electrons in the solid were assumed to equal the free electron mass. In contrast to semiconductors, there is no valence band in aluminum. This simplifies the model, since it allows us to skip the band diagram analysis for minimal energy necessary for secondary electronic processes.

However, the numerical algorithm should be modified in two ways. First of all, the interaction among free electrons must be taken into account, as it is the
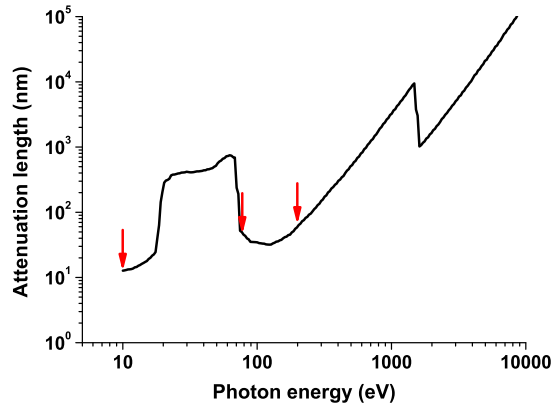
Figure 6.1: Dependence of the photon attenuation length on the photon energy in Al, extracted from [28]. The arrows indicate the photon energies that will be used later in the section 6.4.

only relevant interaction channel on femtosecond timescales for electrons with energy lower than the ionization potential of deep atomic shells ($L-$shell ionization potential of aluminum is ~ 61 eV below the bottom of the conduction band).

Interaction of free electrons can be described well within the Lindhard dielectric function formalism, which takes into account dynamical screening of the interaction potential. Thus, the mean free path (l_e) of the free-free electron scattering and mean energy exchange (dE_e/dx, energy loss per path) can be calculated as follows [49, 61]:

$$l_e^{-1} = n_e \int_0^{E_e - E_f} \frac{d\sigma_e}{d\omega} d\omega \ , \ -\frac{dE_e}{dx} = n_e \int_0^{E_e - E_f} \frac{d\sigma_e}{d\omega} \hbar\omega d\omega \qquad (6.1)$$

Where n_e is the free electron density. The interaction cross-section σ_e is defined via Lindhard dielectric function by the following relation:

$$\frac{d\sigma_e}{d\omega} = \frac{\hbar}{\pi n_e a_0 E_e} \int_{q_1}^{q_2} \frac{1}{q} \Im \left(-\frac{1}{\epsilon(q, \omega)} \right) dq \qquad (6.2)$$

Here we integrate the current momentum within the following limits: from $q_1 = \sqrt{2m_e}/\hbar(\sqrt{E_e} - \sqrt{E_e - \hbar\omega})$ till $q_1 = \sqrt{2m_e}/\hbar(\sqrt{E_e} + \sqrt{E_e - \hbar\omega})$ [49, 61], and $\epsilon(q, \omega)$ is the Lindhard dielectric function [49, 61, 134].» The sign $\Im(x)$ means the imaginary part of x.

« The second modification of the algorithm is necessary to account for correlations between free electrons. The correlations cannot be neglected anymore: after appearance of a "hole" within the conduction band below the Fermi-energy, any free electron can interact with any other to fill this hole. Such a
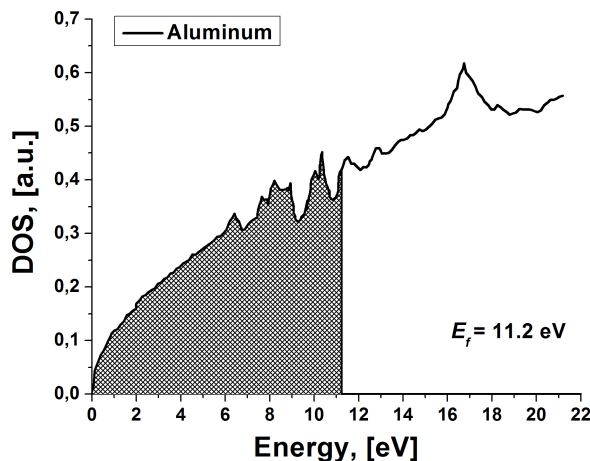
Figure 6.2: The density of states of solid aluminum, extracted from [123, 133]. At the beginning the conduction band is filled up to the Fermi-energy $E_f = 11.2$ eV.

situation occurs when a highly energetic free electron interact with a low energy electron from the bottom of the conduction band (below Fermi-energy). Therefore, the system has to change the state in the sense that all electrons should have a chance to interact with the hole, but not only highly energetic excited electrons. To take into account these correlations, we discretized the timescale into small intervals (small compared to the typical timescale of the problem). On each time-step we redistribute free paths for interaction for all electrons (according to Eqs. 6.1 and 6.2). This gives a chance to interact to those electrons, which do not have high energy but might find a place within low energy states due to ionizations made by other (highly energetic) electrons. Thus, we included possible correlations between electrons in time. Except these points, the same algorithm as the one used for semiconductors can be applied to describe excited metals.»

If the incident photon energy is larger than the ionization potential of the $L-$shell of aluminum, the photons are mostly absorbed via $L-$shell ionizations [28]. Such an absorbtion is accomplished by the excited electron into the conduction band or continuum, leaving an $L-$shell holes behind. This $2p$ holes will then decay via the Auger transitions. For Auger-like processes with $2p$ holes, the exponential law for the time of decay can be applied (chapter 5 and refs . [15, 49]). The DOS and Pauli's principle are taken into account in the same way as for electron impact ionization process. In the algorithm, the electron (hole) enabling the Auger-like transition and the electron being ionized are randomly chosen among the electrons in the conduction band. The

characteristic time of an Auger recombination t_A for L-shell of aluminum is known to be 40 fs [89, 135].

Subsequent dynamics of secondary electrons, produced by the first generation of the free electrons, ionizing $L-$shell if their energy is high enough, and by holes, and their interactions with other electrons or impact ionizations, were also taken into account in the same manner.

Furthermore, we considered one more channel of possible scattering of electrons, an elastic scattering on the target atoms. The mean free path of the scattering is again written in the exponential form. The cross-section of elastic scattering of a free electron with a target atom is taken in the form proposed by Mott with screening parameter by Molière (for details see chapter 3.2.3). If all the prospective path lengths of the traced free electron for inelastic collisions and for free-free electron scattering are larger than those for elastic collisions with atoms, the current collision of the traced free electron is considered as the elastic one. In this case the scattering plane angle φ was specified as random values ranging in the interval $(0, 2\pi]$, and the scattering angle θ is defined by the transferred energy. The transferred energy is unambiguously determined by the differential cross-section and the randomly chosen impact parameter. This transferred energy results in initial lattice excitations, and provides initial conditions for further material modifications.

All applied cross-sections are presented in the Fig. 6.3.
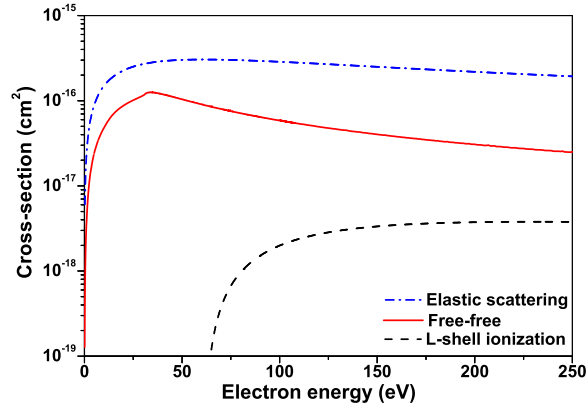
Figure 6.3: Cross-sections of the elastic scattering of electron on atoms (blue dash-dotted line), the electron-electron scattering (solid red line), and the ionization of L-shell (black dashed line) in the relevant energy interval.

The constructed algorithm must be checked for both: a) a correct numerical realization, which is verified by tracing the energy conservation law,

and b) correct physical background of the model, which can be checked by a comparison with experimental data available, see section 6.2.

The energy balance is presented in Fig. 6.4, where the energies of electron, holes, lattice and their sum are presented for the laser parameters, corresponding to the experimental data that will be analyzed below in the next subsection. One can see that the total energy is increasing during the laser pulse. After that, the total energy stays constant, which indicates that the numerical scheme is correct. The total energy is conserved within the computer precision (16 digits), since the MC algorithm traces energy exchange in every single collision event.
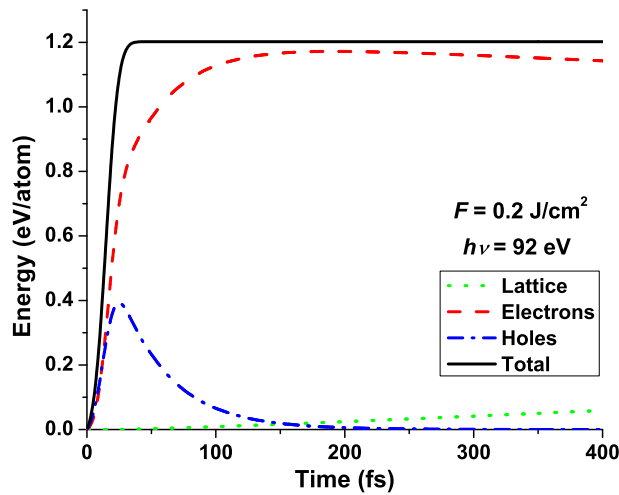
Figure 6.4: Energies of electrons (red dashed line), of L-shell holes (blue dash-dotted line), lattice (green dotted line) and the total energy (sum of them all, black solid line) as functions of time for 92 eV photon energies and fluence 0.2 J/cm^2.

6.2   Comparison to experiments

To check the physical background of the model, we can compare our calculated emission spectra caused by radiative decays of L-shell holes, with the experimentally measured ones. In this case, the laser pulse parameters are chosen to mimic the experimental details from [136]. The temporal intensity envelope of the laser pulse is chosen in the Gaussian shape with a FWHM duration of $\tau_L = 30$ fs. The photon energy is $\hbar\omega = 92$ eV (wavelength of $\lambda = 13.5$ nm)

and the simulated fluences are 0.2 J/cm^2, 0.7 J/cm^2, 1.5 J/cm^2, and 5 J/cm^2. First, we are calculating an electron distribution. The emission spectra are obtained from electron recombinations from the conduction band to $2p$ states. To calculate the emission spectra, we perform the following procedure [137]: we trace the electronic redistribution until all of the L-shell holes are decayed; at the moment of radiative decay of a hole, we save the current distribution of electrons; finally, we average all saved distributions, and get the mean electron distribution. After that, we multiply this averaged distribution with the DOS of aluminum, convolute it with the point-spread-function of the experimentally used spectrometer, and normalize the obtain spectra to directly compare it with experimentally measured ones.

The calculated change of the distribution function of electrons in the conduction band of a solid aluminum irradiated with the fluence of 0.2 J/cm^2 is presented in Fig. 6.5. The electron distribution consists of: the main part of electronic bath, which has only slightly disturbed Fermi-shape [1]; the delta-like peak at approximately 30 eV coming from the electron excitation from the $L-$shell, which is present during and slightly after the laser pulse, and the high energy part of the Auger-electrons at the energies of 73 eV $\pm$ E_F.
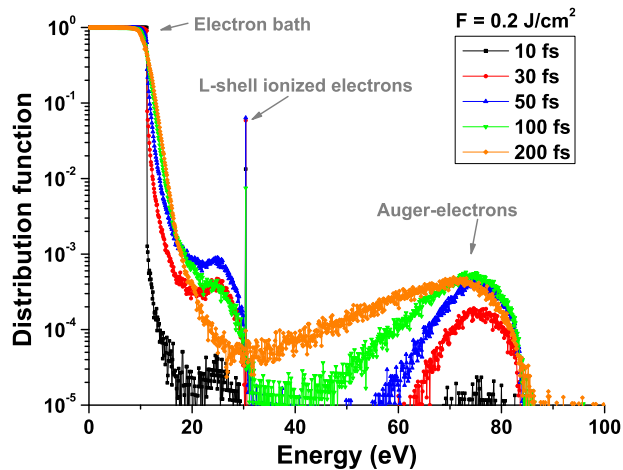
Figure 6.5: Calculated electron distribution function for fluence of 0.2 J/cm^2, photon energy 92 eV, for different time instances.

Figure 6.6 demonstrates the experimental data of emitted spectra together with the calculated ones. The results demonstrate a very good coincidence between them. This allows us to conclude, that the proposed model is indeed

---

[1]Note, that the data between 25 eV and 60 eV are scattered due to numerical statistics, and this scattering has no physical meaning.

appropriate for description of the transient electronic excitation in metals at ultrashort timescales.
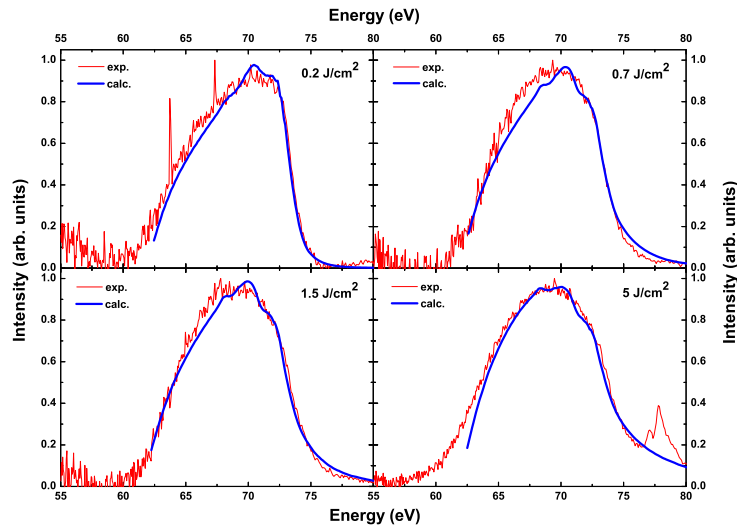
Figure 6.6: Emission spectra from conduction band to $2p$ transition of electrons in irradiated aluminum. The experimental data for fluences of a) 0.2 J/cm^2, b) 0.7 J/cm^2, c) 1.5 J/cm^2, and d) 5 J/cm^2 (thin spiky red lines) are compared with the calculated spectra (bold blue lines).

As can be seen in Fig. 6.5, during the characteristic L-shell decay times, the electronic distribution is not yet thermalized. But the experimental spectra, Fig. 6.6, reflect only one part of electron distribution – electronic bath with energies from the bottom of the conduction band till $\sim 2E_f$. This kind of experimental results do not give an information about the nonequilibrium high-energy tail.

It is also interesting to note, that such a good coincidence is obtained if we use a total DOS of solid aluminum. From the atomic selection rules one might expect that the transition from $3p$ to $2p$ states does not contribute to the observed spectra. However, Fig. 6.7 indicates that the experimental spectra are not well described by the $3s$ and $3d$ electrons emission, but only by *all* of the states together.

Indeed, one can generally expect different selection rules in solids than in single atoms: the electrons in the conduction band of metal aluminum are almost free, in contrast to atomic electrons; furthermore, many-body interactions are essential there, an electron can always find a partner among other

neighboring electrons or phonons to interact with and to satisfy the conservation laws [138].
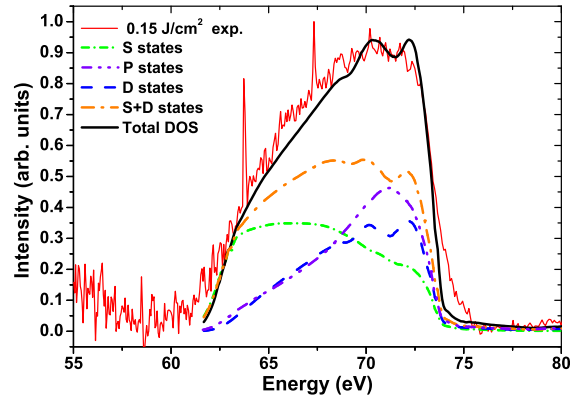
Figure 6.7: Emission spectra for 0.2 J/cm² fluence. Thin spiky line is the experimental data (the same as in Fig. 6.6.a). The calculated spectra obtained from the transitions of all electrons within the conduction band (total DOS) is included as a thick black line, the partial spectra from 3s electrons (3-s states DOS) is presented by the green short-dash-doted line, the violet dash-dot-dot line shows the spectra coming from the 3p electrons (3-p states DOS), the blue dashed line represents the 3d electrons (3-d states DOS), and the orange dash-dot line is 3s + 3d electrons.

A similar consideration of the difference of the selection rules for atoms and solids was presented in the review [139] (and references therein). The authors concluded that the selection rules for electron transitions in solids are the weaker, the more delocalized electronic state is. This perfectly coincides with our observation: the conduction band electrons in aluminum are the most free-like electrons among all the metals, thus, selection rules for transitions from the conduction band to deeper states are expected to have only a small effect if any.

Further we compare the transient distribution functions for different fluences. Fig. 6.8 demonstrates the temporally resolved electron distribution after irradiation of aluminum with 5 J/cm² laser pulse. The other parameters (photon energy, pulse duration) are the same as for Fig.6.5. Now, in contrast to the lower fluence, the distribution looks much smoother at 200 fs, demonstrating a tendency to a faster thermalization. This finding is similar to observations reported in [21] for visible light irradiation: the thermalization of electrons is faster for higher fluences of irradiation.
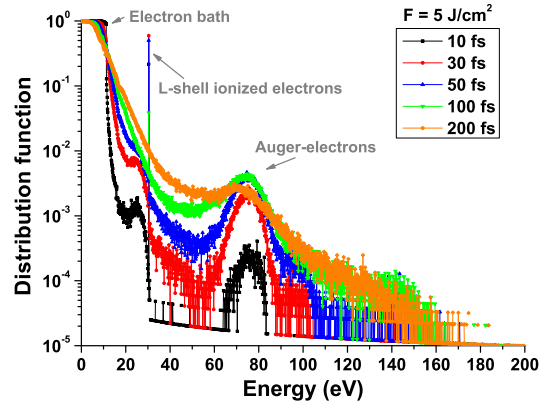
Figure 6.8: Calculated electron distribution function for fluence of 5 J/cm^2, photon energy 92 eV, for different time instances. Compare Fig. 6.5 for lower fluence.

6.3 Difference and similarities with semiconductors

It is also interesting to compare the transient behavior of electron for the case of irradiated metals with semiconductors (Chapter 5). « For a metal, we obtained the transient energy distribution of electrons within the conduction band. Distributions of electrons were again normalized to the number of absorbed photons ($N_{\hbar\omega} = 52$ for the fluence of 2 J/cm^2), and to the aluminum DOS presented in Fig. 6.2. Fig. 6.9 shows the normalized electron distribution function f_e in metal. We see a set of curves similar to Fig. 5.4, but with some differences. The absence of a band gap smoothes the distributions.

The first curve for a time t = 0 fs again corresponds to the absorption of the very first photon. This distribution also reflects the band structure of material, but now electrons are shifted from the conduction band to the higher energies by adding the photon energy $\hbar\omega = 38$ eV. There are the same two competing mechanisms of energy redistribution, however, they act within the conduction band where the density of electrons stays constant. At times shorter than 25 fs the energy increases due to photoabsorption. The bath of Fermi-distributed electrons is also heated by single excited electrons, which redistribute their excess energy among other free electrons (secondary scattering). Therefore, at the end of the laser pulse we see a slightly disturbed Fermi distribution of the main part of electrons and a long high energy tail. The main part of the electrons was not excited by photons and only suffered from the secondary interactions with ionized electrons. The spikes on the curves again reproduce the band structure features during the irradiation.
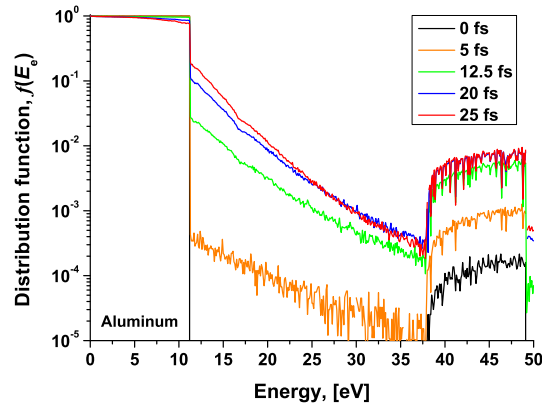
Figure 6.9: Transient electronic distribution function in Aluminum irradiated with a 10 fs FWHM laser pulse.

Except for the features of the distribution attributed to the band structure, the distribution demonstrates also the influence of dynamical screening and collective effects. The screened potential gives smaller cross-sections than the cross-section of impact ionization, thus electrons need more time to redistribute their energy. So we see a stronger non-equilibrium tail than for the case of semiconductors.

In comparison to semiconductors, now all the energy provided by photoabsorption is stored as a kinetic energy of electrons. Therefore, assuming the same absorbed energy, the atoms will be able to get more energy in the following electronic heating of the lattice.»

6.4 Heating of lattice depending on incident photon energy

With the Monte Carlo method described above, we have calculated the lattice heating for three different incident photon energies: 10 eV, 75 eV, and 200 eV. The main difference introduced by the chosen photon energy is that for the photon energy of 10 eV, the photons are absorbed only by the conduction band electrons, without $L-$shell ionizations. Thus, all the energy provided by the laser pulse is kept in the electronic subsystem, and can be exchanged with the lattice. For the case of 75 eV photons, the absorbtion by $L-$shell is dominant. After the photoexcitation, an electron gains the energy of 13 eV above the bottom of the conduction band, which is only a $(\sim (13\text{eV}-E_F)) \sim 3$ eV above the Fermi edge. In this case, the energy from the laser pulse is mainly stored
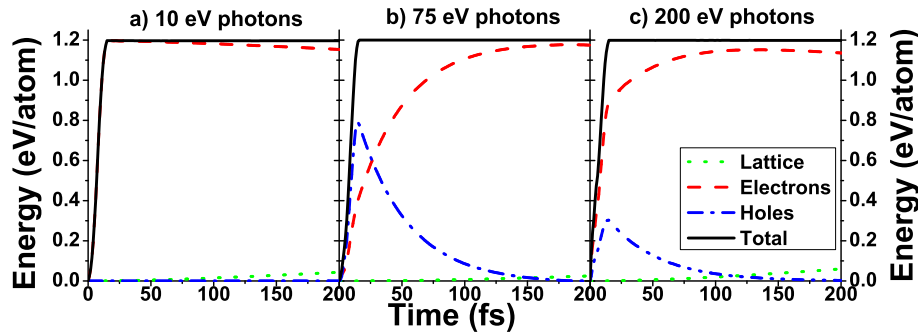
Figure 6.10: Time evolution of the energies of electron, L-shell holes and the lattice after (a) 10 eV, (b) 75 eV, and (c) 200 eV photon energy laser pulse irradiation.

in $L-$shell holes until their Auger-decays with a characteristic time of 40 femtoseconds. As it could be seen above, Fig.6.4, during approximately first 200 fs the electronic subsystem gains the absorbed energy with this delay. Ultrafast processes of a lattice heating can be expected to be different from the first case. And at last, for the energy of 200 eV photon irradiation, the absorption is also mainly by $L-$shell electrons. However, after the photoexcitation, an electron has enough energy to perform the secondary impact ionization of the $L-$shell. Thus, we can expect some interplay of the ionization-Auger recombination mechanisms.

These effects support the idea that the ultrafast heating of the lattice should depend on the incident photon energy. To analyze possible effects, we have performed the simulations, with the total intensity of the laser pulse normalized that way, so that final absorbed energy is 1.2 eV/atom. We applied the laser pulse duration of 10 fs FWHM with a maximum at 10 fs.

As we already could see above, Fig.6.5, electron distribution in irradiated aluminum have two branches: the main part which is almost thermalized, and the nonthermalized tail. The total thermalization is expected to take longer times, but by the time of ~ 200 fs the distribution function of the main part of electrons has a pretty much Fermi-like shape.

The total energies of the free electrons in the CB, the transient energy storage in L-shell holes and the energy transferred to the lattice are shown in the figures 6.10.

In Fig.6.10 one can see that for the 10 eV photons, the photon energy is not enough for L-shell ionizations, and thus all the energy is absorbed by the CB electrons. Then this electrons exchange the energy with the atoms of lattice. In contrast, for the 75 eV photons, the L-shell photoabsorption is dominant, and a big amount of energy provided by the laser pulse is initially stored in the L-shell holes. Later, this energy is released back to the electrons via Auger-decays. This processes cause a delay into the heating of the electronic subsystem of the

metal. In turn, this cause a delay in the heating of lattice. Indeed, the lattice energy is smaller for the case of 75 eV photons than for 10 eV. Furthermore, this effect is even more pronounced, since after the photoabsorption of 10 eV by CB electrons, the electrons end up with the energies within the interval of $[E_f, E_f+10$ eV$]$, while for the 75 eV photons, after the photoabsorption by L-shell electron, they are at the energy only of $E_f + 3$ eV.

For the case of 200 eV photon absorption, the situation is in principle not different from the 75 eV photons: the absorption is occurring dominantly by L-shell photoionizations. Now after the photoabsorption electrons have an energy of ~ 138 eV. This highly energetic electrons heat the lattice faster. Although, some energy is stored also in L-shell holes, but due to the fast heating rate by the other electrons, the final lattice energy is the highest among our investigated photon energies. However, we have to note, that here the energy exchange between electrons and atoms is treated in the simplified manner (accounting only for the total cross-section of elastic scattering as described above). For detailed simulations, it is important to take into account a proper energy exchange mechanism, based on the differential cross-section of scattering as a function of the transferred energy. This does not affect electronic energy losses significantly, but it is important for the resulting energy provided to the lattice.

The energy of L-shell holes is given by the number of L-shell holes multiplied with the ionization potential of the L-shell. Thus, the Fig. 6.10 also shows how fast Auger-processes fill the holes. As one can see, by the time of ~ 200 fs there is no more hole remaining.

When all holes are decayed and the distribution of electrons is close to a thermalized one, following the idea of chapter 4, we can switch to the TTM model describing further lattice heating by equilibrated electronic ensemble. Also, instead of describing the lattice properties in terms of temperature, one can use a Molecular Dynamic simulations (MD-TTM combination [7, 140]), which allows direct investigations of the material modifications.

Due to the different lattice heating rates discussed above, the initial conditions for the MD-TTM are different for different photon energies. Fig. 6.11 shows the comparison of the transient electron energies and excess energy of lattice for different photon energies. One can see a substantial difference at 200 fs.

Since the total absorbed energy is the same, one can expect a similar final lattice heating and, if the energy is enough, probably similar final lattice structural modifications. However, they should occur at different times, since initial heating of the lattice take place with different rates.
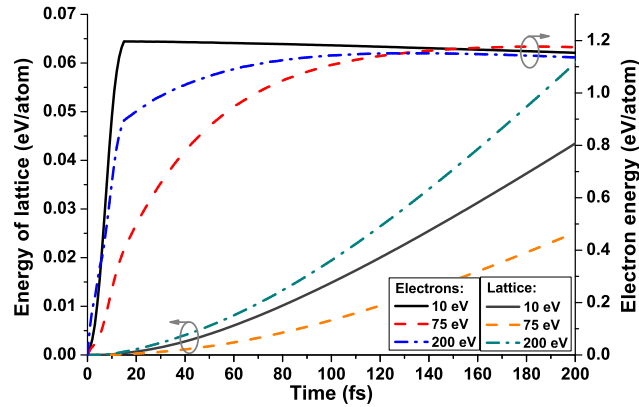
Figure 6.11: Energies of electronic subsystem (right axis) and the energy of lattice (left axis) for the 10 eV, 75 eV, 200 eV photon energies of the 10 fs laser pulse.

6.5 Summary

In conclusion, the transient dynamics of the ionization and redistribution of free electrons in metals (aluminum) during ultrashort VUV-XUV laser pulse irradiation were simulated with a Monte-Carlo method. The method was extended to take into account the band structure of the material, the Pauli's principle, Auger recombinations occurring with holes in the $L-$shell of solid aluminum, and the dynamical screening effects taking place in interactions among free electrons within the conduction band of a metal. It is shown that the non-equilibrium situation is apparently stronger for metals than for semiconductors, due to effective weakening of the interaction among electrons by screening effects. The distribution consists of two parts: the low energetic slightly distorted Fermi-distribution, and the long non-thermalized tail of highly excited electrons. Due to the absence of the valence band, all the energy provided by absorbed incoming photons is stored as kinetic energy of the electrons.

The calculated spectra for different irradiation fluences are in good agreement with the measured ones. Also, the experimentally obtained emission spectra from $2p$ holes decays show that all of the electrons from the conduction band are participating in radiative decays. This demonstrates that the atomic selection rules do not hold for the conduction band electrons of a metal aluminum. During the characteristic decay times, the electronic distribution is not yet thermalized. The experimental spectra reflect only one part of electron distribution, but do not give an information about the nonequilibrium high-energy tail.

For electrons irradiated with femtosecond VUV-XUV laser pulse, we ob-

served a tendency to thermalize faster, when the irradiation fluence is higher. This finding is similar to previously reported results for the visible light irradiation of aluminum.

We demonstrated that the lattice heating on ultrashort timescales by the electrons depends on the incident photon energy. The major role here is played by the ionization of deeper shells ($L-$shell of aluminum for the present analysis). We propose the MC-MD-TTM combination, a model which accounts for the nonequilibrium electron dynamics at ultrashort timescales by MC simulations, for the subsequent lattice heating by the thermalized electrons within the two temperature model, and tracing in detail the lattice structural modifications by means of MD simulations.

This chapter concluded our developed and extended Monte-Carlo algorithm. We have demonstrated, how the classical MC algorithm can be constructed for high excitation energies. Then we came to the intermediate energies, and explained how the MC method can be applied there and which processes must be included. We demonstrated the application of the method to different kinds of materials: dielectrics, semiconductors and metals.

The next chapter will complete our story of electron excitations by adding into consideration a case of very low excitation energies of a few eV. There, a new method, not related to Monte-Carlo scheme, will be presented. Keeping the brand, the method is dealing with non-equilibrium electronic subsystems of solids, and it is applicable for ultra-short timescales.

Chapter 7

Ultrashort visible light irradiation of semiconductors

As it was already mentioned, the Monte-Carlo method was originally created for the treatment of classical systems of particles. Thus, the method is working very well for high energy deposition into materials, allowing for the description of high energy electron transport, as it was discussed in the Chapters 3 and 4. Also, the method can be extended into lower electron energies, i.e. for excitation of materials with XUV-VUV laser pulses, as it was described in Capters 5 and 6, where necessary modifications to account for quantum effects (band structure and DOS of materials, Pauli's principle, correlations) had to be made. However, for very low energies, like for the case of irradiation of materials with visible light, the method becomes hardly applicable. For such low energies, one has to use, for instance, Quantum Monte-Carlo methods, Ab-initio calculations, or other statistical models like solution of Boltzmann kinetic equation, Fokker-Plank equation or similar methods.

Within this chapter we discuss the possibilities of description of material excitation by FLP of visible light. We will develop a relatively simple but powerful model for description of electronic behavior in semiconductors under and after irradiation. This chapter follows the Ref. [141].

7.1   Introduction

«The interaction of laser pulses with matter has been of significant interest in fundamental research both, experimental [8, 13, 142–149] and theoretical [5, 7, 14, 15, 21, 22, 25, 26, 102, 150, 151], and for applications like micromachining, medical surgery and nanotechnology [152–155]. Recently developed, ultrafast lasers [13, 19, 20] have contributed to the progress in fundamental research by allowing the direct investigation of the electronic excitation and relaxation processes on the femtosecond timescale. The pulse duration for ultrafast lasers is comparable to the characteristic times of collisional processes

such as electron-electron and electron-lattice collisions.

Lasers can induce phase transitions in semiconductors and change their optical properties [13, 142, 143, 156–162]. The phase transitions are attributed to the heating and melting of the lattice, while the optical changes reflect a purely electronic effect. An accurate description of the laser field excitation must appropriately contain the lattice and electrons behaviors on ultrashort timescales. To describe semiconductors, it is commonly assumed that earlier models developed for metals may be applied with the necessary modifications [163–167]. However, the underlying physics in the laser excitation of metals and semiconductors are essentially different. Metals are characterized by a large number of free carriers that can absorb the incoming radiation and then quickly redistribute the excess energy among themselves. These processes and the resultant lattice heating can be well-described with thermodynamic models, e.g., the two temperature model [25, 26]. In semiconductors irradiated with visible light, the conduction band has to be filled first with free electrons excited from the valence band. These new electrons can absorb photons via inverse bremsstrahlung and create secondary electrons by impact ionizations. They also heat the lattice [117–120, 168–170].

Thermodynamical approaches, which take into account the laser-induced changes of the electron density in the conduction band, are widely applied [7, 25, 26, 163–167]. Sophisticated descriptions take into account dynamic changes in the optical parameters of a material (i.e., refractive index, reflectivity, and coefficients of photoabsorption) that can result from the irradiation with femtosecond laser pulses [164–166].

However, these approaches have strong limitations: it is generally questionable to apply thermodynamic theory on a femtosecond timescale, since the system may not be in thermal equilibrium. Kinetic approaches have shown, for instance, that the electron-lattice energy exchange is influenced by the particular electron energy distribution and may differ after femtosecond laser excitation from the predictions of the thermodynamical approach [14, 21].

There is another problem of the common description of laser-excited semiconductors: the impact ionization is treated within a simple rate equation, which assumes only a dependence on the density of the free electrons (i.e. electrons in the conduction band) while their energy distribution is neglected [164–166]. However, comparisons with the exact solution of the kinetic equation have shown that this approach may drastically overestimate the importance of the impact ionization processes on a femtosecond timescale [14]. A more detailed description for the excitation of the electrons is essential. The recently proposed multiple rate equation (MRE [10]) combines the advantages of the kinetic approach with the simplicity of the rate equation [6, 10, 171]. The MRE traces the free electron energy distribution and its effect on the impact ionization probability. This influences the transient number of free electrons and thus changes the reflection and the free-electron photoabsorption, finally changing the lattice heating and leading to observable material

Table 7.1: The indices used in Fig.7.1 and the Eq.(7.1). The discrete index corresponds to the energy described in the column 'meaning'

index	value	meaning
k	$\lceil \hbar\omega_L/\Delta\varepsilon \rceil$	Photon energy $\hbar\omega_L$
j	$\lceil E_e^{min}/\Delta\varepsilon \rceil$	Minimum impact energy E_e^{min}
$j\prime$	$\lceil E_g/\Delta\varepsilon \rceil$	Energy gap E_g
m	$\lceil \varepsilon_m/\Delta\varepsilon \rceil$	Maximum energy of calculations
$k\prime$	$\lceil (\varepsilon_i + E_g)/2 \rceil$	Energy of electron prior to Auger-decay

damage [172, 173].

The above mentioned difficulties of standard approaches could be overcame by using ab-initio methods, like DFT [150], molecular dynamics [7], kinetic equations [14], or combinations of such methods. However, these approaches are numerically highly demanding and usually not appropriate to directly interpret experimental results. Thus, our main goal is to establish a model as simple as possible, resolving the density and energy dependence of the governing processes on ultrashort timescales.

We present a comprehensive model based on an extended MRE that includes the nonequilibrium heating of the lattice in dependence on the electronic distribution, and dynamic changes in the dielectric function. The combination of these advanced descriptions of electrons and lattice provides a powerful tool for modeling the laser excitation of semiconductors.»

7.2   A statistical model developed

«In our model, we assume the valence band (VB) to be an infinite bath of electrons that can absorb photons from the laser pulse and increase the number of electrons in the conduction band (CB). This approximation holds for low fluences far from the saturation of photoabsorption. In the opposite case, the change in the number of valence band electrons may be included in the model [171]. However, in the present work we limit ourself to fluences around the melting threshold.

The electrons in the conduction band, further denoted as "free electrons", can absorb additional photons and, by that, increase the energy of the free electron subsystem. Electrons with sufficiently high energy for secondary ionization will perform impact ionizations, which result in electron excitation from the valence band. Excitation from the valence to the conduction band is further denoted as "ionization". The energy required for impact ionization, E_e^{min}, depends on the band structure of the particular material. The electron-phonon scattering heats the lattice but acts as a cooling mechanism for the electronic subsystem. These processes occur on the femtosecond timescale.

On the picosecond timescale, the Auger recombination of free electrons (three-body recombination) decreases the density of electrons in the conduction band. The processes are illustrated in Fig.7.1.
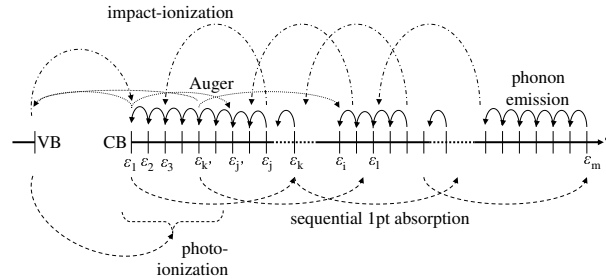
Figure 7.1: A schematic of the processes changing the electronic distribution in the conduction band. The x-axis is the electron energy scale ε divided into the valence band (VB) and the conduction band (CB). The dashed arrows indicate electron energy increase due to photoabsorptions (both, photoexcitation from the VB to the CB, and sequential photoabsorptions within the CB). The dash-dotted arrows show impact ionization processes in which two electrons are involved (excitation of an electron from the VB to the CB by impact of an electron from the CB). The dotted arrows are used to mark Auger-process: one electron falls down from the CB to the VB, while a second electron gains the energy within the CB. The solid arrows between the neighboring energy steps show the process of phonon emission.

In our approach (see Fig.7.1 and cf. Eq. (7.1)), we discretized the energy in the conduction band in steps of the mean *phonon* energy of the material $\Delta\varepsilon = \varepsilon_i - \varepsilon_{i-1}$. The current discrete energy level is marked with index i and ranges from the bottom of the conduction band $\varepsilon_1 = 0$ eV to a certain maximum level ε_m. A list of the additional indices and their meanings is presented in Table 7.1. The photon energy is $\hbar\omega_L$, E_g is the band gap of the material, and the sign $\lceil x \rceil$ means the integer number above x.

For instance, the energy ε_k is equal to the photon energy, counted from the bottom of the conduction band; and the energy ε_{i-k} describes the energy, which is of the one photon energy less than ε_i.»

7.2.1 Extended multiple rate equation describing the electronic distribution

«To describe the electronic subsystem and all of the processes schematically shown in Fig.7.1, we devised the following system of equations for the electronic densities in the conduction band, n_i, at certain energies ε_i based on the multiple rate equation [6, 10]:

$$\dot{n}_i = (\dot{n}_{1p}\theta((\hbar\omega_L - E_g) - \varepsilon_i) + \dot{n}_{2p}\theta((2\hbar\omega_L - E_g) - \varepsilon_i)) +$$
$$\left(W_{i-k}^{1pt}n_{i-k}\theta(\varepsilon_i - \hbar\omega_L) - W_i^{1pt}n_i\right) +$$
$$\left(\frac{n_{i+1}}{\tau_{i+1}^{ph}} \cdot (1 - \delta_{i,m}) - \frac{n_i}{\tau_i^{ph}} \cdot (1 - \delta_{i,1})\right) +$$
$$\left(\sum_{l=j}^{m} \alpha_l n_l \cdot \delta_{i,1} + \alpha_{i+j'}n_{i+j'} - \alpha_i n_i \cdot \theta(\varepsilon_i - E_e^{min})\right) +$$
$$\left(\gamma n_{k'}^2 n_{free} \cdot \theta(\varepsilon_i - E_g) - 2\gamma n_i^2 n_{\text{free}}\right), \text{for } i = 1..m \tag{7.1}$$

where $\theta(x - x_0) = 1$ if $x \geq x_0$, or $\theta(x - x_0) = 0$ otherwise; $\delta_{x,x_0} = 1$ if $x = x_0$, otherwise $\delta_{x,x_0} = 0$.

In the following we describe all terms entering Eq.(7.1).

In contrast to the earlier versions of the MRE [6, 10, 171], as mentioned above, the conduction band is discretized with the energy intervals $\Delta\varepsilon = \varepsilon_i - \varepsilon_{i-1}$ equal to the mean phonon energy of the material.

The change in the electron density n_i with time is denoted with $\dot{n}_i = dn_i/dt$. The first brackets describe the incoming electrons from the valence band by one-photon absorption $\dot{n}_{1p}$. Depending on their initial energy in the valence band, electrons can enter the energy levels from the bottom of the conduction band $\varepsilon_1 = 0$ up to the maximum energy that an electron can receive after photoabsorption, $\hbar\omega_L - E_g$. Electrons after photoabsorption are distributed equally among these levels. The second term in Eq.(7.1) accounts for the two photon absorption $\dot{n}_{2p}$ that can occur for energy levels up to $(2\hbar\omega_L - E_g)$.

The next set of brackets contains the terms for the free-electron photoabsorption, which is described by the probability W_i^{1pt}. The first term here denotes the influx of electrons from lower level k, which is defined in Table 7.1. The second term denotes the loss of electrons at level ε_i due to photoabsorption.

The third set of brackets addresses the energy exchange with phonons that occurs on the characteristic time τ_i^{ph} and depends on the energy of an electron on this level ε_i. Since the discretization interval was chosen to equal the mean phonon energy $\Delta\varepsilon$, the phonon emission will lead to electron jumps between the neighboring levels $i + 1$ and i.

The fourth bracket describes the impact ionization. This process is characterized by the probability of the impact ionization α_k, where the lowest energy

sufficient for impact ionization is defined by the level j (Table 7.1). Due to the impact ionization by any electron from energy levels above a certain limit of E_{e}^{min}, we assumed that the ionized electrons from the valence band end at the lowest energy level ε_1 only. This condition is ensured by the term $\delta_{i,1}$. The high energy electron creating this impact ionization will lose energy equal to the band gap, and the probability of this event is described with $\alpha_{i+j\prime}$.

The last brackets are for the Auger-recombination, which is characterized by the recombination coefficient γ and is generally assumed to be proportional to the cube of the electronic density. For the numerical description, we assumed the following symmetry in the process: both electrons participating in Auger decay are taken from the same level $k\prime$, containing $n_{k\prime}$ electrons, in which one electron jumps to the level i and gains energy, and the other electron falls to the valence band and disappears from the conduction band. However, the electron falling into a valence band can fill any hole, so a third partner in the Auger-process contributes to the equation as the total number of holes, which is equal to the total number of free electrons $n_{\mathrm{free}} = \sum\limits_{i=1}^{m} n_i$. This assumption allows us to describe the influx of electrons to the level i from lower levels with one term $\gamma n_{k\prime}^2 n_{\mathrm{free}}$, where the level of the electron gaining the energy is defined by the index $k\prime$, which can be found in Table 7.1.

The number of the last level m is chosen according to the condition that only a few electrons will reach it during the simulations (no more than $10^{-6} n_{\mathrm{free}}$). This condition ensures that there is no influence of the boundary on the results. One must take special care of the boundary to ensure that no electrons cross it. We have, therefore, additional conditions for the processes in Eq.(7.1) to describe the energy gain for the electrons: the free-electron photoabsorption occurs only for levels below $m - k$, and the Auger recombination is limited to levels $k\prime \leq (m + j\prime)/2$.

The equation (7.1) does not contain spatial dependencies, and, thus, neglects particle and heat transport. Therefore, the model in the present state is valid for the case of thin layer materials under laser irradiation (with a thicknesses smaller than the characteristic attenuation length of photons, which is for the present work $\sim 50\ \mu$m), or on short timescales when the electron transport does not play a significant role (typically, subpicosecond scales [166]). The spatial dependence can be introduced analogously to the method presented in Ref. [171].

The next subsection describes the parameters entering Eq.(7.1). Heating of the lattice due to phonon-emissions by electrons is described in subsection 7.2.3.»

7.2.2 Optical properties and parameters of extended multiple rate equation

«The one-photon absorption rate is defined as:

$$\dot{n}_{1p} = (1 - R)w_b \cdot I(t) \ ,\tag{7.2}$$

where R is the current reflectivity of the material, w_b is the coefficient of the photoabsorption for the particular material and $I(t)$ is the intensity of the laser pulse as a function of time.

The reflectivity is defined via the dielectric function, or the refractive index [163]:

$$R = \frac{(n-1)^2 + k^2}{(n+1)^2 + k^2} \ ,\tag{7.3}$$

with n and k being the real and imaginary parts of the refractive index, respectively. n and k are determined using:

$$2n^2 = \Re(\epsilon) + \sqrt{\Re(\epsilon)^2 + \Im(\epsilon)^2)} \ ,$$
$$2k^2 = -\Re(\epsilon) + \sqrt{\Re(\epsilon)^2 + \Im(\epsilon)^2} \ ,\tag{7.4}$$

where the symbols $\Re$ and $\Im$ denote the real and imaginary part, respectively, and ϵ is the transient dielectric function of the system.

For the dielectric function we use the well-known Drude formula [13, 163, 172, 173]:

$$\epsilon = \epsilon_r - \left(\frac{\omega_p}{\omega_L}\right)^2 \frac{1}{1 + i\nu/\omega_L} \ .\tag{7.5}$$

Here ϵ_r is the intrinsic dielectric constant; $\omega_p = \sqrt{n_{\text{free}}e^2/m_e^*}$ is the transient plasma frequency with e being the electron charge and m_e^* the effective electron mass in the conduction band of the material; ν is the collision frequency parameter. The dielectric function and, thus, the reflectivity depends on the total number of excited electrons in the conduction band n_{free} and, thus, are dynamically changing during the laser pulse irradiation. As we will show below, it is important for determining the material's response to irradiation.

The rate of two-photon absorption $\dot{n}_{2p}$ can be written in a similar manner as the one-photon absorption in Eq.(7.2), with its own coefficient of photoabsorption that can be acquired experimentally for a particular material (see section III).

The free electron photoabsorption can occur only with the help of a third particle that provides the energy- and the momentum-conservations. For solids, this third partner can be either phonon or another free electron [13]. Therefore, the probability of free photoabsorption is written in the form of Drude absorption [174]

$$W_i^{1pt} = \frac{e^2\tau_r}{m_e^*(1 + \omega_L^2\tau_r^2)\hbar\omega_L}E_L^2 \ ,\tag{7.6}$$

where τ_r is the mean electron collision time defined through electron-phonon and electron-electron collision times by Mattissen's rule $\tau_r = (1/\tau_i^{ph} + 1/\tau^e)^{-1}$ [13]. The characteristic time of scattering with phonons depends on the energy of the electron, which is denoted by the index i in τ_i^{ph}. This characteristic scattering time usually is a complicated function for the particular material and is addressed later. The electron-electron collision time τ^e is a function of the number of free electrons: $\tau^e = \langle l_e \rangle / \langle v_e \rangle$, where $\langle l_e \rangle$ is the electron mean free path, and $\langle v_e \rangle$ is the mean electron velocity for all of the free electrons. The mean free path is defined by the electron-electron collision cross-section σ_e and the total electron density $\langle l_e \rangle = 1/(n_{\text{free}} \sigma_e)$. The mean velocity can be easily calculated from the current electron distribution by averaging the energy: $\langle v_e \rangle = (2 \sum_{l=1}^{m} \varepsilon_l n_l / (n_{\text{free}} m_e^*))^{1/2}$. Combining this, we obtain the expression for the mean electron-electron scattering time:

$$\tau^e = \left(\sigma_e n_{\text{free}} \sqrt{2 \sum_{l=1}^{m} \varepsilon_l n_l / n_{\text{free}} / m_e^*} \right)^{-1} . \qquad (7.7)$$

For an estimation of the cross section, one can apply, for instance, the Fermi-screened potential of the interaction. This yields the cross-section in the following form $\sigma_e = \pi r_f^2$, with $r_f = \sqrt{E_f/(6\pi e n_{\text{free}})}$ where the Fermi energy, E_f, can be calculated for the given material density of states and current density of electrons.

E_L is the electrical field amplitude of the laser inside the material and is determined by the laser intensity [14]:

$$E_L^2 = (1-R)I(t)/(\sqrt{\epsilon_0/\mu_0} \sqrt{|\Re(\epsilon)|}) , \qquad (7.8)$$

where the ϵ_0 and μ_0 are the electric constant (vacuum permittivity) and the magnetic constant (vacuum permeability), respectively.

By combining equations (7.6)-(7.8) we obtain the transient coefficient of the free-electron photoabsorption dependent on the material properties and the transient number of excited electrons.

The impact ionization coefficient can be defined by the cross-section of impact ionization: $\alpha_i = n_v \sigma_i v_i$ where n_v is the density of electrons in the valence band of the material; v_i is the velocity of electrons on the level i, which is determined by the energy level $v_i = \sqrt{2\varepsilon_i/m_e^*}$; and the cross section of the impact ionization σ_i can be taken in the analytical form proposed by M. Gryziński [86–88]», Eq. (3.14).

«The coefficient of the Auger-recombination is generally assumed as constant for a particular material (see section 7.3).»
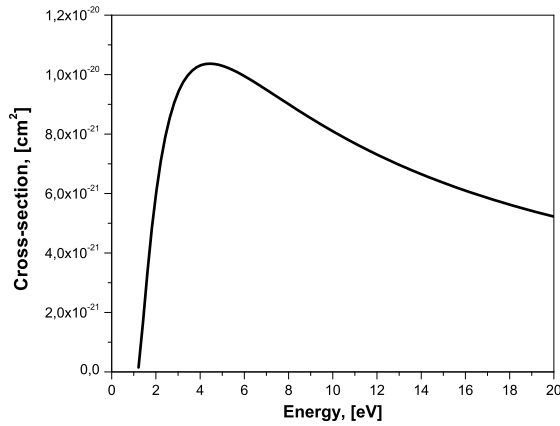
Figure 7.2: Cross-section of impact ionization according to Eq.(3.14) [86–88]. Parameters of a silicon target are applied.

7.2.3 Lattice heating

«At each timestep of the calculations Δt the total energy transferred to the lattice is calculated as $\Delta E_{tot} = \sum_{l=2}^{m} \frac{n_l}{\tau_l^{ph}} \Delta \varepsilon \Delta t$. It is expressed as a lattice temperature as follows:

$$\Delta T_l = \frac{\Delta E_{tot}}{C_l} \quad , \tag{7.9}$$

where ΔT_l is the increase in the lattice temperature and C_l is the lattice heat capacity, which is generally a function of the lattice temperature.

Eq.(7.9) is used to determine the temperature of the lattice heated by the nonequilibrium electronic subsystem, and to evaluate the degree of melting and damage of the material.

When the lattice temperature has reached the melting temperature, additional heat from the electrons is used for melting. During melting, the temperature does not increase, but the electronic subsystem loses its energy to overcome the enthalpy of fusion ΔH.»

7.3 Applied parameters

«Based on earlier experiments [13], we chose a Gaussian laser pulse with a $t_p = 100$ fs duration, determined as a full width of half maximum. The laser pulse intensity is given in the following form:

$$I(t) = F/(s\sqrt{2\pi}) \cdot \exp(-(t - t_p)^2/(2s^2)) \quad , \tag{7.10}$$

where F is the fluence, and $s = t_p/(2\sqrt{2})$ according to the normalization.

The photon energy was $\hbar\omega_L = 1.88$ eV, which corresponds to a wavelength of 625 nm.

Solid silicon was chosen as the target, which has a solid density of $\rho = 2.32$ g/cm^3 and a valence electron density of $n_v = 4 \times 4.5 \ 10^{22}$ 1/cm^3. For a wavelength of 625 nm, the intrinsic dielectric constant is $\epsilon_r = 7.0 + i \times 0.17$ [175].

The coefficient of one photon absorption can be found using Refs. [165, 166]:

$$w_b = (5.02 \cdot 10^3 \text{ cm}^{-1}) \exp(T_l/430 \text{ K})/(\hbar\omega_L) \ . \qquad (7.11)$$

Since the photoionization is generally supported by the electron-phonon interaction, this coefficient depends on the lattice temperature T_l (in K).

The two-photon absorption rate for silicon is defined as follows [165, 166]:

$$\dot{n}_{2p} = \beta((1-R)I(t))^2/(2\hbar\omega_L), \ \beta = 2.0 \text{ cm/GW} \ , \qquad (7.12)$$

However, the two-photon absorption is some orders of magnitude too low to have any significant effect for our range of fluences.

For the free-electron photoabsorption the coefficient of the collisional frequency in the Eq.(7.5) was chosen to be $\nu = 2$ fs^{-1}.

The Auger-recombination coefficient was assumed as $\gamma = 3.8 \times 10^{-31}$ cm^6/s [165, 166].

Additional material properties used are the effective electron mass $m_e^* = 0.35 m_e$, where m_e is the free electron mass, and the mean phonon energy $\Delta\varepsilon = 0.063$ eV [116].

The analysis of the band structure of Si showed that the minimal kinetic energy of an electron in the conduction band necessary for the impact ionization E_e^{min} was equal to the band gap of the material [15, 128]; therefore, the levels j and $j\prime$, mentioned above, are equal.

The band gap of the material is a function of the lattice temperature and is given by the equation [164]:

$$E_g = 1.17 - 1.28 \cdot 10^{-4} T_l - 2.32 \cdot 10^{-7} T_l^2 + 6 \cdot 10^{-11} T_l^3 \qquad (7.13)$$

where the band gap is measured in eV, and the lattice temperature is measured in K. The energy levels $j\prime$ and the conditions depending on the band gap of the material in the Eq.(7.1) will be dynamically changing with the heating of the lattice. Note, that Eq.(7.13) describes a change of the band gap due to lattice heating, but not due to the laser field applied. The ponderomotive shift of the gaps is smaller than $\Delta E_g = e^2 E_L^2/(4 m_e^* \omega_L^2) \approx 0.02$ eV for the applied laser fields strengths [14], which is much smaller than the band gap of Si and, thus, is not included in the model.

The characteristic time of electron-phonon scattering, which is dependent on the electron energy for silicon, was extracted from Fig.7.3 [169, 170] and applied to the system (Eqs. (7.1) and (7.6)).
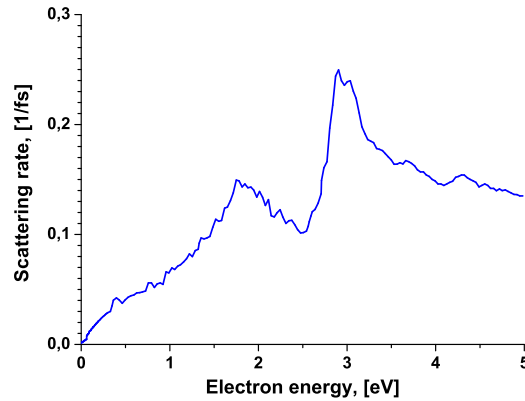
Figure 7.3: The total electron-phonon scattering rate of Si, extracted from the Refs. [169, 170].

For higher energies than shown in Fig. 7.3, we assumed that the rate remained constant and equal to the value corresponding to the maximum energy in the figure.

The heat capacity of the lattice for Si can be found using

$$C_l = 1.978 + 3.54 \cdot 10^{-4} T_l - 3.68 \cdot T_l^{-2} \ , \qquad (7.14)$$

where the heat capacity is measured in $J/(cm^3 \ K)$, and the temperature in K [165, 166].

The melting temperature of solid silicon is $T_{melt} = 1685$ K [13], and the heat of fusion is $\Delta H = 0.0482$ eV/atom.

Taking into account all these parameters, we can solve the system of Eqs.(7.1) and compare the obtained results to experimental data.»

7.4   Results and discussions

«The calculations were performed for different fluences in the range from 0.01 J/cm^2 to 0.4 J/cm^2 to find a critical fluence corresponding to material damage. First, we calculated the dependence of the total free-electron density on time (Fig. 7.4). The electron density in the conduction band increased during and slightly after irradiation and then remained approximately constant. In the range of the characteristic time of the Auger decay, which for the resulting densities of free electrons is around 1 ps, it decreased.

To analyze the excitation and relaxation electronic processes in more detail, we examined the contributions of both channels of electronic ionization,
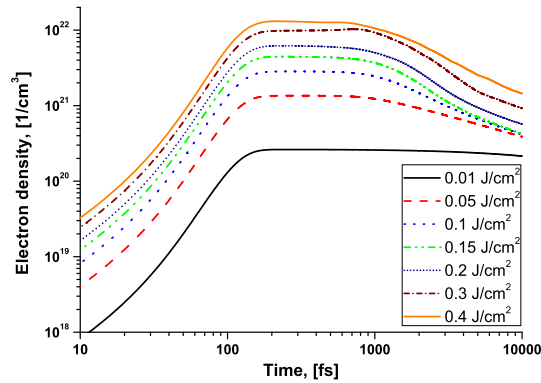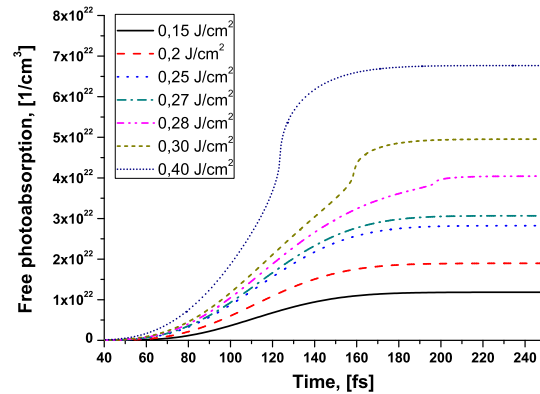
Figure 7.4: The total density of free electrons during and after irradiation of the solid Si target for different fluences of irradiation.

and compared their importance for different fluences. Fig.7.5 shows that the excitation of electrons by photoionization is clearly the dominant process, and impact ionization is involved only for high fluences and long timescales, as is also reported for dielectrics [6, 10]. To perform impact ionization, electrons must gain energy higher than a minimum ionization energy E_{e}^{min}. This energy gain requires time. For femtosecond pulses of visible light, the pulse duration is insufficient to establish the impact ionization channel. Thus, there is no effective ionization avalanche.

The dynamical change in the reflectivity, Eq.(7.3), is presented in Fig.7.6 for different fluences. According to the general dependence of the Drude dielectric function on the electronic density [13,163,165,172], the reflectivity decreases for low fluences, while above some limiting fluence of approximately 0.25 J/cm^2, it starts to increase and overcome the initial value. For high fluences we cut the curves at certain times, when the material melts (see below, Fig. 7.8). During melting of solid silicon, band structure changes leading to collaps of the band gap, thus metallization occurs [13]. Since we do not take into account dynamics of the band structure in the present model, we do not calculate the connected changes of reflectivity.

To compare the obtained reflectivity with experimental data, we plotted its value as a function of fluence for fixed times after irradiation: after 150 fs when the laser pulse is just completed, and at 650 fs (Fig. 7.7). We found perfect agreement between the calculated reflectivity and the experimentally measured reflectivity [13] for the time of 150 fs.

For the time of 650 fs we obtained qualitatively good agreement that reproduced the main features of the increase, while the absolute value of the calcu-
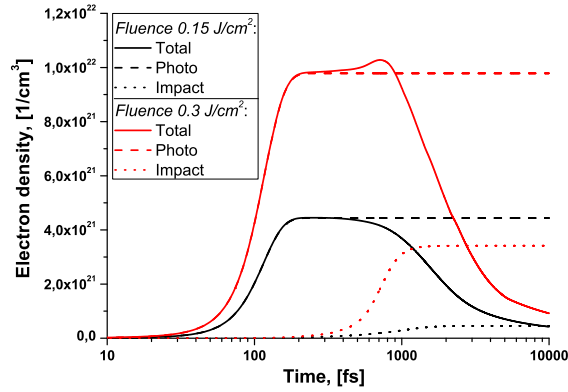
Figure 7.5: Density of free electrons during and after the irradiation of solid Si target caused by different ionization mechanisms. Two different fluences of irradiation are considered.
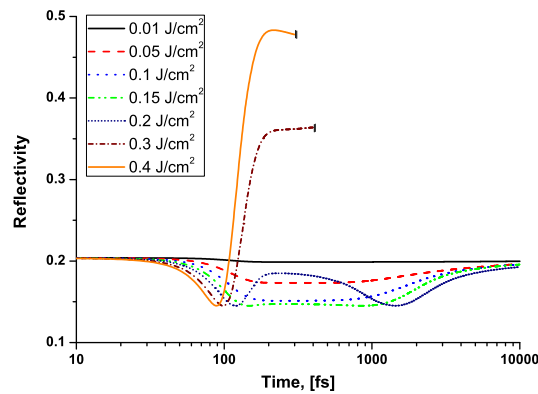
Figure 7.6: The change in the reflectivity as a function of time for different fluences. Curves are shown up to the melting of the material.

lated reflectivity was lower than the experimental one. This may be explained by the fact that at the time of 650 fs for fluences starting from approximately 0.2 J/cm^2, the lattice has already started to melt, as shown below in Fig. 7.8. As mentioned above, the melting of solid silicon leads to a metallization of silicon [13]. Thus, we do not expect a quantitative agreement of reflectivity for

such high fluences. However, the qualitative behavior is still reproduced well as can be seen in Fig. 7.7.
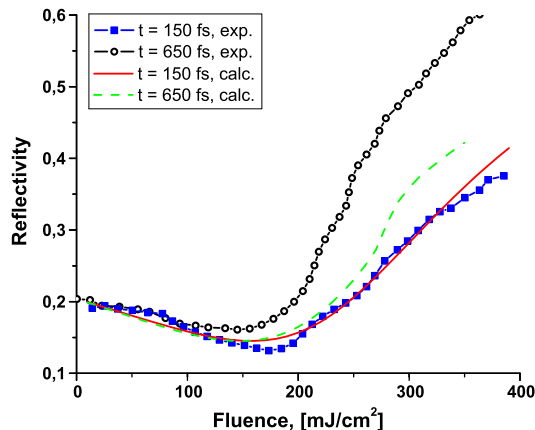
Figure 7.7: The reflectivity as a function of fluence for two different times after the irradiation. The squares and circles are experimental data from Ref. [13]. The lines are the results of the presented calculations.

The heating of the lattice is presented in Fig. 7.8 for different fluences. Here, we found the critical fluence for melting by the direct comparison of the lattice temperature to the melting temperature. Fig. 7.8 shows that the lattice is molten for fluences above approximately 0.141 J/cm^2.

We calculated the critical fluence for melting for two different wavelengths 625 nm and 800 nm. The data are presented in Table 7.2 with the experimental data of the damage threshold from different authors. Our results fit well to the experimental data, although the latter vary rather widely. The general tendency is a larger threshold for the longer wavelength as also found in our calculations.

Based on the results presented in Figs. 7.7 and 7.8 and Table 7.2, we conclude that the proposed model accurately describes both the electronic kinetics and the lattice heating, allowing us to determine the change in the optical parameters and the material damage threshold. The well-established concept of *nonthermal* melting of semiconductors irradiated with femtosecond laser pulses is based on lattice atoms disorder due to a change of the interatomic potential caused of a high ionization degree [13, 150, 166, 167]. In contrast, we obtained the damage fluence via *thermal* melting criteria, i.e. melting of the lattice by heating of atoms in the unchanged interatomic potential. We achieved that because we included two key effects: 1) the dynamic change
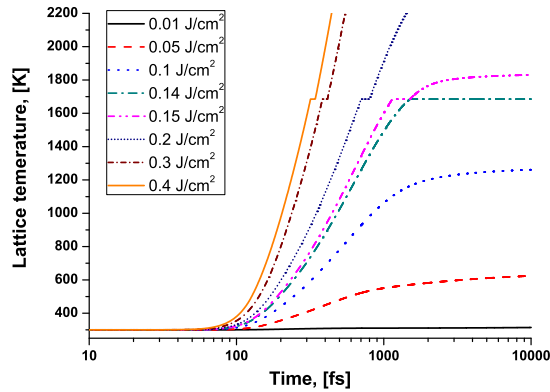
Figure 7.8: The lattice temperature during and after the irradiation of silicon for different fluences of irradiation.

in the optical parameters (reflectivity, free-electron photoabsorption) and 2) the nonequilibrium electron distribution and heating of the lattice with this nonequilibrium electronic ensemble.

Note, that for sufficiently high fluences we obtained a temperature increase greater than 1.5 times the melting temperature within less than one picosecond after the beginning of irradiation. This leads to a fast completion of melting kinetics on the same timescale throughout homogeneous nucleation [7, 102]. Thus, our results show that thermal melting may also occur on a subpicosecond timescale.

Additionally, we performed the analysis of the absorption by free electrons. Fig. 7.9 shows the photoabsorption by free electrons in the conduction band for different fluences. At a fluence of approximately 0.28 J/cm^2, there is a sudden increase in absorption at the end of irradiation. For insulators, this effect is referred to as optical breakdown. In contrast to dielectrics in which the material damage occurs after optical breakdown [172, 173], the material damage (melting) for semiconductors occurs at lower fluences than the optical breakdown (compare thresholds of the data in Fig. 7.8 to those in Fig. 7.9). We conclude that the crystal damage originating from melting and the optical breakdown as a sudden increase in the free-electron photoabsorption are independent processes and must be considered separately, depending on the material and laser parameters.

It is also interesting to note, that the experimental findings shown in Table 7.2 demonstrate two aspects of the data: one set of thresholds at $F_m \sim (0.15 - 0.17)$ J/cm^2, and a second one at 0.25 - 0.27 J/cm^2. While the first set of data corresponds to our calculated melting threshold, the larger values agree with

Table 7.2: A comparison of the calculated and experimentally measured damage threshold fluence F_m [J/cm^2] of silicon for two different irradiation wavelengths (λ, nm). The experimental data were collected from the references cited within the table.

$F_m(\lambda = 625)$	$F_m(\lambda = 800)$	Reference
0.12	-	[156]
0.15	-	[18, 158]
0.17	-	[13]
-	0.15	[161]
-	0.16	[162]
-	0.17	[159]
-	0.25	[142, 160]
-	0.27	[143]
0.141	0.17	Present work

Figure 7.9: The total density of absorbed photons by free electrons during the irradiation of a solid Si target for different fluences of irradiation with visible light of 625 nm.

our calculated optical breakdown threshold. The optical breakdown generally leads to strong irreversible damage of the crystal with possible ablation, thus the damage should be more pronounced in experiments.»

7.5 Summary

«In conclusion, a new model describing the irradiation of semiconductors with femtosecond laser pulses was developed. Based on the earlier proposed multiple

rate equation, the new model includes not only the energy distribution of conduction band electrons, but also the interaction of electrons with phonons and, thereby, the heating of the lattice. Taking into account dynamic changes in the optical parameters of the target (reflectivity, absorption coefficients) and tracing the resulting lattice heating and melting, the model comprehensively gives access to a damage criterion.

In contrast to well-established approaches based on a thermodynamic description of the material, our new model is applicable to nonequilibrium electronic systems in which thermodynamic properties like temperature are not well defined. The model remains simple to use in comparison with, for instance, solving the Boltzmann kinetic approach or the Fokker-Planck equation.

We found perfect agreement with the measured reflectivity of silicon irradiated with a femtosecond laser pulse and the damage fluence threshold.

Our results show that the damage of irradiated semiconductors may be caused by purely thermal melting within a picosecond in addition to the common assumption of nonthermal melting.

It was demonstrated that for semiconductors the lattice reaches the melting temperature first, and the optical breakdown appears only for higher fluences. Thus, the melting and optical breakdown of a material are independent processes and should be considered separately, accounting for the particular material and laser pulse properties.»

This chapter concluded the overview of ultrafast electronic excitations in solids. Together with previous chapters, which were describing high (in the keV regime) and intermediate (tens to hundreds eV) energies of electron excitations, we completed the discussion by constructing a model applicable for low energy excitation (few eV) of semiconductors and dielectrics.

Chapter 8

Summary

This dissertation was focused on general aspects of ultrafast electron behavior in solids after high energy deposition. We discussed two possible ways of such energy deposition: by swift heavy ions (SHI) impacts, and by femtosecond laser pulses (FLP) irradiation. In both cases, FLP and SHI irradiation of solids, initially the electronic subsystem is excited to high energies on subpicosecond timescales, and only later the lattice is heated by this ensemble of electrons. Although the processes of initial excitation of electrons for these two cases are different, but one can expect certain similarities for later electron relaxation. This electronic behavior and energy exchange with a lattice define the following material transformations.

Depending on the energy of initial excitation, it is convenient to bring under consideration three main energy regimes, characterized by different processes involved: a) high energy electron excitation, where the electron energy can reach up to few keV to few tens of keV; b) intermediate electron energies on the order of tens to hundreds eV, and c) low energy electrons, which are excited by a visible light of few eV. These three regimes were described in this work, arranged in the text in the same order. For each of these parts an adequate model has been constructed, and the results were compared to experiments.

The first part was focused on the SHI irradiation of insulators, creating electrons with energies up to several tens of keV (chapters 3 and 4). At this energies, the semiclassical Monte-Carlo (MC) approach was presented and the results were compared to experiments. The method presents a "classical" way to construct a MC algorithm, and describes the main advantages of the model. This part is accomplished by presenting the extended approach – a combination of the MC method with the two temperature model (TTM), and discussion of the advantages of this combined MC-TTM method.

In the second part (chapters 5 and 6), we focused on intermediate energies (in the order of ~ 100 eV) of excitation of the electronic subsystem of materials in ultrashort timescales. To give a particular example, we considered excitations of solids with FLP in VUV-XUV photon energy range. There we have developed a new MC code, which describes the excitation and relaxation

processes in terms of single particles. A classical MC approach was extended to account for a density of states (DOS) of material, for Pauli blocking and correlations. Analyzing the results for semiconductors allowed us to introduce a concept of an effective energy gap, which can be used to estimate a number of excited electron per the absorbed photon. For the case of metals, we described the difference from semiconductors, and introduced necessary modifications in the Monte-Carlo procedure. Comparisons with experimental results were presented there as well.

In the third part (chapter 7), an extended multiple rate equation (EMRE) was proposed. This model describes a visible light irradiation of semiconductors or dielectrics, thus, applicable for electrons excited to the energies of only a few eV. The EMRE is a specially constructed numerical model of solving a kinetic equation. It combines the simplicity of rate equation systems, with a availability of tracing the nonequilibrium electronic distribution. Important differences from the usual thermodynamical approaches are discussed there, and the comparison with experiments is presented.

These three different descriptions complete our story of electron excitations and relaxations at ultrashort timescales. Three different models allowed us to cover a broad interval of energies: from an eV to tens of keV. At different energies, there are peculiarities that have to be considered specially. The corresponding necessary considerations were presented in this dissertation.

List of Figures

List of Tables

Appendix A

Monte-Carlo Algorithm and the applied cross-sections

In this Appendix we will give a more detailed description of the Monte-Carlo algorithm applied in the Chapters 5 and 6. Particularly, we describe the cross-sections applied, possible other choices of cross-sections and the influence on the final results of the simulation. Also, at the end we will focus on the novelty of the proposed method, which most important aspect is tracing individual particles simultaneously with tracing of the electron distribution function.

To model a penetrating laser pulse, we determine the time instance when every particular photon penetrates the simulation box, according to the Gaussian profile of the laser pulse intensity. Then, the realized free path is calculated according to the Poisson law; the mean free path (attenuation length) can be found in Ref. [176] for photon energies above 30 eV. We define whether this photon is absorbed or not, according to a condition, whether the realized penetration depth is smaller than the simulation box size or not. The electron that absorbs the photon is chosen randomly among all the electrons. Note that for photons with energy above the L-shell ionization potential, the probability of photoabsorption by electrons of L-shell is much higher than that of the conduction or valence band electrons (the attenuation length is much shorter [176]).

The following algorithm for the determination of the interaction parameters realizing the collision of excited electron was used [15, 104, 114, 132]: first, we determine the type of the next collision, according to the relative cross-section of elastic atomic scattering, secondary ionization if the electron energy is high enough, and free-free electron scattering for the case of a metal. For the case of a semiconductor, the last process can be neglected, since the density of excited free electrons is much smaller than the density of valence electrons; thus free-free electron scattering becomes negligible on femtosecond timescales (before electron thermalization). On the second step, the path length is calculated for the chosen kind of collision according to Eq.(3.11) from Chapter 3, repeated

here for convenience:

$$l_k = -\ln(\gamma_k)l_0^k \ , \tag{A.1}$$

where l_k is the realized free flight distance, γ_k is a random number uniformly distributed in $[0, 1)$, and $l_0^k = (n_k\sigma_k \cdot F)$ is the mean free path, calculated for the particular event according to its cross-section σ_k, and the number of corresponding scattering centers n_k (atoms, or electrons within particular energy interval). The coefficient $F = (1 - f_c(E))$ is responsible to maintain the Pauli's principle [104, 132], and will be discussed below in more detail.

Here, the cross-section can correspond to elastic scattering $\sigma_k = \sigma_{at}$, for this case $n_k = n_{at}$, the density of atoms; or to secondary ionizations $\sigma_k = \sigma_{imp}$, for which $n_k = n_v$ (where n_v is the density of valence electrons); or to a free-free electron scattering $\sigma_k = \sigma_{free}$, where $n_k = n_e$ denotes the density of free electrons.

The elastic scattering cross-section is taken in a form of Mott's cross-section with the screening parameter proposed by Moliere (see [49, 177] and references therein):

$$\frac{d\sigma_{at}}{d\omega} = r_e^2 \frac{Z_\alpha(Z_\alpha + 1)}{(1 - cos(\theta) + 2\eta_c)^2} \frac{1 - \beta^2}{\beta^4} \ , \ \ \sigma_{at} = \pi a_0^2 \frac{Z_\alpha(Z_\alpha + 1)}{\eta_c(\eta_c + 1)} \frac{Ry^2}{E_e^2} \ . \tag{A.2}$$

Here, $\beta = (v/c)^2$ with v being the electron velocity; c is the speed of light in vacuum; ω is defined out of the transferred energy $\Delta E = \hbar\omega$, which determination will be described later; r_e is the classical electron radius; $a_0 = 0.53$ Å is Bohr radius; E_e is the energy of the free electron; $Ry = 13.6$ eV is the Rydberg constant; Z_a is the atomic number of the colliding atom (Si or Al for our case), and η_c is the screening parameter of the atom by its own electrons [49, 177]:

$$\eta_c = 1.7 \times 10^{-5} Z_\alpha^{2/3} \left(\frac{m_e c^2}{2E_e} - 1 \right) \left(1.13 + 3.76 \frac{Z_\alpha^2}{\alpha^2} \frac{m_e c^2}{2E_e} \Big/ \sqrt{1 + \frac{m_e c^2}{E_e}} \right) \ , \tag{A.3}$$

where m_e is the free electron mass, and $\alpha = 1/137$ is the fine structure constant.

Alternatively, one could use other screening parameters, or even introduce different cross-sections, as discussed in Refs. [49, 177]. In particular, one can apply electron-phonon scattering instead of electron-atom elastic scattering, which is more suitable for low electron energies (below 10 eV or 50 eV [49, 61]). Also, one could calculate electron atom scattering beyond the assumption of single atoms, accounting for many-body effects in solids by means of density-functional-theory or other kind of $ab - initio$ calculations.

For the impact ionization cross-section σ_{imp} we used the following equation obtained by M. Gryzinski [86–88]:

$$\frac{\sigma_{imp}}{d\omega} = 4\pi a_0^2 \left(\frac{Ry}{\hbar\omega}\right)^2 \frac{1}{\hbar\omega} \Phi(I_i, E_e) \times$$

$$\left[\frac{\hbar\omega}{I_i} + \frac{3}{4}\left(1 - \frac{\hbar\omega}{E_e}\right)\ln\left(2.7 + \sqrt{\frac{E_e - \hbar\omega}{I_i}}\right)\right]\left(1 - \frac{\hbar\omega}{E_e}\right)^{\frac{I_i}{I_i - \hbar\omega}} \quad ;$$

$$\sigma_{imp} = 4\pi a_0^2 \left(\frac{Ry}{I_i}\right)^2 \frac{I_i}{E_e}\left(\frac{E_e - I_i}{E_e + I_i}\right)^{3/2} \times$$

$$\left[1 + \frac{2}{3}\left(1 - \frac{I_i}{2E_e}\ln\left(2.7 + \sqrt{\frac{E_e}{I_i} - 1}\right)\right)\right] \quad . \tag{A.4}$$

This cross-section depends on I_i - the ionization potential of i-th electron (electron belonging to the discretized energy interval E_i within the valence band or to the deep atomic shell; n_i is the density of electrons in this energy state); and $\Phi(I_i, E_e) = I_i/E_e[E_e/(I_i + E_e)]^{3/2}$.

The cross-sections (A.4) are very convenient in their simple analytical form. Another possible choice of the cross-sections would be, for instance, semi-empirical Lots cross-sections [178–180], which also have a simple form. Alternatively, one could use a more complex Ritchi-dielectric formalism to account for collective effects in solids ([61] and references therein).

For the aluminum target, the free-free electron collisions are accounted for by means of the Lindhard dielectric function formalism [49, 61, 134]. In the framework of this method, the mean free path and the corresponding energy losses can be calculated as:

$$l_e^{-1} = n_e \int_0^{E_e - E_f} \frac{d\sigma_e}{d\omega}d\omega \;\; , \;\; -\frac{dE_e}{dx} = n_e \int_0^{E_e - E_f} \frac{d\sigma_e}{d\omega}\hbar\omega d\omega \;\; , \tag{A.5}$$

where $\hbar\omega$ is the transferred energy, and $\hbar$ is the Plank constant. The interaction cross-section σ_{free} is defined via the Lindhard dielectric function within the first Born approximation as:

$$\frac{d\sigma_{free}}{d\omega} = \frac{\hbar}{\pi n_e a_0 E_e}\int_{q_1}^{q_2} \frac{1}{q}\Im\left(-\frac{1}{\epsilon(q,\omega)}\right) dq \;\; . \tag{A.6}$$

Here integration is going by the current momentum q within the limits from $q_1 = \sqrt{2m_e}/\hbar(\sqrt{E_e} - \sqrt{E_e - \hbar\omega})$ till $q_1 = \sqrt{2m_e}/\hbar(\sqrt{E_e} + \sqrt{E_e - \hbar\omega})$, and $\epsilon(q,\omega)$ is the Lindhard dielectric function [49, 61, 134]. The total cross-section is obtained by the numerical integration of Eq.(A.6) for each electron energy E_e. After we know the realized free path, we can calculate the corresponding time of the next collision.

Apart from the Lindhard dielectric function, one could employ different models: the Mermin dielectric function, or the Full-Conserving-Dielectric-Function (see [181] and references therein). But as it was shown in [181], the Lindhard dielectric function gives a very good agreement with more precise approaches.

We performed a cross-section analysis to check the difference of alternative models for all kinds of cross-sections: elastic, impact ionization, and free-free electron scattering. It appeared to be that the particular shape of the cross-section does not influence significantly the overall electron behavior. The qualitative electron behavior always remained the same, and the quantitative differences were very small. However, it can influence particular fine effects, where small fractions of electron energy result in observable effects (it concerns, for instance, lattice heating and point defect creation).

For the hole decay time, we apply a Poisson distribution of times of decays with a mean time extracted from Ref. [89] for each particular shell of an atom. For deep shell decays, the most probable process of filling a hole is the Auger decay, where a hole is filled by an electron from the conduction or valence band, while another electron from the valence or conduction band gains the excess energy. For the valence band hole decay of Si, we assume Coster-Kronig transitions and apply the characteristic time from Ref. [89].

After we determined the times of photoabsorption for all photons, the free flight times till the next collision for all free electrons, and the times of decay for all holes, we chose the shortest time among them, and let the corresponding particle perform the event. When a photon is absorbed, we consider the photon to disappear from our analysis, giving the energy to an electron, exciting it to the conduction band or continuum.

In the case of hole Auger decay, the hole is filled, and a new hole might appear within the valence band, if the electron filling the hole initially belonged to the valence but not to the conduction band.

For the electron collisions, we determine the transferred energy out of the differential cross-section of scattering [49, 177]. The corresponding energy transfer ΔE is determined by a random number γ uniformly distributed in [0,1) from the condition:

$$\sigma_k \gamma^2 = \int_0^{\Delta E} \frac{d\sigma_k}{dE} dE \ , \tag{A.7}$$

where one has to solve the inverse problem to obtain ΔE for every particular event, and the cross-sections correspond to Eqs.(A.2), (A.4) or (A.6), depending on a kind of the realized collision.

In case of secondary ionization, we consider an electron to be ionized, if the transferred energy ΔE, calculated with Eqs.(A.4) and (A.7) is higher than the ionization potential of the electron I_i [57], and if there are free places available according to the Pauli's exclusion principle, see below. Subsequent propagation of secondary electrons produced by the first generation of the free

electrons and their interactions with the target are taken into account in the same manner.

After the realized event, the particle changes its state: a photon disappears creating a new free electron; a hole moves up or also disappears, exciting an electron; a colliding electron changes its energy, and may change the energy of a second electron in case of inelastic or free-free scattering. Then, the new free paths for the next possible collisions have to be calculated. After that we find the next shortest time of the event, and trace the next particle, performing a process by applying the same algorithm. Thus, we have time-resolved tracing of all particles involved in our simulation box.

Since every change of an electronic state changes also the electron distribution function, we have to take this into account in our simulation. This is important because of two details: first, the Pauli's exclusion principle (the functional F mentioned above) operates with the transient distributions, which are changing in time; second, the correlation effects must be considered for the case of metals [132]: indeed, after appearance of a "hole" within the conduction band below the Fermi-energy, any of the free electrons can interact with any other to fill this hole. Such situation occurs when a highly energetic free electron interacts with a low energy electron from the bottom of conduction band (below the Fermi-energy), or when an electron is removed from the low energy state by photoabsorption or Auger decay. Therefore, the system has to change the state in the sense that all electrons should have a chance to interact with the hole, but not only highly energetic excited electrons. To take into account these correlations, we discretized the time into small intervals of 0.5 fs (which is small comparing to the typical timescale of the problem). On each time-step we redistribute free paths for interaction for all electrons, which were not able to interact before, giving them a chance to interact since they might find a place now within low energy states. Thus, we included possible correlations between electrons in time.

For both of these reasons, we trace simultaneously the single particles, and the distribution function $f_c(E)$ on the discretization grid (the index c denotes the conduction band electrons, while for semiconductors the index v belongs to the valence band). At each collision, when electron escapes from an energy state E_1, the distribution of electrons changes as $f_c(E_1) \rightarrow f_c(E_1) - 1/g(E_1)$, where $g(E_1)$ is the DOS of our target material, which corresponds to a loss of one electron from this energy state. At the same time, for an incoming electron to the energy interval E_2, the distribution function is increasing by one electron: $f_c(E_2) \rightarrow f_c(E_2) + 1/g(E_2)$. In the case of a second electron involved in the collision, the same procedure must be performed for its own energy states.

It is very important that the Pauli's principle forbids transitions for electrons into fully filled states where $f(E_i) = 1$. That is usually accounted for by multiplying every probability of a collision with a Pauli factor $F = (1 - f_c(E))$. In our simulation, we introduced the functional into the mean free path (all

the cross-sections are multiplied with F, see Eq.(A.1) and its description above) [15, 104, 114, 132]. Therefore, during the simulation only excitations into energy discretization intervals containing still free places at this time instance, according to the DOS and the distribution function, were considered as possible ones. In the case when there is no free place for electrons ($f_c(E_i) = 1$), the free path of such collision l_k calculated by Eq.(A.1) becomes infinite, this event becomes impossible and never realizes. Depending on the transient distribution function for each possible collision, the cross-section, and thus the mean free path, can significantly differ from the original values without Pauli's principle. Exactly this feature is responsible for fulfilling the Pauli's principle; it allowed us to obtain the Fermi-distribution of electrons, instead of the classical Maxwell-Boltzmann distribution [132].

Also note, that if two electrons are involved in the interaction (impact ionization or free-free scattering), there must be two Pauli's factors, each responsible for the probability of available place in the respective final state for both electrons.

Bibliography

[1] S. Amoruso, G. Ausanio, R. Bruzzese, M. Vitiello, and X. Wang. Femtosecond laser pulse irradiation of solid targets as a general route to nanoparticle formation in a vacuum. *Phys. Rev. B*, 71:033406–033410, 2005.

[2] H. Dachraoui and W. Husinsky. Thresholds of plasma formation in silicon identified by optimizing the ablation laser pulse form. *Phys. Rev. Lett.*, 97:107601–107605, 2006.

[3] C. H. Crouch, J. E. Carey, J. M. Warrender, M. J. Aziz, E. Mazur, and F. Y. Génin. Comparison of structure and properties of femtosecond and nanosecond laser-structured silicon. *Appl. Phys. Lett.*, 84:1850–1852, 2004.

[4] V. Hommes, M. Miclea, and R. Hergenröder. Silicon surface morphology study after exposure to tailored femtosecond pulses. *Appl. Surf. Sci.*, 252:7449–7460, 2006.

[5] A. A. Manenkov and A. M. Prokhorov. Distruction of transperent solids by laser irradiation. *Usp. Fiz. Nauk [Sov. Phys. Usp.]*, 29:179 [104], 1986.

[6] B. Rethfeld. Free-electron generation in laser-irradiated dielectrics. *Phys. Rev. B*, 73:035101–035107, 2006.

[7] D.S. Ivanov and L.V. Zhigilei. Combined atomistic-continuum modeling of short-pulse laser melting and disintegration of metal films. *Phys. Rev. B*, 68:064114–064136, 2003.

[8] R. Stoian, A. Rosenfeld, D. Ashkenasi, I.V. Hertel, N.M. Bulgakova, and E.E.B. Campbell. Surface charging and impulsive ion ejection during ultrashort pulsed laser ablation. *Phys. Rev. Lett.*, 88:097603–097606, 2002.

[9] A. Vogel, J. Noack, G. Hüttman, and G. Paltauf. Mechanisms of femtosecond laser nano surgery of biological cells and tissues. *Appl. Phys. B*, 81:1015–1047, 2005.

[10] B. Rethfeld. Unified model for the free-electron avalanche in laser-irradiated dielectrics. *Phys. Rev. Lett.*, 92:187401–187404, 2004.

[11] M.E. Povarnitsyn, T.E. Itina, M. Sentis, K.V. Khishchenko, and P.R. Levashov. Material decomposition mechanisms in femtosecond laser interactions with metals. *Phys. Rev. B*, 75:235414–235419, 2007.

[12] K. Sokolowski-Tinten, J. Solis, J. Bialkowski, J. Siegel, C.N. Afonso, and D. von der Linde. Dynamics of ultrafast phase changes in amorphous gesb films. *Phys. Rev. Lett.*, 81:3679–3682, 1998.

[13] K. Sokolowski-Tinten and D. von der Linde. Generation of dense electron-hole plasmas in silicon. *Phys. Rev. B*, 61:2643–2650, 2000.

[14] A. Kaiser, B. Rethfeld, M. Vicanek, and G. Simon. Microscopic processes in dielectrics under irradiation by subpicosecond laser pulses. *Phys. Rev. B*, 61:11437–11450, 2000.

[15] N. Medvedev and B. Rethfeld. Effective energy gap of semiconductors under irradiation with an ultrashort vuv laser pulse. *Europhys. Lett.*, 88:55001–55005, 2009.

[16] B. Nagler *et al.* Turning solid aluminium transparent by intense soft x-ray photoionization. *Nature Physics*, 5:693–696, 2009.

[17] K. Sokolowski-Tinten *et al. High intensity XUV-FEL interaction with solids: first experimental results*, volume 88. Heidelberg: Springer Series in Chemical Physics, 2007.

[18] S.P. Hau-Riege, R.A. London, R.M. Bionta, M.A. McKernan, S.L. Baker, J. Krzywinski, R. Sobierajski, R. Nietubyc, J.B. Pelka, M. Jurek, L. Juha, J. Chalupský, J. Cihelka, V. Hájková, A. Velyhan, J. Krása, and J. Kuba. Multiple pulse thermal damage thresholds of materials for x-ray free electron laser optics investigated with an ultraviolet laser. *Appl. Phys. Lett.*, 90:173128–173130, 2007.

[19] U. Zastrauand C. Fortmann, R.R. Fäustlin, L.F. Cao, T. Doppner, S. Düsterer, S.H. Glenzer, G. Gregori, T. Laarmann, H.J. Lee, A. Przystawik, P. Radcliffe, H. Reinholz, G. Röpke, R. Thiele, J. Tiggesbäumker, N.X. Truong, S. Toleikis, I. Uschmann, A. Wierling, T. Tschentscher, E. Förster, and R. Redmer. Bremsstrahlung and line spectroscopy of warm dense aluminum plasma heated by xuv free-electron-laser radiation. *Phys. Rev. E*, 78:066406–066410, 2008.

[20] J. Chalupsky, L. Juha, J. Kuba, J. Cihelka, V. Hajkova, S. Koptyaev, J. Krasa, M. Bergh, C. Caleman, J. Hajdu, R.M. Bionta, H. Chapman, A. Velyhan, R.A. London, M. Jurek, J. Krzywinski, R. Nietubyc, J.B.

Pelka, S.P. Hau-Riege, R. Sobierajski, J. Meyer ter Vehn, A. Tronnier, K. Sokolowski-Tinten, K. Tiedtke, S. Toleikis, T. Tschentscher, H. Wabnitz, U. Zastrau, and N. Stojanovic. Characteristics of focused soft x-ray free-electron laser beam determined by ablation of organic molecular solids. *Optics Express*, 15:6036–6043, 2007.

[21] B. Rethfeld, A. Kaiser, M. Vicanek, and G. Simon. Ultrafast dynamics of nonequilibrium electrons in metals under femtosecond laser irradiation. *Phys. Rev. B*, 65:214303–214313, 2002.

[22] P. Lorazo, L.J. Lewis, and M. Meunier. Thermodynamic pathways to melting, ablation, and solidification in absorbing solids under pulsed laser irradiation. *Phys. Rev. B*, 73:134108–134129, 2006.

[23] R.I. Tobey, D. Prabhakaran, A.T. Boothroyd, and A. Cavalleri. Ultrafast electronic phase transition in $la_{1/2}sr_{3/2}mno_4$ by coherent vibrational excitation: evidence for nonthermal melting of orbital order. *Phys. Rev. Lett.*, 101:197404–197407, 2008.

[24] A. Couairon, L. Sudrie, M. Franco, B. Prade, and A. Mysyrowicz. Filamentation and damage in fused silica induced by tightly focused femtosecond laser pulses. *Phys. Rev. B*, 71:125435–125445, 2005.

[25] M.I. Kaganov, I.M. Lifshitz, and L.V. Tanatarov. Relaxation between electrons and lattice. *Zh. Eksp. Teor. Fiz. [Sov. Phys. JETP, in english]*, 31[4]:232 [173], 1956 [1957].

[26] S.I. Anisimov, B.L. Kapeliovich, and T.L. Perelman. Electron emission from metal surfaces exposed to ultrashort laser pulses. *Zh. Eksp. Teor. Fiz. [Sov. Phys. JETP, in english]*, 66[39]:776 [375], 1974 [1974].

[27] H.E. Elsayed-Ali, T.B. Norris, M.A. Pessot, and G.A. Mourou. Time-resolved observation of electron-phonon relaxation in copper. *Phys. Rev. Lett.*, 58:1212–1215, 1987.

[28] N.J. Carron. *An Introduction to the Passage of Energetic Particles through Matter.* New York - London: Taylor and Francis Group, 2007.

[29] I.A. Baranov, Yu.V. Martynenko, S.O. Tsepelevich, and Yu. N. Yavlinskiy. Inelastic sputtering of solids by ions. *Usp. Fiz. Nauk [Sov. Phys. Usp]*, 156 [31]:178 [1015], 1988.

[30] A.M. Miterev. Theoretical aspects of the formation and evolution of charged particle tracks. *Usp. Fiz. Nauk [Sov. Phys. Usp]*, 172 [45]:1131 [1019], 2002.

[31] F.F. Komarov. Defect and track formation in solids irradiated by superhigh-energy ions. *Usp. Fiz. Nauk [Sov. Phys. Usp]*, 173 [46]:1287 [1253], 2003.

[32] L.T. Chadderton. Nuclear tracks in solids: registration physics and the compound spike. *Radiat. Meas.*, 36:13–34, 2003.

[33] P. Sigmund. *Stopping of Heavy Ions.* Springer Tracts of Modern Physics Vol. 204, Springer, Berlin, 2004.

[34] See special issue. *Fifth International Symposium on Swift Heavy Ions in Matter (SHIM 2002).* Giardini Maxos, Italy, 2002.

[35] See special issue. *Sixth International Symposium on Swift Heavy Ions in Matter (SHIM 2005).* Giardini Maxos, Italy, 2005.

[36] C. P. Poole and Jr. and F. J. Owens. *Introduction to Nanotechnology.* Wiley Interscience, Hoboken, New Jersey, 2003.

[37] M. Toulemonde, C. Dufour, and E. Paumier. Transient thermal process after a high-energy heavy-ion irradiation of amorphous metals and semiconductors. *Phys. Rev. B*, 46:14362–14369, 1992.

[38] A. E. Volkov and V. A. Borodin. Transient thermal process after a high-energy heavy-ion irradiation of amorphous metals and semiconductors. *Nucl. Instrum. Methods Phys. Res. B*, 146:137–141, 1998.

[39] G. Schiwietz, E. Luderer, and P. L. Grande. Ion tracks – quasi one-dimensional nano-structures. *Appl. Surf. Sci.*, 182:286–292, 2001.

[40] V.P. Efremov, S.A. Pikuz Jr., A.Ya. Faenov, O. Rosmej, I. Yu. Skobelev, A. V. Shutov, D. H.H. Hoffmann, and V. E. Fortov. Study of the energy release region of a heavy-ion flux in nanomaterials by x-ray spectroscopy of multicharged ions. *JETP Lett.*, 81:378–382, 2005.

[41] J. Rzadkiewicz, O. Rosmej, A. Blazevic, V.P. Efremov, A. Gojska, D.H.H. Hoffmann, S. Korostiy, M. Polasik, K. Slabkowska, and A. E. Volkov. Studies of the kÎś x-ray spectra of low-density sio_2 aerogel induced by ca projectiles for different penetration depths. *High Energy Density Phys.*, 3:233–236, 2007.

[42] J. Rzadkiewicz, A. Gojska, O. Rosmej, M. Polasik, and K. Slabkowska. Interpretation of the si $k\alpha$ x-ray spectra accompanying the stopping of swift ca ions in low-density sio_2 aerogel. *Phys. Rev. A*, 82:012703–012717, 2010.

[43] H. Rothard. Electron ejection by heavy particles as precursor of track formation in condensed matter. *Nucl. Instrum. Methods Phys. Res. B*, 22:27–39, 2004.

[44] F. F. Komarov, O. I. Velichko, V. A. Dobrushkin, and A. M. Mironov. Mechanisms of arsenic clustering in silicon. *Phys. Rev. B*, 74:035205–035215, 2006.

[45] K. Schwartz, A.E. Volkov, K.-O. Voss, M.V. Sorokin, C. Trautmann, and R. Neumann. Thermal spike effect on defect evolution in nacl irradiated with light and heavy ions at 8 and 300 k. *Nucl. Instrum. Methods Phys. Res. B*, 245:204–209, 2006.

[46] K. Schwartz, A.E. Volkov, M.V. Sorokin, C. Trautmann, K.-O. Voss, R. Neumann, and M. Lang. Effect of electronic energy loss and irradiation temperature on color-center creation in lif and nacl crystals irradiated with swift heavy ions. *Phys. Rev. B*, 78:024120–024130, 2008.

[47] E. Akcöltekin, S. Akcöltekin, O. Osmani, A. Duvenbeck, H. Lebius, and M. Schleberger. Swift heavy ion irradiation of srtio$_3$ under grazing incidence. *New J. Phys.*, 10:053007– 053020, 2008.

[48] A.M. Kolchuzhkin. *Monte-Carlo method in the theory of radiation transport [in russian]*. Tomsk:TPU, Russia, 2004.

[49] A.F. Akkerman. *Modeling of Charged Particles Trajectories in Matter [in russian]*. Nauka, Moscow, Russia, 1991.

[50] N. N. Bogoliubov and K. P. Gurov. Kinetic equations. *J. Exp. Theor. Phys., [in Russian] (Journal of Physics USSR)*, 17 [10]:614–628 [265–274], 1946 [1946].

[51] L. Boltzmann. *Lectures on Gas Theory*. Berkeley, CA: U. of California Press, 1964.

[52] H. Risken. *The Fokker-Planck Equation: Methods of Solutions and Applications*. Springer Series in Synergetics, Heidelberg, 1996.

[53] J. Gibbs. *Elementary Principles in Statistical Mechanics*. New York: C. Scribner's Sons, 1902.

[54] N. Metropolis and S.M. Ulam. The monte carlo method. *J. Amer. Statist. Assoc.*, 44:335–341, 1949.

[55] G.S. Fishman. *Monte-Carlo Concepts, Algorithms and Applications*. Springer-Verlag, New York, 1996.

[56] R. Meester. *A natural introduction to probability theory*. Birkhaeuser Verlag, Basel, Switzerland, 2003.

[57] N. A. Medvedev, A. E. Volkov, N. S. Shcheblanov, and B. Rethfeld. Early stage of the electron kinetics in swift heavy ion tracks in dielectrics. *Phys. Rev. B*, 82:125425–125436, 2010.

[58] N.A. Medvedev and A.E. Volkov. Monte-carlo simulations of electronic excitations in swift heavy ion tracks in sio_2. *AIP Conf. Proc.*, 999:238 – 244, 2008.

[59] W. Eckstein. *Computer Simulations of Ion-Solid Interactions*. New York: Springer-Verlag, 1991.

[60] B. Gervais and S. Bouffard. Simulation of the primary stage of the interaction of swift heavy ions with condensed matter. *Nucl. Instr. and Meth. B*, 88:355 – 364, 1994.

[61] M. Murat, A. Akkerman, and J. Barak. Total and partial atomic-level widths. *IEEE Trans. Nucl. Sci.*, 55:3046–3054, 2008.

[62] E. J. Kobetich and R. Katz. Energy deposition by electron beams and δ rays. *Phys. Rev.*, 170:391–396, 1968.

[63] M.P.R. Waligórski, R.N. Hamm, and R. Katz. The radial distribution of dose around the path of a heavy ion in liquid water. *Nucl. Tracks Radiat. Meas.*, 11:309–319, 1986.

[64] R. Katz, K.S. Loh, L. Daling, and G.R. Huang. An analytic representation of the radial distribution of dose from energetic heavy ions in water, si, lif, nai, and sio_2. *Radiat. Eff. Defects Solids*, 114:15–20, 1990.

[65] B. Gervais, M. Beuve, G.H. Olivera, and M. E. Galassi. Numerical simulation of multiple ionization and high let effects in liquid water radiolysis. *Radiat. Phys. Chem.*, 75:493–513, 2006.

[66] O. Avila and M. E. Brandan. Low energy ion tracks in lithium fluoride. *Nucl. Instrum. Methods Phys. Res. B*, 218:289–293, 2004.

[67] M. L. Knotek and P. J. Feibelman. Stability of ionically bonded surfaces in ionizing environments. *Surf. Sci.*, 90:78–90, 1979.

[68] C.N.R. Rao and D.D. Sarma. Interatomic auger transitions in transition-metal oxides. *Phys. Rev. B*, 25:2927–2929, 1982.

[69] G.K. Wertheim, J.E. Rowe, D.N.E. Buchanan, and P.H. Citrin. Experimental interatomic auger rates in sodium halides. *Phys. Rev. B*, 51:13669–13674, 1995.

[70] L. Van Hove. Correlations in space and time and born approximation scattering in systems of interacting particles. *Phys. Rev.*, 95:249–262, 1954.

[71] J.A. Bearden and A.F. Burr. Structural, electronic, and effective-mass properties of silicon and zinc-blende group-iii nitride semiconductor compounds. *Rev. of Mod. Phys.*, 39:125–142, 1967.

[72] H.-D. Betz. Charge states and charge-changing cross sections of fast heavy ions penetrating through gaseous and solid media. *Rev. Mod. Phys.*, 44:465–539, 1972.

[73] M. Toulemonde. Irradiation by swift heavy ions: Influence of the non-equilibrium projectile charge state for near surface experiments. *Nucl. Instrum. Methods Phys. Res. B*, 250:263–268, 2006.

[74] K. Shima, T. Ishihara, T. Miyoshi, and T. Mikumo. Equilibrium charge-state distributions of 35 – 146-mev cu ions behind carbon foils. *Phys. Rev. A*, 28:2162–2168, 1983.

[75] G. Schiwietz, K. Czerski, M. Roth, F. Staufenbiel, and P. L. Grande. Femtosecond dynamics – snapshots of the early ion-track evolution. *Nucl. Instrum. Methods Phys. Res. B*, 226:683–704, 2004.

[76] J. P. Rozet, C. Stéphan, and D. Vernhet. Etacha: a program for calculating charge states at ganil energies. *Nucl. Instrum. Methods Phys. Res. B*, 107:67–70, 1996.

[77] L.D. Landau and E.M. Lifshitz. *Course of Theoretical Physics: Mechanics, Vol.1; 3rd ed.* Elsevier Science, Pergamon Press, Oxford, 1976.

[78] A. A. Rukhadze and V. P. Silin. Electrodynamics of media with spatial dispersion. *Usp. Fiz. Nauk [Sov. Phys. Usp.]*, 74 [4]:223 [459], 1961.

[79] A. A. Rukhadze and V. P. Silin. Linear electromagnetic phenomena in a plasma. *Usp. Fiz. Nauk [Sov. Phys. Usp.]*, 76 [5]:79 [37], 1962.

[80] V.P. Silin. *Introduction to the Kinetic Theory of Gases [in russian]*. FIAN-RAS, Moscow, 1998.

[81] R.L. Kauffman, K.A. Jamison, T.J. Gray, and P. Richard. Relative multiple ionization cross sections of neon by projectiles in the 1-2-mev/amu energy range. *Phys. Rev. A*, 11:872–883, 1975.

[82] J.A. Demarest and R.L. Watson. Ion-excited $k\alpha$ x-ray satellite spectra of si, s, cl, and ar in the gas phase. *Phys. Rev. A*, 17:1302–1313, 1978.

[83] C. Schmiedekamp, B.L. Doyle, T.J. Gray, R.K. Gardner, K.A. Jamison, and P. Richard. Linear electromagnetic phenomena in a plasma. *Phys. Rev. A*, 18:1892–1901, 1978.

[84] H. Rothard, G. Lanzanó, E. De Filippo, and C. Volant. Fermi shuttle acceleration in atomic collisions: the case of ion induced electron emission. *Nucl. Instrum. Methods Phys. Res. B*, 230:419–425, 2005.

[85] G. Lanzanó, E. De Filippo, H. Rothard, C. Volant, A. Anzalone, N. Arena, M. Geraci, F. Giustolisi, and A. Pagano. Fast electron production in collisions of swift heavy ions (20 mev/u < e < 100 mev/u) with foils of solids. *Nucl. Instrum. Methods Phys. Res. B*, 233:31–42, 2005.

[86] M. Gryziński. Two-particle collisions. i. general relations for collisions in the laboratory system. *Phys. Rev.*, 138:A305–A321, 1965.

[87] M. Gryziński. Two-particle collisions. ii. coulomb collisions in the laboratory system of coordinates. *Phys. Rev.*, 138:A322–A335, 1965.

[88] M. Gryziński. Classical theory of atomic collisions. i. theory of inelastic collisions. *Phys. Rev.*, 138:A336–A358, 1965.

[89] O. Keski-Rahkonen and M.O. Krause. Total and partial atomic-level widths. *At. Data Nucl. Data Tables*, 14:139–146, 1974.

[90] M. Inokuti. Inelastic collisions of fast charged particles with atoms and molecules – the bethe theory revisited. *Rev. Mod. Phys.*, 43:297–347, 1971.

[91] J.F. Ziegler. Stopping of energetic light ions in elemental matter. *J. Appl. Phys.*, 85:1249–1253, 1999.

[92] G. Schiwietz and P. L. Grande. On the treatment of light-ion electronic stopping in dense matter. *Nucl. Instrum. Methods Phys. Res. B*, 90:10–19, 1994.

[93] V.P. Shevelko, M.S. Litsarev, and H. Tawara. Multiple ionization of fast heavy ions by neutral atoms in the energy deposition model. *J. Phys. B*, 41:115204–115209, 2008.

[94] M. Caron, H. Rothard, M. Toulemonde, B. Gervais, and M. Beuve. Theoretical and experimental study of electronic temperatures in heavy ion tracks from auger electron spectra and thermal spike calculations. *Nucl. Instrum. Methods Phys. Res. B*, 245:36–40, 2006.

[95] M. Biberman and V. S. Vorob'ev and I. T. Yakubov. *Kinetics of the Nonequilibrium Low-Temperature Plasma*. Plenum, New York [Nauka, Moscow, in Russian], 1987 [1982].

[96] D. Jou and J. Casas-Vazquez and G. Lebon. *Extended Irreversible Thermodynamics*. Springer, New York, 2001.

[97] L. Wang and X. Zhou and X. Wei. *Heat Conduction. Mathematical Models and Analytical Solutions*. Springer, New York, 2008.

[98] O. Osmani, N. Medvedev, M. Schleberger, and B. Rethfeld. Excitation and relaxation of swift heavy ion irradiated dielectrics. *e-J. Surf. Sci. Nanotech.*, 8:278–282, 2010.

[99] N. Medvedev, O. Osmani, M. Schleberger, and B. Rethfeld. Track creation after swift heavy ion irradiation of insulators. *Nucl. Instrum. Methods Phys. Res. B*, 268:3160–3162, 2010.

[100] E. Akcöltekin, T. Peters, R. Meyer, A. Duvenbeck, M. Klusmann, I. Monnet, H. Lebius, and M. Schleberger. Creation of multiple nanodots by single ions. *Nat. Nanotechnol.*, 2:290–294, 2007.

[101] E.M. Bringa and R.E. Johnson. Coulomb explosion and thermal spikes. *Phys. Rev. Lett.*, 88:165501–165505, 2002.

[102] B. Rethfeld, K. Sokolowski-Tinten, D. von der Linde, and S. I. Anisimov. Ultrafast thermal melting of laser-excited solids by homogeneous nucleation. *Phys. Rev. B*, 65:21430–21434, 2002.

[103] A.F. Akkerman and Yu.M. Nikitushev and V.A. Botvin. *Monte-Carlo Solutions of Problems of fast Electron Transport in Matter [in russian]*. Nauka, Alma-Ata, 1971.

[104] N. Medvedev and B. Rethfeld. Dynamic of electronic subsystem of semiconductors excited with an ultrashort vuv laser pulse. *Proc. of SPIE*, 7361:13–22, 2009.

[105] J. F. Ziegler and J. P. Biersack. *The stopping and range of ions in matter (SRIM)*. http://www.srim.org/, 2008.

[106] P. G. Klemens. Thermal resistance due to point defects at high temperatures. *Phys. Rev.*, 119:507–509, 1960.

[107] S. Andersson and L. Dzhavadov. Thermal resistance due to point defects at high temperatures. *J. Phys. Condens. Matter*, 4:6209 – 6216, 1992.

[108] F. Agullo-Lopez, A. Mendez, G. Garcia, J. Olivares, and J. M. Cabrera. Synergy between thermal spike and exciton decay mechanisms for ion damage and amorphization by electronic excitation. *Phys. Rev. B*, 74:174109–174115, 2006.

[109] A. Rivera, A. Mendez, G. Garcia, J. Olivares, J.M. Cabrera, and F. Agullo-Lopez. Ion-beam damage and non-radiative exciton decay in $linbo_3$. *J. Lumin.*, 128:703–707, 2008.

[110] P. Kluth, C.S. Schnohr, O.H. Pakarinen, F. Djurabekova, D.J. Sprouster, R. Giulian, M.C. Ridgway, A.P. Byrne, C. Trautmann, and D.J. Cookson. Fine structure in swift heavy ion tracks in amorphous sio_2. *Phys. Rev. Lett.*, 101:175503–175507, 2008.

[111] M.V. Fischetti, D.J. DiMaria, S.D. Brorson, T.N. Theis, and J.K.Kirtley. Theory of high-field electron transport in silicon dioxide. *Phys. Rev. B*, 31:8124–8142, 1985.

[112] Z. Lin, L.V. Zhigilei, and V. Celli. Electron-phonon coupling and electron heat capacity of metals under conditions of strong electron-phonon nonequilibrium. *Phys. Rev. B*, 77:075133–075150, 2008.

[113] R.H.M. Groeneveld, R. Sprik, and A. Lagendijk. Femtosecond spectroscopy of electron-electron and electron-phonon energy relaxation in ag and au. *Phys. Rev. B*, 51:11433–11445, 1995.

[114] N. Medvedev and B. Rethfeld. Transient dynamics of the electronic subsystem of semiconductors irradiated with an ultrashort vacuum ultraviolet laser pulse. *New J. Phys.*, 12:073037–073043, 2010.

[115] J.M. Hernandez-Mangas, J. Arias, L. Bailon, M. Jaraiz, and J. Barbolla. Improved binary collision approximation ion implant simulators. *J. Appl. Phys.*, 91:658 – 668, 2002.

[116] A.J. Tuzzolino. Quantum efficiency of silicon in the vacuum ultraviolet. *Phys. Rev.*, 134:A205–A213, 1964.

[117] C. Delerue, G. Allan, and M. Lannoo. Theoretical aspects of the luminescence of porous silicon. *Phys. Rev. B*, 48:11024–11036, 1993.

[118] R.C. Alig, S. Bloom, and C.W. Struck. Scattering by ionization and phonon emission in semiconductors. *Phys. Rev. B*, 22:5565–5582, 1980.

[119] R.H. Bartram and A. Lempicki. Efficiency of electron-hole pair production in scintillators. *J. Lumin.*, 68:225–240, 1996.

[120] F. Scholze, H. Henneken, P. Kuschnerus, H. Rabus, M. Richter, and G. Ulm. Determination of the electron-hole pair creation energy for semiconductors from the spectral responsivity of photodiodes. *Nucl. Instr. and Meth. in Phys. Research A*, 439:208–215, 2000.

[121] R.C. Alig. Scattering by ionization and phonon emission in semiconductors. ii. monte carlo calculations. *Phys. Rev. B*, 27:968–977, 1983.

[122] G.W. Fraser, A.F. Abbey, A. Holland, K. McCarthy, A. Owens, and A. Wells. The x-ray energy response of silicon part a. theory. *Nucl. Instrum. Methods Phys. Research A*, 350:368–378, 1994.

[123] D.A. Papaconstantopolous. *Handbook of the Band Structure of Elemental Solids*. New York: Plenum, 1986.

[124] L.E. Ramos, L.K. Teles, L.M.R. Scolfaro, J.L.P. Castineira, A.L. Rosa, and J.R. Leite. Structural, electronic, and effective-mass properties of silicon and zinc-blende group-iii nitride semiconductor compounds. *Phys. Rev. B*, 63:165210–165220, 2001.

[125] Virginia Semiconductor Inc. *The compilation of experimental data done by Virginia Semiconductor Inc.* see www.virginiasemi.com and references therein., –.

[126] J.F. Seely and E.G. Harris. Heating of a plasma by multiphoton inverse bremsstrahlung. *Phys. Rev. A*, 7:1064–1067, 1973.

[127] W.S.M. Werner. Electron transport in solids for quantitative surface analysis. *Surf. Interface Anal.*, 31:141–176, 2001.

[128] E. O. Kane. Heating of a plasma by multiphoton inverse bremsstrahlung. *Phys. Rev.*, 159:624–631, 1967.

[129] M. Bonitz, Th. Bornath, D. Kremp, M. Schlanges, and W.D. Kraeft. Quantum kinetic theory for laser plasmas. dynamical screening in strong fields. *Contrib. Plasma Phys.*, 39:329–347, 1999.

[130] D. Kremp, Th. Bornath, M. Bonitz, and M. Schlanges. Quantum kinetic theory of plasmas in strong laser fields. *Phys. Rev. E*, 60:4725–4732, 1999.

[131] M. Brigida, C. Favuzzi, P. Fusco, F. Gargano, N. Giglietto, F. Giordano, F. Loparco, B. Marangelli, M.N. Mazziotta, N. Mirizzi, S. Rainò, and P. Spinelli. A new monte carlo code for full simulation of silicon strip detectors. *Nucl. Instr. and Meth. in Phys. Research A*, 533:322 – 343, 2004.

[132] N. Medvedev and B. Rethfeld. Dynamics of electronic excitation of solids with ultrashort laser pulse. *AIP Conf. Proc.*, 1278:250–261, 2010.

[133] F. Ladstädter, U. Hohenester, P. Puschnig, and C. Ambrosch-Draxl. First-principles calculation of hot-electron scattering in metals. *Phys. Rev. B*, 70:235125–235135, 2004.

[134] C. Kittel. *Introduction to Solid State Physics*. John Wiley & Sons, 8-th International Edition, 2004.

[135] C.-O. Almbladh, A. L. Morales, and G. Grossmann. Theory of auger core-valence-valence processes in simple metals. i. total yields and core-level lifetime widths. *Phys. Rev. B*, 39:3489–3502, 1989.

[136] S.M. Vinko *et al.* Electronic structure of an xuv photogenerated solid-density aluminum plasma. *Phys. Rev. Lett.*, 104:225001–225005, 2010.

[137] N. Medvedev, B. Rethfeld, D.O. Gerike, U. Zastrau, and E. Förster. Virtual snapshots of the fs xuv-excited conduction band of aluminum. *Phys. Rev. Lett.*, −:*to be submitted*, 2010.

[138] M. Beye, F. Hennies, M. Deppe, E. Suljoti, M. Nagasono, W. Wurth, and A. Föhlisch. Dynamics of electron-phonon scattering: Crystal- and angular-momentum transfer probed by resonant inelastic x-ray scattering. *Phys. Rev. Lett.*, 103:237401–237405, 2009.

[139] J.A.D. Matthew. Some quasi-atomic effects in the solid state. *Contemp. Phys.*, 34:89–98, 1993.

[140] N. Medvedev, U. Rosandi, H.M. Urbassek, and B. Rethfeld. Melting of a thin al film under uv and xuv irradiation. *Phys. Rev. B*, −:*to be submitted*, 2010.

[141] N. Medvedev and B. Rethfeld. Comprehensive model of ultrashort visible light irradiation of semiconductors. *J. Appl. Phys.*, 108:103112 − 103120, 2010.

[142] P.P. Pronko, P.A. VanRompay, C.Horvath, F. Loesel, T. Juhasz, X. Liu, and G. Mourou. Avalanche ionization and dielectric breakdown in silicon with ultrafast laser pulses. *Phys. Rev. B*, 58:2387–2390, 1998.

[143] J. Bonse, K.-W. Brzezinka, and A.J. Meixner. Modifying single-crystalline silicon by femtosecond laser pulses: an analysis by micro raman spectroscopy, scanning laser microscopy and atomic force microscopy. *Appl. Surf. Sci.*, 221:215–230, 2004.

[144] T. Y. Choi and C. P. Grigoropoulos. Plasma and ablation dynamics in ultrafast laser processing of crystalline silicon. *J. Appl. Phys.*, 92:4918–4926, 2002.

[145] T. Y. Choi, D. J. Hwang, and C. P. Grigoropoulos. Ultrafast laser-induced crystallization of amorphous silicon films. *Opt. Eng.*, 42:3383–3388, 2003.

[146] T. Sjodin, H. Petek, and H.-L. Dai. Ultrafast carrier dynamics in silicon: A two-color transient reflection grating study on a (111) surface. *Phys. Rev. Lett.*, 81:5664–5668, 1998.

[147] M. Hase, M. Kitajima, A.M. Constantinescu, and H. Petek. The birth of a quasiparticle in silicon observed in time-frequency space. *Nature*, 426:51–54, 2003.

[148] R.E. Russo, X. Mao, J.J. Gonzalez, and S.S. Mao. Femtosecond laser ablation icp-ms. *J. Anal. At. Spectrom.*, 17:1072–1075, 2002.

[149] L. Patrone, D. Nelson, V. I. Safarov, M. Sentis, W. Marine, and S. Giorgio. Photoluminescence of silicon nanoclusters with reduced size dispersion produced by laser ablation. *J. Appl. Phys.*, 87:3829–3838, 2000.

[150] E.S. Zijlstra, J. Walkenhorst, and M. E. Garcia. Anharmonic noninertial lattice dynamics during ultrafast nonthermal melting of insb. *Phys. Rev. Lett.*, 101:135701–135705, 2008.

[151] W. Marine, N.M. Bulgakova, L. Patrone, and I. Ozerov. Insight into electronic mechanisms of nanosecond-laser ablation of silicon. *J. Appl. Phys.*, 103:094902–094913, 2008.

[152] A. Vogel, N. Linz, S. Freidank, and G. Paltauf. Femtosecond-laser-induced nanocavitation in water: Implications for optical breakdown threshold and cell surgery. *Phys. Rev. Lett.*, 100:038102–038106, 2008.

[153] E. Higurashi, R. Sawada, and T. Ito. Optically induced angular alignment of trapped birefringent micro-objects by linearly polarized light. *Phys. Rev. E*, 59:3676–3681, 1999.

[154] G. Hüttmann, C. Yao, and E. Endl. New concepts in laser medicine: Towards a laser surgery with cellular precision. *Med. Laser Appl.*, 20:135–139, 2005.

[155] A. Rodriguez, M. Echeverria, M. Ellman, N. Perez, Y.K. Verevkin, C.S. Peng, T. Berthou, Z. Wang, I. Ayerdi, J. Savall, and S.M. Olaizola. High-power laser interference lithography process on photoresist: Effect of laser fluence and polarisation. *Microelectronic Engineering*, 86:937–941, 2009.

[156] D.H. Reitze, T.R. Zhang, W.M. Wood, and M.C. Downer. Two-photon spectroscopy of silicon using femtosecond pulses at above-gap frequencies. *J. Opt. Soc. Am. B*, 7:84–89, 1990.

[157] A. Cavalleri, K. Sokolowski-Tinten, J. Bialkowski, M. Schreiner, and D. von der Linde. Femtosecond melting and ablation of semiconductors studied with time of flight mass spectroscopy. *J. Appl. Phys.*, 85:3301–3305, 1999.

[158] D. von der Linde, K. Sokolowski-Tinten, and J. Bialkowski. Femtosecond melting and ablation of semiconductors studied with time of flight mass spectroscopy. *Appl. Surf. Sci.*, 109-110:1–10, 1997.

[159] P. Pronko, P.A. VanRompay, R. Singh, F. Qian, D. Du, and X. Liu. Laser induced avalanche ionization and electron-lattice heating of silicon with intense near ir femtosecond pulses. *Mat. Res. Soc. Symp. Proc.*, 397:45–51, 1996.

[160] J. Bonse, S. Baudach, J. Kruger, W. Kautek, and M. Lenzner. Femtosecond laser ablation of silicon-modification thresholds and morphology. *Appl. Phys. A*, 74:19–25, 2002.

[161] A. Borowiec, M. Mackenzie, G.C. Weatherly, and H.K. Haugen. Transmission and scanning electron microscopy studies of single femtosecond laser pulse ablation of silicon. *Appl. Phys. A*, 76:201–207, 2003.

[162] S.I. Kudryashov and V.I. Emel'yanov. Melting of silicon during femtosecond laser pulse. *JETP Lett.*, 73:228–231, 2001.

[163] M.I. Gallant and H.M. van Driel. Infrared reflectivity probing of thermal and spatial properties of laser-generated carriers in germanium. *Phys. Rev. B*, 26:2133–2146, 1982.

[164] G.E. Jellison Jr. and F.A. Modine. Optical functions of silicon between 1.7 and 4.7 ev at elevated temperatures. *Phys. Rev. B*, 27:7466–7472, 1983.

[165] H.M. van Driel. Kinetics of high-density plasmas generated in si by 1.06- and 0.53- μm picosecond laser pulses. *Phys. Rev. B*, 35:8166–8176, 1987.

[166] J.K. Chen, D.Y. Tzou, and J.E. Beraun. Numerical investigation of ultrashort laser damage in semiconductors. *Int. J. of Heat and Mass Transfer*, 48:501–509, 2005.

[167] D.P. Korfiatis, K.-A.Th. Thoma, and J.C. Vardaxoglou. Conditions for femtosecond laser melting of silicon. *J. Phys. D: Appl. Phys.*, 40:6803–6808, 2007.

[168] E. Antoncik. Impact ionization and quantum efficiency in semiconductors. *Czech. J. Phys. B*, 17:953–968, 1967.

[169] M.V. Fischetti and S.E. Laux. Monte carlo analysis of electron transport in small semiconductor devices including band-structure and space-charge effects. *Phys. Rev. B*, 38:9721–9745, 1988.

[170] M.V. Fischetti and S.E. Laux. Monte carlo study of electron transport in silicon inversion layers. *Phys. Rev. B*, 48:2244–2274, 1993.

[171] B.H. Christensen and P. Balling. Modeling ultrashort-pulse laser ablation of dielectric materials. *Phys. Rev. B*, 79:155424–155434, 2009.

[172] B. Rethfeld, H. Krutsch, and D.H.H. Hoffmann. Tracing laser-induced dielectric breakdown in solids. *Contr. to Plasma Physics*, 50:16–20, 2010.

[173] B. Rethfeld, O. Brenk, N. Medvedev, H. Krutsch, and D.H.H. Hoffmann. Interaction of dielectrics with femtosecond laser pulses: application of kinetic approach and multiple rate equation. *Appl. Phys. A*, 101:19–25, 2010.

[174] E. Yablonovitch and N. Bloembergen. Modeling ultrashort-pulse laser ablation of dielectric materials. *Phys. Rev. Lett.*, 31:877–879, 1972.

[175] E.D. Palik. *Handbook of Optical Constants of Solids*. Academic, Orlando, 1985.

[176] B.L. Henke, E.M. Gullikson, and J.C. Davis. X-ray interactions: photoabsorption, scattering, transmission, and reflection at e=50-30000 ev, z=1-92. *At. Data and Nucl. Data Tables*, 54:181–342, 1993.

[177] I. Plante and F.A. Cucinotta. Cross sections for the interactions of 1 ev - 100 mev electrons in liquid water and application to monte-carlo simulation of hze radiation tracks. *New J. Phys.*, 11:063047–063051, 2009.

[178] W. Lotz. Electron-impact ionization cross-sections and ionization rate coefficients for atoms and ions from hydrogen to calcium. *Z. Physik*, 220:446–472, 1969.

[179] W. Lotz. Electron-impact ionization cross-sections and ionization rate coefficients for atoms and ions from scandium to zinc. *Z. Physik*, 220:446–472, 1969.

[180] H.-K. Chung, M.H. Chen, W.L. Morgan, Y. Ralchenko, and R.W. Lee. Flychk: Generalized population kinetics and spectral model for rapid spectroscopic analysis for all elements. *High Energy Density Physics*, 1:3–12, 2005.

[181] M.D. Barriga-Carrasco. Proton stopping using a full conserving dielectric function in plasmas at any degeneracy. *Phys. Rev. E*, 82:046403–046408, 2010.

List of Publications

Publications in international journals

1. Nikita Medvedev and Alexander E. Volkov, *Monte-Carlo simulations of electronic excitations in swift heavy ion tracks in SiO_2*, AIP Conf. Proc. 999, 238 (2008).

2. Nikita Medvedev and Baerbel Rethfeld, *Dynamic of electronic subsystem of semiconductors excited with an ultrashort VUV laser pulse*, Proc. SPIE 7361, 73610E (2009).

3. Nikita Medvedev and Baerbel Rethfeld, *Effective energy gap of semiconductors under irradiation with an ultrashort VUV laser pulse*, Europhys. Lett. 88, 55001 (2009).

4. Orkhan Osmani, Nikita Medvedev, Marika Schleberger and Baerbel Rethfeld, *Excitation and relaxation of swift heavy ion irradiated dielectrics*, e-J. Surf. Sci. Nanotech. Vol. 8, p.278 (2010).

5. Nikita Medvedev, Alexander E. Volkov, Baerbel Rethfeld and Nikita S. Shcheblanov, *Effect of inter-atomic Auger processes on relaxation of electronic vacancies at deep levels of highly ionized atoms in swift heavy ion tracks*, Nucl. Instrum. And Meth. B 268, 2870 (2010).

6. Nikita Medvedev, Orkhan Osmani, Baerbel Rethfeld and Marika Schleberger, *Track creation after swift heavy ion irradiation of insulators*, Nucl. Instrum. And Meth. B 268, 3160 (2010).

7. Nikita Medvedev and Baerbel Rethfeld, *Transient dynamics of the electronic subsystem of semiconductors irradiated with an ultrashort VUV laser pulse*, New J. Phys. 12, 073037 (2010).

8. Baerbel Rethfeld, Oliver Brenk, Nikita Medvedev, Helena Krutsch and Dieter H.H. Hoffmann, *Interaction of dielectrics with femtosecond laser pulses: application of kinetic approach and multiple rate equation*, Appl. Phys. A 101, 19 (2010).

9. Nikita Medvedev, Alexander E. Volkov, Nikita Stcheblanov and Baerbel Rethfeld, *Early stage of the electron kinetics in swift heavy ion tracks in dielectrics*, Phys. Rev. B 82, 125425 (2010).

10. Nikita Medvedev and Baerbel Rethfeld, *Dynamics of Electronic Excitation of Solids with Ultrashort Laser Pulse*, AIP Conf. Proc. 1278, 250 (2010)

11. Nikita Medvedev and Baerbel Rethfeld, *Comprehensive model of ultra-short visible light irradiation of semiconductors*, J. Appl. Phys. 108, 103112 (2010).

Published reports

1. N. Medvedev, O. Osmani, M. Schleberger, and B. Rethfeld, *Combination of Monte-Carlo simulation and Two Temperature Model for Track creation in swift heavy ion irradiated dielectrics*, GSI Annual Report of the High Energy Density Physics 2009 p.TH-19 (2010)

2. O. Brenk, N. Medvedev, and B. Rethfeld, *Modelling laser-induced dielectric breakdown with the multiple rate equation*, GSI Annual Report of the High Energy Density Physics 2009 p.TH-07 (2010)

3. N. Medvedev and B. Rethfeld, *Electronic Dynamics of Semiconductors after Ultra-short VUV Free-Electron Laser Pulse Irradiation*, GSI Scientific Report 2008 p.TH-14 (2009)

4. N. Medvedev and B. Rethfeld, *Monte-Carlo study of electron dynamics in silicon during irradiation with ultrashort VUV laser pulses*, GSI, ILIAS Progress Report No. 3 (05/2008) p.59

5. N. A. Medvedev, A. E. Volkov, *Monte-Carlo simulation of electronic excitations in tracks of swift heavy ions in dielectrics*, GSI Scientific Report 2006 (2007) p.311.

6. M. Lang, W. Hasenkamp, N. Ishikawa, N. Medvedev, R. Neumann, R. Papaleo, C. Trautmann, K.-O. Voss, T. Yamaki, *Influence of ion-charge state on damage morphology of ion tracks in dark mica*, GSI Scientific Report 2006 (2007) p.312.

7. M. Lang, K.-O. Voss, R. Neumann, C. Trautmann, N. Medvedev, W. Hasenkamp, R. Papaleo, U. A. Glasmacher, G. A. Wagner, N. Ishikawa, T. Yamaki, *Influence of ion velocity on the track morphology in dark mica*, GSI Scientific Report 2005 (2006) p.343.

8. N. A. Medvedev, *Etch-pit morphology of tracks induced by ions in natural dark mica*, GSI Summer Student School 2005 Proceedings (16th International Students Program, Darmstadt, Germany, 8 August - 30 September 2005).

Presentations on Conferences/Invited Reports (presenter underlined)

1. <u>N. Medvedev</u> and B. Rethfeld, *Ultrafast electron kinetics in metals irradiated with femtosecond XUV laser pulses*, (Oral).
   DPG Spring Meeting, Surface Science Division, Dresden, Germany. 03/2011.

2. <u>N. Medvedev</u>, O. Osmani, M. Schleberger, B. Rethfeld, *Temporally resolved track creation in dielectrics after swift heavy ion irradiation. Part I: Monte-Carlo simulation*, (Oral).
   DPG Spring Meeting, Surface Science Division, Dresden, Germany. 03/2011.

3. <u>O. Osmani</u>, N. Medvedev, B. Rethfeld, M. Schleberger, *Temporally resolved track creation in dielectrics after swift heavy ion irradiation. Part II: Two Temperature Model*, (Oral).
   DPG Spring Meeting, Surface Science Division, Dresden, Germany. 03/2011.

4. <u>K. Huthmacher</u>, N. Medvedev, B. Rethfeld, *Dynamics of electrons in liquid water excited with ultrashort VUV laser pulse*, (Oral).
   DPG Spring Meeting, Surface Science Division, Dresden, Germany. 03/2011.

5. <u>N. Medvedev</u> and B. Rethfeld, *Electron kinetics in Aluminum irradiated with VUV femtosecond laser pulses*, (Oral).
   31th International Workshop on Physics of High Energy Density in Matter, Hirschegg, Austria. 01/2011.

6. <u>N. Medvedev</u>, *Combined Monte-Carlo – Two Temperature Model simulations of swift heavy ion track creation*, (Oral).
   Invited report at University of Helsinki, Finland. 11/2010.

7. <u>N. Medvedev</u>, *Ultrafast electron kinetics in semiconductors and metals irradiated with VUV-XUV femtosecond laser pulse*, (Oral).
   Invited report in XFEL-group, DESY, Hamburg, Germany. 10/2010.

8. <u>O. Osmani</u>, N. Medvedev, B. Rethfeld, and M. Schleberger, *Ultrafast excitation and relaxation processes in swift heavy ion irradiated insulators*, (Oral).
   IISC-18, 18th International Workshop on Inelastic Ion-Surface Collisions, Gatlinburg, Tennessee, USA. 10/2010.

9. K. Schwartz, N. Medvedev, <u>A. Volkov</u>, C. Trautmann, B. Rethfeld, and R. Neumann *Effect of diffusion of valence holes to defect distribution in swift heavy ion tracks in alkali-halides*, (Poster).
   IBMM-17, 17th International Conference on Ion Beam Modification of Materials, Montreal, Canada. 09/2010.

10. <u>O. Osmani</u>, N. Medvedev, B. Rethfeld, and M. Schleberger, *Ultrafast excitation and relaxation processes of swift heavy ion irradiated insulators*,

(Poster).
IBMM-17, 17th International Conference on Ion Beam Modification of Materials, Montreal, Canada. 09/2010.

11. N. Medvedev, O. Osmani, B. Rethfeld and M. Schleberger, *Three-zone model of track creation after swift heavy ion impact on insulators*, (Oral). ICACS 24, the 24th International Conference on Atomic Collisions in Solids, Krakow, Poland. 07/2010.

12. N.A. Medvedev, K. Schwartz, A.E. Volkov, B. Rethfeld, C. Trautmann *Effect of spatial redistribution of electronic excitations on formation of the defect halo of swift heavy ion tracks in alkali-halides*, (Oral). ICACS 24, the 24th International Conference on Atomic Collisions in Solids, Krakow, Poland. 07/2010.

13. B. Rethfeld, N. Medvedev, *Interaction of ultrashort VUV laser pulses with semiconductors*, (Oral) FLAMN-10, Fundamentals of Laser Assisted Micro- & Nanotechnologies, St. Petersburg, Russia. 07/2010.

14. N. Medvedev and B. Rethfeld, *Transient dynamics of electronic subsystem of aluminum target irradiated with an ultrashort XUV laser pulse*, (Poster, accepted for presentation). High Power Laser Ablation conference, Santa Fe, New Mexico, USA. 04/2010.

15. N. Medvedev and B. Rethfeld, *Electronic Kinetics of Semiconductors under an Ultrashort VUV Laser Pulse Irradiation*, (Poster, accepted for presentation). High Power Laser Ablation conference, Santa Fe, New Mexico, USA. 04/2010.

16. N. Medvedev and B. Rethfeld, *New self-consistent model of ultrashort laser irradiation of materials*, (Oral). DPG Spring Meeting, Surface Science Division, Regensburg, Germany. 03/2010.

17. N. Medvedev, O. Osmani, B. Rethfeld and M. Schleberger, *Spatial and temporal resolved microscopic processes in dielectrics irradiated with swift heavy ions*, (Oral). DPG Spring Meeting, Surface Science Division, Regensburg, Germany. 03/2010.

18. N. Medvedev and B. Rethfeld, *Kinetics of electronic subsystem of metallic target irradiated with an intense ultrashort XUV laser pulse*, (Poster). SNI-2010 "Synchrotron, Neutron and Ion Irradiation", Berlin, Germany. 02/2010.

19. <u>N. Medvedev</u> and B. Rethfeld, *Excitation of Metals with Ultrashort Laser Pulses*, (Poster).
   30th International Workshop on Physics of High Energy Density in Matter, Hirschegg, Austria. 02/2010.

20. N. Medvedev and <u>B. Rethfeld</u>, *Three zone model of track creation after swift heavy ions irradiation of insulators*, (Oral).
   30th International Workshop on Physics of High Energy Density in Matter, Hirschegg, Austria. 02/2010.

21. <u>N. Medvedev</u> and B. Rethfeld, *Transient Dynamic of Electrons in Metal irradiated with an Ultrashort Laser Pulse*, (Oral).
   BMBF FLASH-project meeting, Rostock, Germany. 10/2009.

22. <u>O. Osmani</u>, N. Medvedev, M. Schleberger and B. Rethfeld, *Electronic Properties Excitation and Relaxation of Swift Heavy Ion Irradiated Dielectrics* (Oral).
   ACSIN-10, 10th International Conference on Atomically Controlled Surfaces, Interfaces and Nanostructures, Granada, Spain. 09/2009.

23. <u>N. Medvedev</u>, A. E. Volkov, B. Rethfeld and N. S. Shcheblanov, *Effect of inter-atomic Auger processes on relaxation of electronic vacancies at deep levels of highly ionized atoms in swift heavy ion tracks*, (Poster).
   REI-15 "Radiation Effects in Insulators", Padova, Italy. 09/2009.

24. <u>N. Medvedev</u>, O. Osmani, B. Rethfeld and M. Schleberger, *Track Creation after Swift Heavy Ion Irradiation of Insulators*, (Poster).
   REI-15 "Radiation Effects in Insulators", Padova, Italy. 09/2009.

25. <u>N. Medvedev</u>, *Excitation and Relaxation of Electronic Subsystem at Femtosecond Timescales*, (Oral).
   Invited report at GSI Plasma Physics Department, Darmstadt, Germany. 05/2009.

26. <u>N. Medvedev</u> and B. Rethfeld, *Dynamic of Electronic Subsystem of Semiconductors irradiated with an Ultrashort VUV Laser Pulse*, (Oral).
   SPIE Europe's Optics and Optoelectronics Congress, Prague, Czech Republic. 04/2009.

27. <u>N. Medvedev</u> and B. Rethfeld, *Electronic Dynamics of Semiconductors after Femtosecond Laser Pulse Irradiation*, (Oral).
   BMBF FLASH-project meeting, Kassel, Germany. 04/2009.

28. <u>N. Medvedev</u> and B. Rethfeld, *Electronic dynamics of semiconductors irradiated with an ultrashort VUV laser pulse*, (Oral).
   DPG Spring Meeting of the Section Condensed Matter, Dresden, Germany. 03/2009.

29. <u>N. Medvedev</u> and B. Rethfeld, *Theoretical Study of Electronic Dynamics of Semiconductors after Irradiation with an Ultrashort VUV Laser Pulse*, (Poster).
   29th International Workshop on Physics of High Energy Density in Matter, Hirschegg, Austria. 02/2009.

30. <u>N. Medvedev</u>, *Excitation and Relaxation of Electronic Subsystem at Femtosecond Timescales*, (Oral).
   Invited report at Duisburg-Essen University, Physics Department, Duisburg-Essen, Germany. 10/2008.

31. <u>N. Medvedev</u> and B. Rethfeld, *Monte-Carlo Simulation of Electronic Dynamics in Silicon Irradiated with an Ultra-short VUV Free-Electron Laser Pulse*, (Poster).
   XXX-ECLIM, 30th European Conference on Laser Interaction with Matter, Darmstadt, Germany. 09/2008.

32. N. Medvedev and <u>A. E. Volkov</u>, *Monte-Carlo Simulations of Electronic Excitations and Relaxations in Swift Heavy Ions Tracks in Dielectrics*, (Poster).
   SHIM, Seventh International Symposium on Swift Heavy Ions in Matter, Caen, France. 06/2008.

33. <u>N. Medvedev</u>, *Monte Carlo Simulation of Electronic Excitation after Swift Heavy Ion Irradiation*, (Oral).
   Invited talk at Physics Department, Kaiserslautern, Germany. 05/2008.

34. <u>N. Medvedev</u> and B. Rethfeld, *Monte-Carlo study of electronic dynamics in semiconductors with an ultrashort XUV-laser pulse*, (Oral).
   Combined DPG Meeting of the Division AMOP, Darmstadt, Germany. 03/2008.

35. <u>N. Medvedev</u> and B. Rethfeld, *Excitation of electrons in Silicon with an ultrashort XUV free electron laser pulse: a Monte-Carlo study*, (Oral).
   DPG meeting: Chemical and Polymer Physics Division, Berlin, Germany. 02/2008.

36. <u>N. Medvedev</u> and B. Rethfeld, *Monte-Carlo study of electronic dynamics in Silicon with an ultrashort XUV free electron laser pulse*, (Poster).
   28th International Workshop on Physics of High Energy Density in Matter, Hirschegg, Austria. 01/2008.

37. <u>N. Medvedev</u>, *Material Excitation in Swift Heavy Ion Tracks*, (Oral).
   Invited report in Technical University of Kaiserslautern, Germany. 10/2007.

38. N. Medvedev and <u>A.E. Volkov</u>, *Monte-Carlo Simulation of Electronic Excitations and Relaxations in Swift Heavy Ion Tracks in Dielectric*, (Oral).

Electron microscopy and multiscale modelling EMMM-2007: An International Conference, Moscow, Russia. 09/2007.

39. <u>N. Medvedev</u>, *Monte Carlo simulations of electronic excitations in swift heavy ions tracks in dielectrics*, (Oral).
Invited report in GSI Material Research Department, Darmstadt, Germany. 12/2006.

40. M. Lang, K.-O. Voss, N. Medvedev, W. Hasenkamp, U.A. Glasmacher, N. Ishikawa, R. Neumann, R. Papaleo, <u>C. Trautmann</u>, G.A. Wagner, T. Yamaki, *Etch-pit morphology of tracks induced by heavy ions in natural mica*, (Poster).
IBMM-2006, 15th International Conference on Ion Beam Modification of Materials, Budapest, Hungary. 09/2006.

41. <u>N. Medvedev</u> and M. Lang, *Etch-pit morphology in dark mica (phlogopite); Raman spectroscopy analysis of Zirkon ($ZrSiO_4$)*, (Oral).
Invited report in GSI Material Research Department, Darmstadt, Germany. 09/2006.

42. <u>A.E. Volkov</u> and N.A. Medvedev, *Does ionization equilibrium exist in swift heavy ion tracks?*, (Poster)
ICACS 22, the 22th International Conference on Atomic Collisions in Solids, Berlin, Germany. 05/2006.

43. <u>N. Medvedev</u>, *Etch-pit morphology of tracks induced by ions in natural dark mica*, (Oral).
16th International Students Program (Summer Student School), Darmstadt, Germany. 09/2005.

Acknowledgments

Curriculum Vitae

Personal details:

Name	:	Nikita Andreevich Medvedev
Nationality	:	Russia
Date of birth	:	December 26, 1983
Place of birth	:	Aktyubinsk, USSR
Marital Status	:	Not married
Contacts	:	medvedev@physik.uni-kl.de

Education:

1990 − 2001	:	Secondary Comprehensive School No. 5, Kirzhach-city, Russia Graduated with distinction (silver medal)
1991 − 1998	:	Musical School No. 3, Kirzhach-city, Russia Speciality: Piano
2001 − 2005	:	Bachelor degree study Department of Theoretical and Nuclear Physics, Moscow Engineering Physics Institute (State University), Russia (Bachelor of Science) Speciality: Applied Mathematics and Physics. Thesis: "Analysis of ionization equilibrium conditions in tracks of swift heavy ions",
2005 − 2007	:	Master degree study Department of Theoretical and Nuclear Physics, Moscow Engineering Physics Institute (State University), Russia (Master of Science) Speciality: Applied Mathematics and Physics. Thesis: "Monte-Carlo modeling of excitation and relaxation of electronic subsystem of dielectric in tracks of swift heavy ions",

Scientific work experience:

08/2005 – 10/2005	:	Summer student program.
		Participation in experiments in the PROBRAL project.
		Material Research Department, GSI, Darmstadt, Germany.
06/2006 – 12/2006	:	Invited researcher (Mitarbeiter).
		Participation in experimental and theoretical investigations
		of general aspects of swift heavy ion tracks formation.
		Material Research Department, GSI, Darmstadt, Germany.
02/2004 – 09/2007	:	Student's scientific practice. Junior researcher.
		Institute of General and Nuclear Physics,
		Russian Research Centre 'Kurchatov Institute', Moscow, Russia.
09/2007 – present	:	Doctoral research
		Fachbereich Physik,
		Technische Universität Kaiserslautern, Germany